UNIVERSITY OF CALIFORNIA,
IRVINE

An Investigation of the Reuse of Powder Feedstock, Process Parameters, and General Operational Procedures for Laser Engineered Net Shaping Additive Manufacturing

THESIS

submitted in partial satisfaction of the requirements
for the degree of

MASTER OF SCIENCE

in Materials Science and Engineering

by

Katherine Lorinda Terrassa

Thesis Committee:
Professor Julie M. Schoenung, Chair
Provost and Executive Vice Chancellor Enrique J. Lavernia
Assistant Professor Timothy Rupert

2017

DEDICATION

To

my parents, husband, and family,

Thank you for your endless support and encouragement. Your belief in my success has made it so.

TABLE OF CONTENTS

LIST OF FIGURES

LIST OF TABLES

ACKNOWLEDGMENTS

I would like to express my gratitude to my committee chair, Professor Julie M. Schoenung, for providing an environment that allowed me to grow as a researcher and engineer. I am grateful for the personally challenging opportunities I have been given and her encouragement to tackle them.

I would like to thank my committee members, Provost Enrique Lavernia and Professor Timothy Rupert, whose work and appreciation for engineering research has been an inspiration throughout my graduate career.

In addition, a thank you to my lab family for sharing their priceless experimental knowledge and tips on how to be a graduate student, but mostly for their moral support throughout my trials and tribulations. It truly takes a village!

I would like to thank Sandia National Laboratories in Livermore, Ca. for the financial support provided by contract 1687547.

ABSTRACT OF THE THESIS

An Investigation of the Reuse of Powder Feedstock, Process Parameters, and General Operation Procedures for Laser Engineered Net Shaping Additive Manufacturing

By

Katherine Lorinda Terrassa

Master of Science in Materials Science and Engineering

University of California, Irvine, 2017

Professor Julie M. Schoenung, Chair

Laser Engineered Net Shaping, LENS®, is a multi-variable process of Additive Manufacturing that employs a high-power laser to deposit powder feedstock onto a substrate to build parts layer-by-layer. Advantages of this process are tailored microstructures with optimized structural properties for a variety of industry applications. The LENS® system parameters allow for variable user control but also introduce complexity into the process where every change in deposition procedure results in different effects on the build. To understand the connection between process parameters and build quality, each variable should be fully understood. The focus of this study was to isolate single variables and exhaustively analyze the effects on the deposition process. The first project investigates reusing powder feedstock for multiple cycles and the effects on powder properties and build quality. The second project examines the effect of varying the hatch rotation angle parameter by characterizing the resulting microstructural and mechanical properties. Microstructural and compositional characterization was done through several microscopy techniques to analyze the 316L SS powders, used throughout this thesis, and the manufactured parts. Bulk

material properties were analyzed with compression, microhardness, and density testing. It was found that reusing powder for ten cycles causes minimal changes to the powder properties. The properties of builds tested from select cycles were unchanged. Varying the hatch rotation angle between layers of a deposition did affect microstructural development which influenced mechanical properties. Finally, the complexity of the LENS® system was discovered through extensive operation, and the care required to manufacture consistent parts is exemplified.

INTRODUCTION

The field of metal based Additive Manufacturing (AM) has gained traction in recent years as new process developments have presented new application opportunities for the technology to expand beyond a prototyping tool. End-use products are now being fabricated in various alloy composition for applications in aerospace, automotive, medical, and military industries. Breaking from the traditional subtractive machining, AM offers the unique capability of controlling the microstructure of a material to design mechanical properties for a specific application while building a complex part layer-by-layer. This level of control allows for the repairing and refurbishing of damaged or defective components, and the creation of functionally graded materials for use where dissimilar properties are required at adjacent locations of a part. Traditionally these properties would not have been possible within one component or required multiple manufacturing steps. With AM, composite parts with homogeneous matrix materials are achievable and the post processing is minimal. This manufacturing advantage has been employed for aerospace and automotive applications requiring stiff, lightweight parts [1, 2, 3], custom biomedical implants [4, 5], and recently a composite prototype submersible hull was built by the U.S. Navy in an effort to push the AM application envelope [6]. With new opportunities comes new research questions. AM is a very dynamic process that requires knowledge of all aspects of the material used and the specific process for the given application. Directed energy deposition (DED) is a class of AM processes that builds up a part by utilizing a focused energy source to simultaneously heat and melt a substrate while material is being injected into the melt pool.

The Laser Engineered Net Shaping (LENS®) system, shown in Figure1 (a), is a DED device that was developed by Sandia National Laboratories and commercialized by Optomec, USA

in 1997 [1], [7]. The system consists of a high-power laser that creates a melt pool on a substrate secured to a moving stage while under an inert gas environment, typically argon, within a glovebox with the oxygen content maintained around or below 10 ppm. The stage rasters in the X and Y directions per a CAD drawing while the laser height is incremented in the positive Z direction to build the part up layer-by-layer. Powder feedstock is loaded into an external gas-pressurized hopper, fed into the LENS® chamber by argon carrier gas, and ejected from four nozzles into the laser melt pool [7]. A schematic of this setup is shown in Figure1 (b) [8]. Each pass of the laser deposits a rapidly solidified track, creating parts that attain high density comparable to traditionally cast materials. The four-nozzle system and clean environment make the LENS® one of the most flexible DED platforms [1].

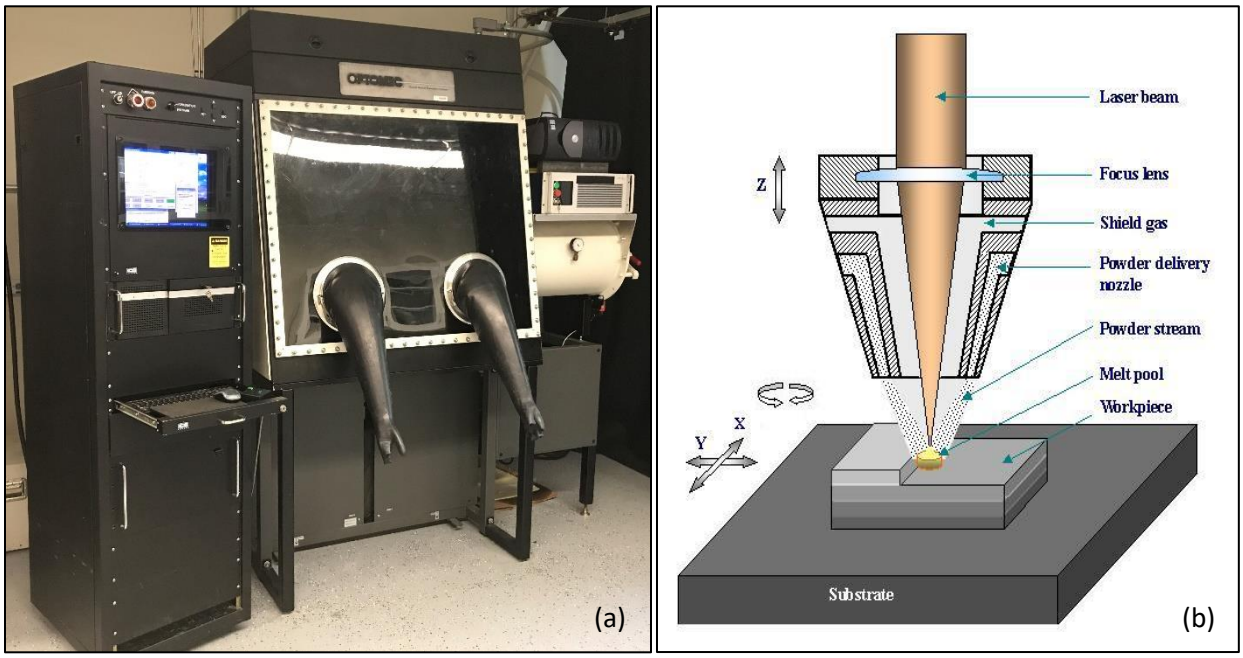

Figure1. LENS® 750 Workstation (a) and schematic of laser and powder delivery setup in relation to moveable stage inside the glovebox (b) [8].

There is a critical region of the laser beam above and below the focal plane of the laser spot size where the energy density is high enough to create a melt pool on the substrate. If the substrate or current layer is not within this region, no deposition will occur. Likewise,

during a deposition the melt pool will not grow to a height that moves the build surface out of this region. This region is shown in Figure 2 highlighted in green surrounding the laser spot size [1].

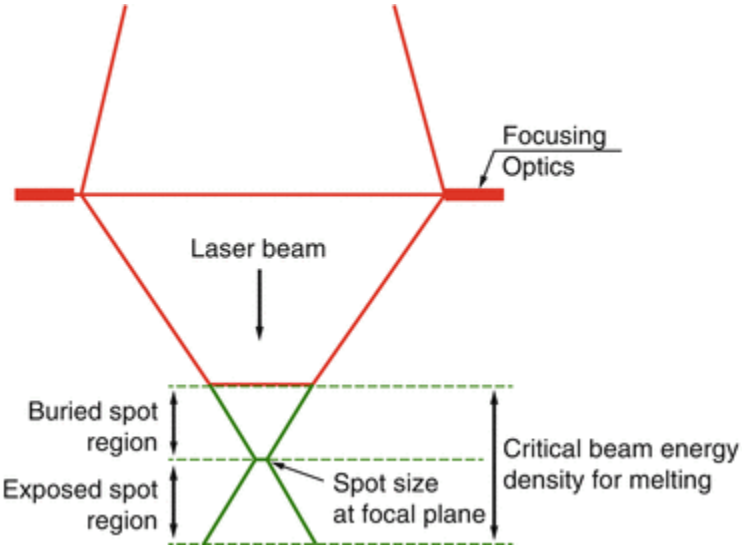

Figure 2. Laser optics schematic of critical deposition region for DED [1].

The process parameters used, including the chosen material, for a LENS® deposition dictate the outcome of the manufactured part and should be optimized accordingly. In addition to correctly identifying the laser focal plane, the laser power, laser scan rate, powder feed rate, layer height, hatch pattern, hatch spacing, and hatch rotation angle are important process parameters that can be varied in the workstation. A major advantage of the DED process is the superior mechanical properties that can be developed due to the ability to control microstructures with these input parameters. The small melt pool size, ~0.5 mm [9], [10], [11] and rapid scanning speed of the laser produce high cooling rates of $10^3 - 10^4$ K/s [10], [11] and large thermal gradients within the material. Below the melt pool is a heat affected zone (HAZ) with varying penetration depth that consists of the region between the solid/liquid interface [11]. The size of the HAZ depends on the thermal transfer and solidification rates between the melt pool and substrate or previously deposited layers.

These conditions lead to a unique cellular solidification structure with nonequilibrium grains that are not found in cast materials [1], [11]. The process conditions that produce these desirable microstructures are unique to material, geometry, and size of the deposition.

Optimizing properties of powder feedstock are equally as important as the conditions set for the melt pool focal plane and laser optics. Properties of size, morphology, and chemistry can influence the interaction between the powder particles and the melt pool or laser and ultimately the build quality. Ideally most of the powder ejected from the nozzles would be collected in the melt pool and contribute to the build, however the efficiency of powder delivery for the LENS® system is often less than 10% and excess powder is either distributed within the chamber from the turbulence of the argon gas or left over on the stage surrounding the build. The left-over powder is typically either discarded or reused with an arbitrary amount of virgin powder for a number of cycles that is generally determined from the operator's experience. There is little knowledge of the condition of left over powder and therefore the effects on build quality are equally unknown. A motivation of this study was to collect the powder from the stage and determine the effect of repeated reuse on properties of the powder and the parts built from multiple reuse cycles. The collectable powder can change in size and shape due to interactions with other particles during the delivery process, interactions with the laser or melt pool, as well as the violent shaking that occurs during required sieving between subsequent cycles to remove agglomerates. Understanding the extent of these changes and the direct effect on the builds is the first project of this study and the focus of Chapter 1.

Varying any parameters will affect the deposition quality. To understand the primary influence of a parameter it is important to keep all other parameters constant. In addition to

investigating the effect of changing powder conditions, the next project in this study focuses on the effect of changing the scanning direction of subsequent layers, i.e. the hatch rotation angle which is typically set to 90°. DED parts from powder feedstock typically exhibit a corrugated surface topology due to the deposition of parallel tracks within a single layer [1]. This topology can create gaps between layers and is compensated for by rotating the scanning direction of the next layer with respect to the previous. The change in layer orientation also eliminates preferential grain growth and helps to minimize residual stress by eliminating anisotropy and gaps without drastically changing the layer height [1, 9, 10]. The common 90° rotation angle is rarely modified; however research has shown that enhanced mechanical properties can be achieved with hatch rotation angles of 105° [12]. The subject of Chapter 2 of this study is to corroborate the superior mechanical properties of the 105° hatch rotation as well as investigate the effect on microstructure and grain growth specifically.

Finally, this study concludes with a closer look at the general operation, maintenance, and intricacies of process control of the LENS® 750 Workstation used throughout this project, shown in Figure1 (a). Standard operating procedures created for LENS® and relevant characterization processes are also presented.

The material used throughout this study was gas atomized 316L Stainless Steel powder, (lot no. 45981, sized 45-106 μm, Carpenter Technology Corporation, Philadelphia, PA). This LENS® system contains a 1 kW fiber laser and was used in the same configuration for each project with the beam energy focused such that depositions occurred within the buried spot region according to Figure 2. The working distance (WD) for the powder feed nozzles was set so the convergence of powder from all four nozzles was just below the current layer, in

the middle of the melt pool. The relation of the laser focal plane with the nozzle WD is illustrated in Figure 3, showing the relative focal length of the laser, set to 0.43 in, and the nozzle WD, set to 0.28 in, both in the buried region. To begin each deposition, the powder flow was first turned on to establish a consistent flow before introducing the laser and starting the build. All parts were designed to deposit a contour outline of the part prior to filling in the rest of the layer per the set hatch spacing and pattern. After the first layer is completed, the laser increments by the set layer height and the contour deposits again as the start of the next layer. The powder feed rate (PFR) is determined by the rotations per minute (RPM) input parameter, controlling the internal mechanism of the hopper. The starting working distance is set manually by lowering the laser head so that the nozzles are the desired height from the substrate. Adjustments to these parameters dictate the dimensions of the melt pool and the capture efficiency of the powder feedstock.

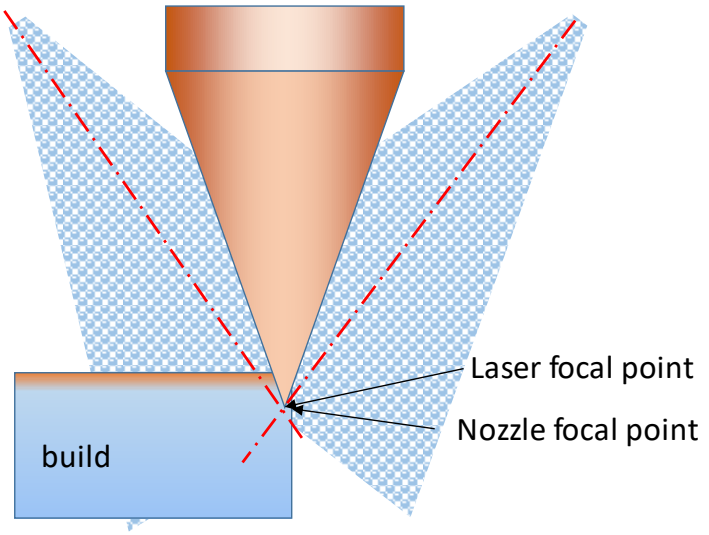

Figure 3. Schematic of nozzle convergence alignment with substrate or top layer surface.

The main deposition parameters for the test builds from both projects were determined through a parametric study of varying power and powder feed rate settings starting with process parameters known to deposit fully dense parts of similar composition. Coupon

depositions of each power and rate combination were evaluated by cutting each down the middle along the build axis using a band-saw and polishing to 1200 grit SiC grinding paper to examine internal porosity. The parameters determined to produce fully dense 316L SS parts for the current LENS® configuration are shown in Table 1.

Table 1. Primary deposition parameters for repeated test builds in Chapter 1 and 2.

Power (W)	Laser Speed (in/min)	Powder Feed Rate (g/min)	Layer Thickness (in)	Hatch Spacing (in)	Hatch Pattern	Hatch Rotation (°)	Working Distance (in)
295	40	26.7	0.01	0.016	Serpentine	90	0.28

CHAPTER ONE

1. Powder Reuse in Laser Directed Energy Deposition:

1.1. Background:

The potential to successfully reuse powder in DED machines has been a popular question in the last few years. Given the large percentage of powder that is left over after a deposition, powder reuse is attractive from an economics perspective but also pushes the need to understand the direct relationship between powder quality and build quality. Studies have been done on electron-beam machining (EBM) and selective laser melting (SLM) systems to investigate how the reuse of powder would affect the deposition process. The properties of interest are particle size distribution (PSD), particle morphology, tap density, flowability, and powder chemistry. Ardila et al. [14] studied the reuse of IN718 for 14 iterations in the SLM process and found only small variations in the PSD after 7 reuses. It was also noted that small changes in composition occurred with the decrease of Ni content yet this was attributed to a slight increase in oxidation and was within allowable tolerances for the alloy. Ardila tested deposited parts for porosity and impact toughness but found no discernable patterns through reuse iterations. Tang et al. [15] also utilized the SLM process but reused Ti-6Al-4V powder for 21 cycles and found that flowability improved with increased reuse and narrower PSD despite increased irregularity of particle morphology. Tang also noted an increase in oxygen content but attributed this to typical oxidation of the alloy over time and saw no undesirable influence on the mechanical properties of the parts or the deposition process itself. Carroll et al. [16] studied Waspaloy powder with direct metal laser deposition (DMLD) process over 11 cycles. Like Ardila and Tang, the mean particle size of Carroll's study decreased marginally but there was no noticeable change in powder surface finish or

morphology. There was also no noticeable change in chemistry of the particles or the builds after only a slight decrease in hardness after the first iteration. Carroll attributed the lack of deviation of powder properties through reuse to the low powder usage efficiency of 5% and predicted that with parameters optimized for capture efficiency the powder would have more interaction with the laser and substrate and the changes in powder properties would be more apparent.

These studies served as a baseline for this investigation into the reuse of 316L stainless steel (316L SS) powder with LENS® deposition. Similar properties of the feedstock powders were tracked through deposition iterations in addition to LENS® specific parameters. The test builds from each cycle were designed to be small enough to require a manageable amount of powder through the entire study but also provide proper specimens for compression yield strength, microhardness, and microstructure evaluation. The details of this project's procedure, methods, results and discussion are presented in the following sections.

1.2. Approach:

The scope of this powder reuse project spanned nine cycles of reuse, thus a total of ten cycles. The as-received (AR) powder was used in Cycle 0 (C0) and the parts made in C0 were C0 parts. The powder collected from the stage after the C0 cycle was then once-used powder, or Cycle 1 (C1) powder, to be deposited and build C1 parts. Depositions with C1 powder make C2 powder and parts, and so on to C9. Powders and parts from each cycle were characterized per the techniques described in the following method sections.

To properly reuse the powder after each deposition cycle within the LENS®, the powder was processed according to the procedure presented in the flow chart of Figure 1.1. The

depositions for C0 were made with unused, unprocessed AR powder. An unused bottle of AR powder was sieved and sampled to characterize the AR properties. Used powder was collected from the stage after the depositions and sieved to remove agglomerates larger than 150 μm, the maximum recommended particle size for the LENS®. The minimum recommended particle size is 38 μm however the decision was made to not remove the smaller particles in order to limit the total amount of powder required to achieve the desired number of deposition cycles. One bottle of each cycle was used for full PSD sieving analysis before being properly homogenized in a V-blender. One sample of 500 g was taken from each cycle after V-blending for analysis. Once the powder was rebottled after V-blending it was returned to the hopper for deposition in the next cycle. Further details on each process shown in Figure 1.1 are presented in the methods section.

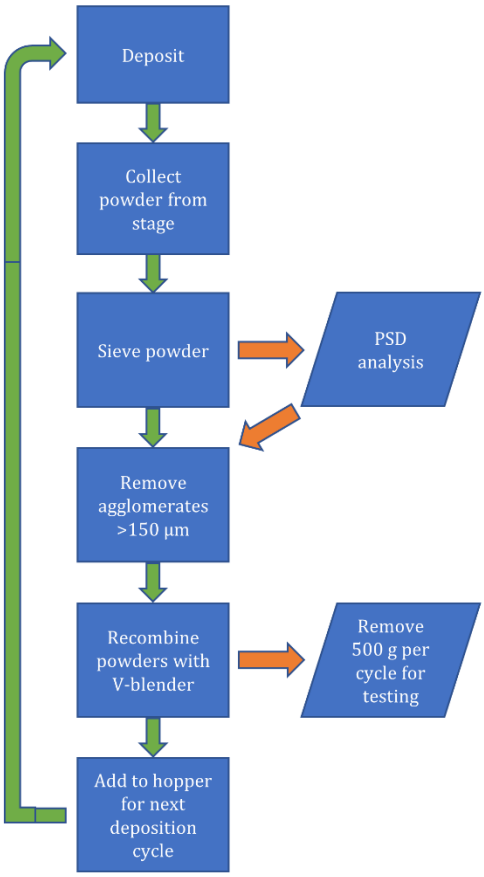

Figure 1.1. Flow chart of powder processing procedure, where PSD is particle size distribution. Green arrows indicate the procedure followed for every deposition and round of sieving. Orange arrows indicate the characterizing and sampling procedure followed once per cycle.

Test builds were deposited with consistent parameters from each cycle to properly characterize the effect of the reused powder. Additional parts of varying geometry and size were built from each cycle to provide enough reused powder to complete the ten cycles. The deposition parameters for the additional parts were consistent with those of the test builds except for laser power and powder feed rate which both varied slightly from build to build. It was determined through experience that the size and shape of builds greatly affected the melt pool characteristics. Due to the amount of powder used and production time, small modifications to deposition parameters were necessary to minimize the occurrence of a

plume from the melt pool. It was determined that this plume produced nanoscale stainless steel powders within the glovebox which could be hazardous once exposed to atmosphere during the maintenance process of the LENS® machine. The details of some of these additional parts are discussed in later chapters. The nanoscale powders, referred to here as black powder for their appearance, are discussed in later sections within this chapter.

1.3. Methods:

1.3.1. Powder Characterization:

1.3.1.1. Powder Sampling:

After sieving to remove agglomerates or perform PSD analysis, a V-blender was used to re-homogenize the particles. This process repeatedly separates and combines the powder particles during 100 full rotations. This technique was adapted from ASTM B215-15 [17]. Once the rotations were complete, a 500 g analysis sample was taken from each cycle one time. The rest of the powder was rebottled for use in the next cycle of depositions. Powder from the sampling was then used for all testing described in the subsequent sections.

1.3.1.2. Phase Identification:

X-ray diffraction (XRD) was performed in a Rigaku SmartLab X-ray Diffractometer (Rigaku Analytical Devices, Wilmington, Massachusetts) utilizing Cu Kα radiation and a scan speed of 2.0 degree/min for the 2θ range from 40°-100°. Powder samples from C0, C1, C5, and C9 were scanned to confirm phase consistency throughout the deposition cycles with reference DB card number 033-0397 for austenitic stainless steel. Black powder was also characterized with XRD at the same settings to understand any phase changes that occur due to the change in melt pool energy where this powder was produced.

1.3.1.3. Chemical Analysis:

Chemical analysis was conducted with energy dispersive spectroscopy (EDS) in a FEI Quanta 3D FEG dual beam scanning electron microscope (SEM) (FEI, Hillsboro, Oregon) on morphological and cross-section samples to identify particulates and impurities on the surface of and inside the particles as well as obtain bulk elemental analysis of the test builds. X-ray photoelectron spectroscopy (XPS) was performed with a KRATOS Axis SUPRA (Kratos Analytical, Manchester, United Kingdom) using a resolution of 200 μm to measure the elemental composition of the particles for a surface depth of ~10 nm from selected cycles. Data analysis was done with CasaXPS software to calibrate the adventitious carbon peak due to the use of a charge neutralizer while scanning. The particle samples were not treated with any solvents prior to scanning in order to preserve the surface chemistry.

A nearly complete bulk elemental composition analysis of the powders was obtained by EAG Laboratories (Liverpool, NY) through three techniques; Instrumental Gas Analysis, Inductively Coupled Plasma Optical Emission Spectroscopy, and Glow Discharge Mass Spectroscopy. Samples from all ten cycles were tested simultaneously to ensure process consistency. This analysis, along with EDS, was used to determine the Cr/Ni ratios and ferrite number (FN) of the powders to understand any austenite-ferrite structure changes through each reuse cycle. The Cr/Ni ratio was determined by calculating the chromium equivalent (Cr_{eq}) and nickel equivalent (Ni_{eq}) of a material, Equation 1.1 and 1.2 respectively [18].

$$Cr_{eq} = Cr + Mo + 0.7Nb \quad (1.1)$$

$$Ni_{eq} = Ni + 35C + 20N + 0.25Cu \quad (1.2)$$

Equation 1.1 uses the weight % of chromium (Cr), molybdenum (Mo), and niobium (Nb) to calculate the chromium equivalent or ferrite forming elements. Equation 1.2 calculates the austenite forming elements as the Ni_{eq} with weight % of nickel (Ni), carbon (C), nitrogen (N), and copper (Cu) [9] [19]. These values were then used to extrapolate the FN from the Cr_{eq} and Ni_{eq} WRC-1992 diagram [18] which is the amount of ferrite present in the alloy based on the composition. Some ferrite is needed to resist solidification cracking. This diagram estimates the expected ferrite content from the proportioned dilution ratios of a Fe-Cr-Ni alloy to obtain corrosion resistant austenitic stainless steels with low cracking susceptibility [9],[18], [19].

1.3.1.4. Particle Size Distribution:

The particle size distribution (PSD) of the particles from all cycles was determined through sieve analysis per ASTM B214-16 [20]. This standard also provides guidelines for determining the set amount of powder and sieving time required for specific materials. These guidelines were used to develop an SOP for 316L SS, Appendix I, resulting in 15 minute shake time for 700 – 1000 g of powder. After collecting the unused powder from the LENS® chamber stage, particles were separated by particle diameter of 38, 45, 106, and 150 μm in the shaker using sieves of mesh No. 400, 325, 140, and 100, respectively. A sample size of approximately 5.25 kg was used from each cycle for consistent comparison. After separating by mesh size, the powder was measured to determine weight distribution. All agglomerates greater than 150 μm were removed from the powders prior to use in the next cycle, thus the removed were created during the previous cycle of depositions. The particles in all sieves smaller than 150 μm were recombined using the V-blender method discussed previously.

A more detailed distribution of particle size was obtained from SEM micrographs of morphology samples at low magnification from cycles C0, C1, C5, and C9 analyzed in the Olympus BX53M Optical Microscope (OM) (Olympus, Center Valley, PA) by using a particle count and measure tool from Olympus Stream Basic analysis software. Micrographs were segmented to highlight particles and manually edited to ensure that only full particles were represented. The resulting PSD was determined from the average data collected of minimum particle diameter such that the number of particles sampled was equal for all cycles tested.

1.3.1.5. Morphology:

Powder morphology was evaluated using secondary electron mode of the SEM to image powders mounted to microscopy stubs with conductive carbon tape. The particles were mounted so as not to compromise their integrity by avoiding smashing or packing of the powder. SEM micrographs of low and high magnification were analyzed for qualitative representations of particle shape and size. Morphology was also characterized quantitatively using the OM Olympus Stream Basic analysis software count and measure tool to measure the sphericity of an equal number of particles from C0, C1, C5, and C9.

1.3.1.6. Cross-sectional Analysis:

The internal porosity of powder particles was evaluated by mounting particles in KonductoMet conductive filled phenolic mounting compound using a Buehler SimpliMet 1000 Automatic Mounting Press (Buehler, Lake Bluff, Ill.). The samples were polished metallographically to 0.04 μm colloidal silica suspension using Buehler EcoMet 250 grinder-polisher and examined in the SEM to observe the cross-section of the particles.

1.3.1.7. Tap Density and Flowability Measurements:

The powders from each cycle were tested using a method following ASTM B527-15 to determined their tap density [21]. This test evaluates a powder's packing density within a specified container. For these 316L SS powders, 100 ± 0.5 g of powder was measured to the nearest 0.01 g and poured into a 25 mL graduated cylinder with $\pm$ 0.2 mL precision. The volume of powder was recorded and the cylinder was then tapped for five minutes at 100 to 300 taps per minute, with a stroke height of approximately 3 mm. The tapped results can then be related to the physical property of flowability through the Hausner ratio. The tapped volume was recorded and the Hausner ratio, H, of tapped density to bulk (loose) density was calculated per Equation 1.3,

$$H = \frac{\rho_T}{\rho_B} \tag{1.3}$$

where ρ_T is the tapped density and ρ_B is the loose density. Powders with Hausner ratios greater than 1.25 are designated as having poor flowability.

The Carr index, an indication of powder compressibility, can also be extrapolated from the tap densities as it is dependent on the bulk and tapped volumes of powders as well. The relation to Hausner ratio is shown in Equation 1.4. A Carr index below 15 indicates a powder of good flowability and above 25 indicates poor flowability.

$$C = 100\left(1 - \frac{1}{H}\right) \tag{1.4}$$

The flowability of each powder cycle was measured through two other dynamic techniques. First, changes in the powder feed rate (PFR) within the LENS® machine were tracked during depositions of similar parts in each cycle. The Hall Flow meter method was then used to test powder flow of the sampled powders from each cycle.

PFR through the LENS® machine was calculated by measuring the amount of powder starting in the hopper before and after a deposition. The difference was then divided by the total powder flow time for the deposition, resulting in units of g/min.

The Hall Flow meter method was performed on 50 g samples from each cycle per ASTM B213-17 [22]. The powder was placed in a funnel apparatus resembling that shown in Figure 1.2. A stop watch was used to record the time duration for all powder to exit the funnel opening. The test was repeated four times for each cycle using different 50 g samples and the recorded data are presented as an average flow rate with units of 50 g/sec.

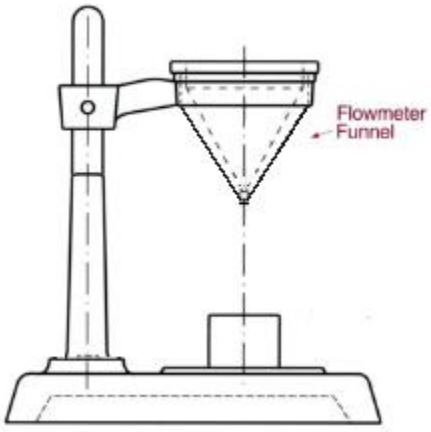

Figure 1.2. Hall Flow meter apparatus.

In addition, alternative analysis for flowability was done on powder samples from C0, C2, and C5 with a Revolution particle analyzer (Mercury Scientific Inc, Newton, CT). This device uses a rotating drum to measure flowability potential by analyzing avalanche energy from digital images of the powder behavior as the drum is rotated. The avalanche energy is measured as the change in potential energy of the powder before and after the fall of powder within the drum. For a powder that is free flowing, the avalanche energy is low [23].

1.3.2. Process and Parts Characterization:

1.3.2.1. Deposition Consistency:

To maintain deposition consistency, there were several steps taken prior to running the build program. First, the power output of the laser as seen by the substrate or current layer was measured using a power puck laser sensor that measures power in watts by sampling a 20 sec exposure of laser power. Extensive depositions can cause the lens cover, located in the deposition head below the focal lens, to become dirty or damaged and required to be cleaned or replaced. Both actions could alter the amount of laser power attenuation. Calibrating the power settings insures the expected amount of energy is delivered to the melt pool by the laser.

The powder feed nozzles were carefully cleared of any powder build up using a push pin inserted into each nozzle before every deposition. Powder alignment with the laser was also confirmed such that the four nozzles produce equal powder dispersion patterns with the laser output directly in the middle. The PFR associated with the amount of input powder in the hopper and the current RPM setting was also tracked for each test build. Details on this process and other LENS® consistency procedures are described in Chapter 3 of this thesis.

From each cycle of powder, a series of test builds with dimensions of 0.62 in x 0.62 in x 0.5 in, width x depth x height, were made with consistent deposition parameters to evaluate the effect of reused powder on build properties. Three of these builds were deposited in each cycle with 2.8, 2.9, and 3.0 RPM to ensure the test builds evaluated for mechanical properties were of consistent PFR through all cycles. Additional parts were deposited from each cycle to use powder and explore the consistency of the LENS® process. These parts are discussed in Chapter 3.

1.3.2.2. Process Efficiency:

The efficiency of powder usage was tracked to determine the potential impact of reusing powder continuously. The mass amount of powder used to deposit similar parts for each cycle was measured and compared to the amount of powder collected from the stage to be reused, thus the metric is powder reuse efficiency. In addition, this method provides insight about how the powder usage changes with geometry of builds within the same cycle.

1.3.2.3. Build Finish:

Parts from each build cycle were examined for geometrical accuracy as compared to the CAD drawing using calipers. The surface finish and coloring of parts were also compared throughout the cycles.

1.3.2.4. Cutting:

The test builds from cycles C0, C1, C5, and C9 were cut into smaller cuboids for subsequent characterization with a wire electric discharge machining (EDM) process. Each test build was cut into four cuboids from the center of the builds with aspect ratios of 1.5, the longer side of the cubes being parallel to the build direction as shown in Figure 1.3. A 2.5 mm thick cross-section sample including the substrate to the top layer was also cut from each build. The cuboids were used for density and compression testing. The cross-section sample was used for internal defect analysis, microhardness testing, and evaluation of weld pool and layer characteristics.

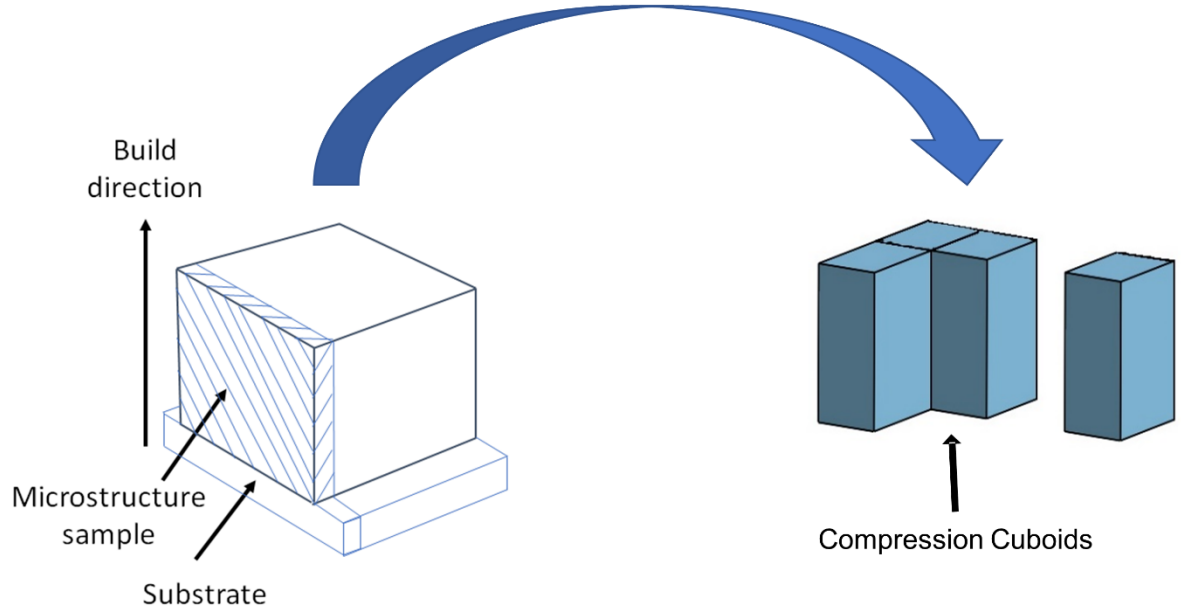

Figure 1.3. Schematic of test builds cut with EDM for microstructure analysis sample and density/compression analysis cuboids.

1.3.2.5. Internal Defects:

The internal porosity and microstructure of the builds was evaluated by mounting the cross-section samples cut from the test builds in KonductoMet conductive filled phenolic mounting compound using a Buehler SimpliMet 1000 Automatic Mounting Press. The samples were polished to 0.04 µm finish with colloidal silica suspension on the Buehler EcoMet 250 grinder-polisher. Internal porosity and build defects were examined and compared for C0, C1, C5, and C9 builds.

1.3.2.6. Chemical Analysis:

Chemical analysis was conducted with the EDS detector in the SEM on cross-section samples to identify bulk composition of each build as well as any internal particulates and impurities. This was used as a comparative analysis between the builds and to estimate their Cr_{eq}/Ni_{eq} ratio and FN.

1.3.2.7. Density:

Archimedes' principle was applied to test the density for each build from C0, C1, C5, and C9. The cuboids were polished to 1200 grit SiC grinding paper on all faces to remove surface roughness. A Mettler Toledo AG204 balance was used to perform the test with ethanol as the liquid medium to submerge the cuboids and measure their buoyancy. The weight of each specimen was measured in air and in the liquid. The density was calculated according to Equation 1.5,

$$\rho = \frac{W(a)*\rho(l)}{W(a)-W(l)} \quad (1.5)$$

where ρ(l) is the density of the liquid, W(l) is the weight of the solid in liquid, W(a) is the weight of the solid in air, and ρ is the density of the solid in g/cm^3. The four cuboids from each build were tested three times and the average was taken of all twelve test results to be the final density of the test build.

1.3.2.8. Compression:

The cuboids used for density testing were subjected to compression tests with the Instron 8801 universal testing machine (Instron Inc,. Norwood, MA). Strain was measured using a laser interferometer. The cuboids were prepared by grinding all faces to a 1200 grit surface finish to achieve and maintain the appropriate aspect ratio of 1.5 for compression testing per ASTM E9-09 [24]. The cubes were mounted between the anvils with WC platens, as shown in Figure 1.4, and moly-petrolatum lubricant. Each test was performed at a strain rate of 10^{-3} s^{-1} and stopped at 15% strain to avoid excessive strain and maintain equivalent test procedure for all cuboids. The test data provided by Bluehill software was postprocessed to account for the initial gauge length difference between the offset of the WC spacers and the actual height of each specimen. The corrected engineering strain was calculated by

multiplying the recorded axial strain by the ratio of measured strain to sample height. The engineering stress was corrected by multiplying the recorded stress by one minus the corrected engineering strain. The resulting engineering stress strain curve was used to plot the 0.2% offset from the elastic deformation response to determine the corrected compressive yield strength. Three specimens from each test build were tested and the average yield strength is presented.

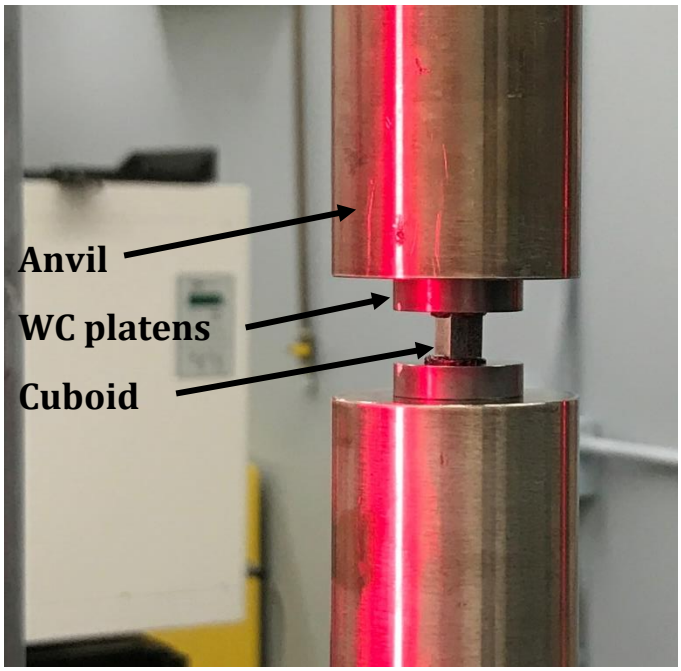

Figure 1.4. Compression test setup showing Instron anvils, platens, and test sample alignment.

1.3.2.9. Microhardness:

The microhardness of each test build from C0, C1, C5, C9 was tested with a Struers Duramin Microindenter (Struers, Copenhagen, Denmark) utilizing Vickers hardness scale with indents of 0.5 kgf for 10 s. Indents were made in a series of arrays, vertical from the substrate to the top layer and horizontal across the build. The Duramin 5 microindenter software measured the dimensions of the indent diagonals in microns and calculated the hardness according to Equation 1.6,

$$HV = 1.854 \frac{F}{d^2} \quad (1.6)$$

where F is the load in kgf, d is the arithmetic mean of the two diagonals of the indent in mm, and HV is the Vickers hardness. Average hardness from horizontal measurements on test builds from each cycle were compared as the change in hardness with increasing build height.

1.3.2.10. Weld Pool and Layer Characteristics:

Microstructure samples were etched using a 3:1 hydrochloric and nitric acid etchant for 30 seconds. This etchant highlights the dendritic and cellular structures that define the weld pool and layer geometry, as well as any defects formed during the build process. These were examined using the OM and Olympus Stream Basic software.

1.4. Results and Discussion:

1.4.1. Powder Characterization:

1.4.1.1. Phase Identification:

XRD scans for powder samples from C0, C1, C5, C9 are plotted in Figure 1.5. All scans show the same peaks of austenitic stainless steel, gamma-Fe FCC structure. No extraneous peaks were found in any samples, indicating that there was no effect on phase and no contamination from increased reuse cycles.

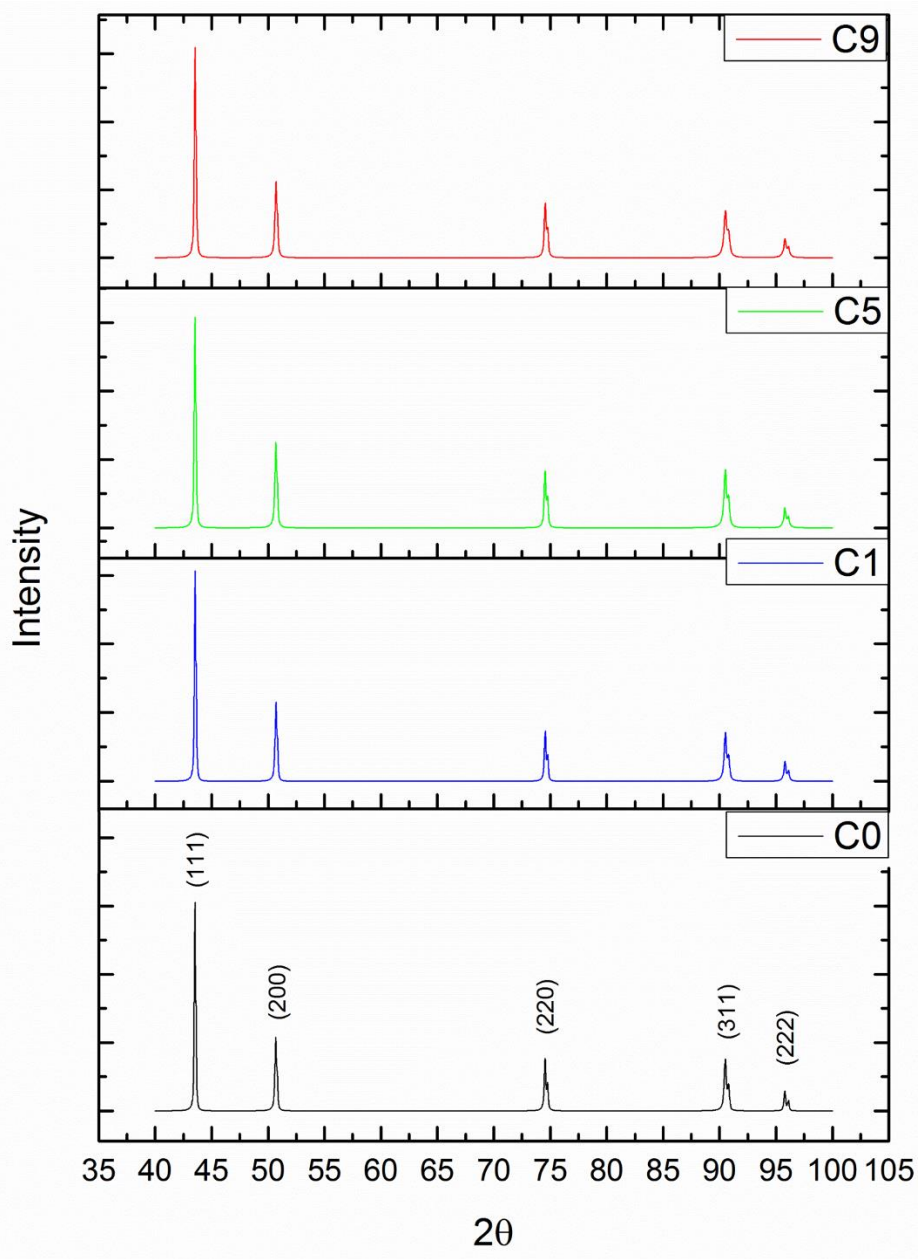

Figure 1.5. All XRD scans from C0, C1, C5, C9 are consistent with austenitic stainless steel.

XRD was also performed on the black powder that was collected from the LENS® chamber after C1 depositions, the spectrum is shown in Figure 1.6. The additional peaks in this scan were identified as alpha-Fe of the BCC crystal structure, indicated with blue stars, showing that the black powder undergoes a phase transformation as a result of the energy of the melt pool.

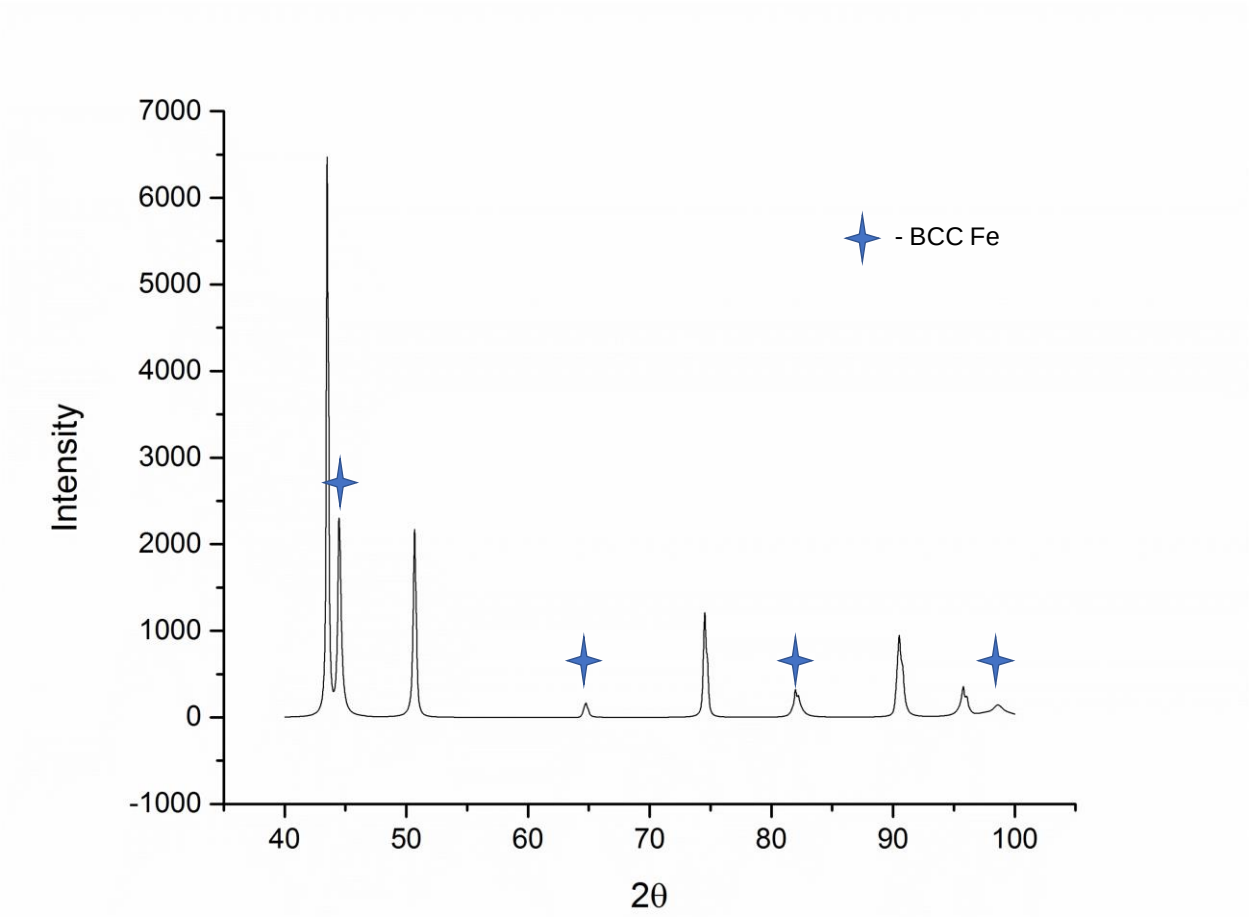

Figure 1.6. XRD scan of fine black powder collected from chamber. Scan shows extra peaks identified to be synthetic iron in BCC crystal structure.

1.4.1.2. Chemical Analysis:

1.4.1.2.1. Bulk Analysis:

Bulk chemical analysis of powders from C0 through C9 are shown in Table 1. and indicate minor fluctuation of trace elements through each cycle. The only element concentration that displays a consistent trend is oxygen which appears to increase steadily from C0 to C9, as highlighted from Figure 1.7.

Table 1.1. Bulk chemical analysis of powders from C0 through C9.

Cycle	Fe [wt%]	Cr [wt%]	Ni [wt%]	Mo [wt%]	Mn [wt%]	Si [wt%]	N [wt%]	C [wt%]	P [wt%]	O [wt%]	S [wt%]
0	66.20	17.40	12.60	2.24	0.860	0.670	0.099	0.016	0.011	0.018	0.0037
1	66.20	17.40	12.60	2.25	0.870	0.680	0.096	0.016	0.009	0.018	0.0036
2	66.20	17.40	12.60	2.25	0.870	0.680	0.093	0.016	0.012	0.020	0.0037
3	66.20	17.40	12.60	2.25	0.870	0.680	0.095	0.016	0.012	0.020	0.0038
4	66.20	17.40	12.60	2.25	0.880	0.680	0.094	0.017	0.014	0.022	0.0037
5	66.10	17.40	12.60	2.26	0.890	0.680	0.096	0.017	0.014	0.023	0.0037
6	66.10	17.40	12.60	2.26	0.880	0.680	0.095	0.017	0.011	0.024	0.0036
7	66.10	17.40	12.60	2.25	0.880	0.680	0.090	0.017	0.012	0.025	0.0037
8	66.10	17.40	12.60	2.25	0.890	0.680	0.098	0.017	0.013	0.027	0.0036
9	66.10	17.40	12.60	2.25	0.880	0.680	0.095	0.017	0.012	0.027	0.0036

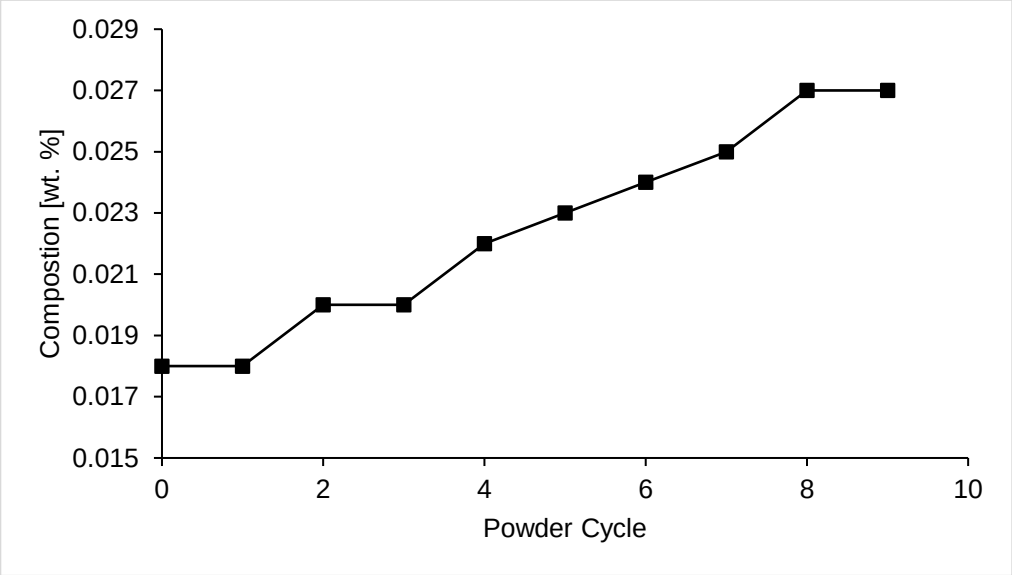

Figure 1.7. Change in oxygen content by weight percent from C0 through C9.

The steady increase in oxygen through the increased reuse of powder could be attributed to continued exposure to atmosphere during powder processing between deposition cycles, allowing an increase in surface oxides to form. The LENS® chamber environment was kept below 20 ppm oxygen content during all depositions and below 5 ppm for the test builds.

Ardila and Tang reported small changes in elemental composition of their alloys over time during their powder reuse studies due to oxidation [14], [15]. Ardila reported a decrease in Ni content of reused IN718 and attributed this to increased oxidation but showed no evidence of varying oxygen content. Tang showed oxygen content as increasing in the Ti-6V-4Al powders with repeated reuse that corresponded with decreases in Al and V weight percent. Neither study reported an effect of these composition changes on the build properties.

Elemental composition was also evaluated by EDS on powder cross-section samples from C0, C1, C5, and C9. These data, shown in Table 1.2, are used as a comparative representation between cycles and omits the composition of carbon due to limitations of the detector [25]. Other elements that were scanned for are included in the data set with 0 wt.% to indicated that they were not detected. Three sites were tested for elemental analysis from each cycle's cross-sectional sample of powder. The EDS scan on one particle in C9 resulted in a concentration of 0.31 wt.% of Cu while all other scans in C9 and the other cycles showed 0 wt.% of Cu. The average concentration of the C9 powder scans, 0.1%, is included in Table 1. to represent the data obtained. This addition of Cu is also used in the calculations of FN for the powder from C9 to show the effect of this amount of Cu on the Ni_{eq} calculated per Equation 1.2 compared to the other cycles.

Table 1.2. Compositional analysis of internal cross-sections of powder particles from C0, C1, C5, and C9.

Element	C0 wt%	C1 wt%	C5 wt%	C9 wt%
Fe	64.9	67.2	67.3	64.7
Cr	17.7	18.3	18.2	18.7
Ni	12.9	11.0	10.8	12.3
Mo	2.0	2.2	2.2	2.6
Mn	1.1	0.5	0.6	1.1
Si	0.7	0.8	0.9	0.7
N	0.7	0.0	0.0	0.0
P	0.0	0.0	0.0	0.0
S	0.0	0.0	0.0	0.0
Cu	0.0	0.0	0.0	0.1
Nb	0.0	0.0	0.0	0.0

The compositional data collected from both techniques show variations in weight percent through the cycles, however the EDS values have higher fluctuations and is an indication of the inaccuracies of the technique. The bulk data from Table 1. were used for determining the ferrite number for the powders with the addition of the Cu and Nb concentrations from EDS scans of powder cross-sections. These elements were not tested by the same methods in Table 1.1.

Cr_{eq} and Ni_{eq} were calculated according to Equation 1.1 and 1.2, respectively, for all cycles of powder. Table 1. shows the results of these calculations of the select cycles that were also analyzed for composition by EDS. The resulting Cr_{eq} /Ni_{eq} was consistent throughout all cycles leading to a consistent FN of ~0.6 representing a primarily austenitic structure for all powders. The typical range for 316L SS FN is between 0-2 [26]. It can be seen from Table 1.3 that the addition of copper to the Ni_{eq} equation for austenite stabilizers has no effect on the resulting FN. In fact, the development of a generalized model for predicting FN based on quantified significance of individual elements reports that the influence of Nb and Cu is insignificant in ferrite number calculations for stainless steels [27].

It should also be noted that the FN estimations from these equations and diagrams are highly dependent on the processing conditions. These values have been developed for welding applications where the solidification process is much slower than DED solidification.

Table 1.3. Calculations of Cr_{eq} and Ni_{eq} for bulk chemical analysis of powders from C0, C1, C5, C9. Ferrite Numbers (FN) were extrapolated from the WRC-1992 diagram.

Cycle	Cr_{eq}	Ni_{eq}	Cr_{eq}/Ni_{eq}	FN
0	19.6	15.1	1.3	0.6
1	19.7	15.1	1.3	0.6
5	19.7	15.1	1.3	0.6
9	19.7	15.1	1.3	0.6

1.4.1.2.2. Surface Analysis:

The surface chemistry was analyzed for C0, C1, C5, and C9 powders using EDS, the results are shown in Table 1.4. EDS measurements were taken from particle surfaces that presented similar features in each cycle that was examined. The features are surface contaminants and oxides of Mn and Si as can be seen in Figure 1.8 showing the scanned area from a C9 particle. The color EDS mapping shows that the dark spots on the surface of particles in the electron image are mainly rich in oxygen, manganese, and silicon. These features were found to be typical for all cycles. The weight percent fluctuation in values for all elements in Table 1.2 is attributed to the inaccuracies inherit in scanning the spherical surface of particles with the EDS detector [25] as well as the relative amount of surface contamination between each region of interest.

Table 1.4. EDS surface chemistry of morphology samples of powders tested from select cycles.

Element	C0 wt%	C1 wt%	C5 wt%	C9 wt%
Fe	65.4	62.2	65.2	62.9
Cr	18.5	18.9	18.9	19.0
Ni	12.5	12.4	11.5	11.3
Mo	2.3	2.9	1.8	2.2
Mn	1.3	1.4	1.2	1.5
O	1.1	1.2	0.8	2.2
Si	0.7	1.0	0.6	1.0
N	0.0	0.0	0.0	0.0
P	0.0	0.0	0.0	0.0
S	0.0	0.0	0.0	0.0
Cu	0.0	0.0	0.0	0.0
Nb	0.0	0.0	0.0	0.0

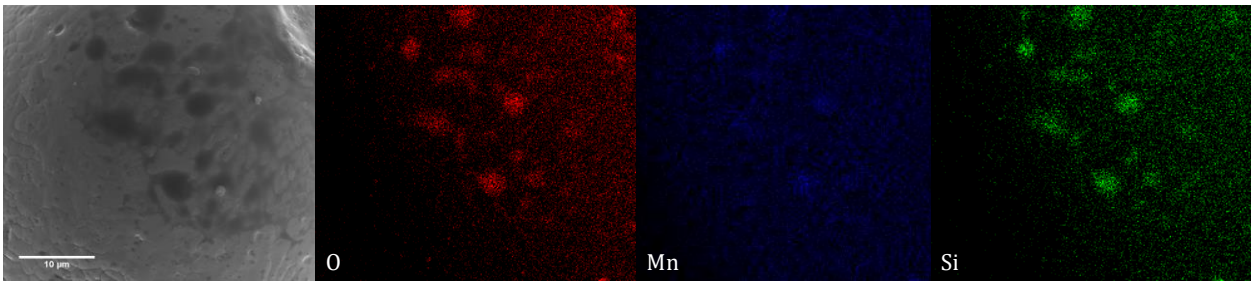

Figure 1.8. EDS elemental mapping of scanning electron image from the surface of a powder particle from C9. Color mapping shows the dark spots in electron image are oxides consisting of O, Mn, and Si.

High-resolution XPS scans were performed on particle samples for C0, C1, C5, and C9. The surface scans show strong peaks of mainly Fe, Cr, Mn, and O. The oxygen profiles are shown in Figure 1.9. The profile data of peak position and concentration percent (% Area) are also listed for each cycle. To evaluate the change in concentrations properly, the percent atomic concentrations from the deconvoluted peaks were calculated as the ratio of intensity to the total intensity of electrons in the measurement of the profile [28]. This calculation was performed for the main peak of O 1s profiles and show that the concentration of oxygen does increase from C0 to C5 and then drops again at C9, though not below the initial value of C0. These results are shown in Table 1.5. The percent atomic concentration for Fe, Cr, and Mn

follow the same trend as the oxygen for C0, C1, C5, and C9. The iron scan was identified as a profile characteristic Fe_2O_3 oxide with the main peak at 710.8 eV bonding energy [29]. This scan profile is the same for all powders tested as seen in Figure 1.10. Chromium scan profiles show bonding energies for Cr_2O_3 at 576.5 eV, and manganese bonding energies represent Mn_2O_3 [28]. All XPS scans show there is an increase in the metal oxides on the surface of powder particles from the reuse of powder supporting the increase in oxygen content from C0-C9 from the bulk chemical analysis. However, it would be expected to have a corresponding change in concentration of the bonding elements. XPS analysis at a higher resolution than 200 μm per scans, would provide more detail on the individual particle surface chemistry.

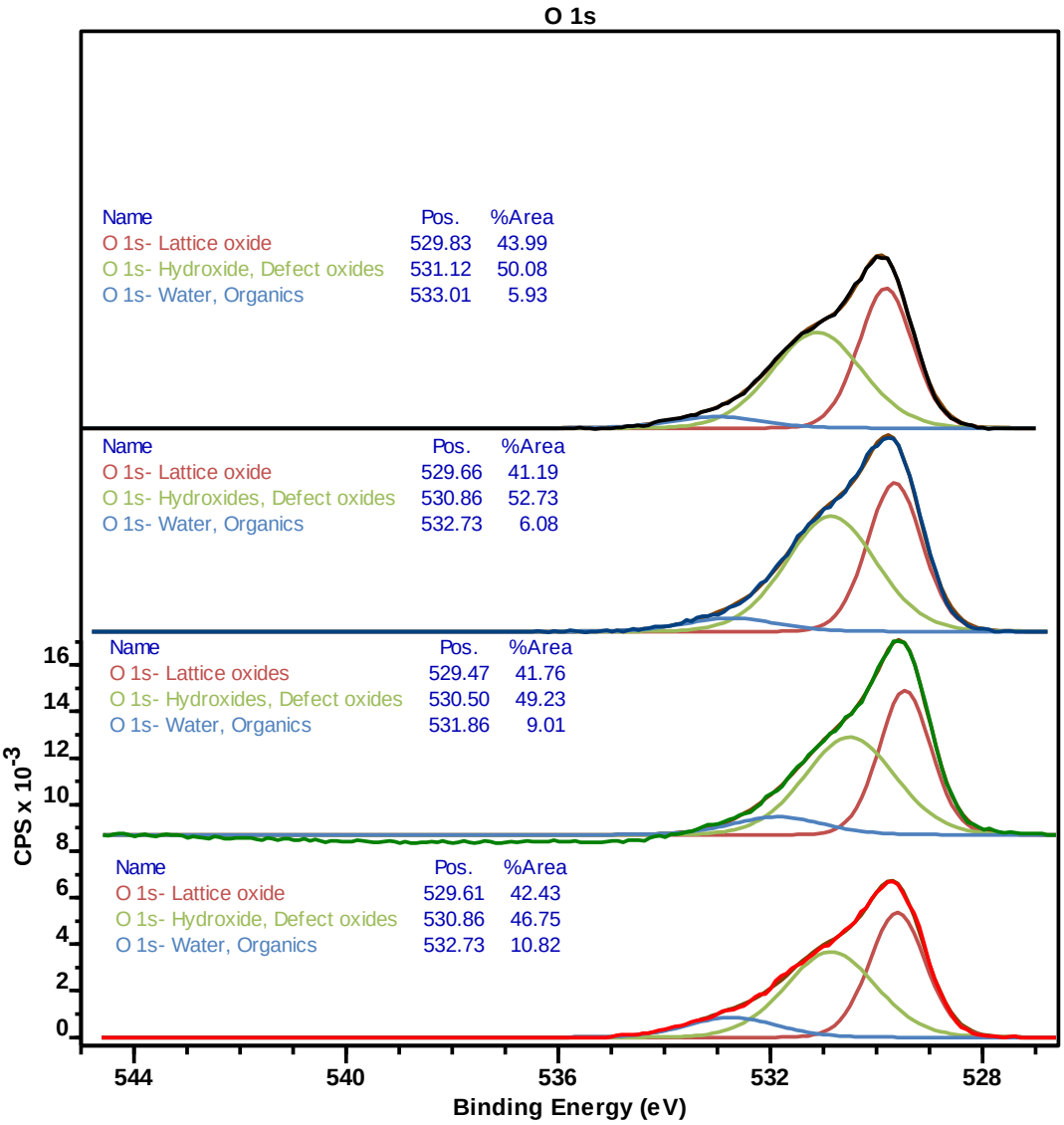

Figure 1.9. XPS scans showing oxygen profiles for C0, C1, C5, and C9 including peak areas used to calculate percent atomic concentrations.

Table 1.5. XPS data extrapolated from the main peaks of oxygen profiles of C0, C1, C5, and C9.

O 1s	% Concentration	Intensity	% Atomic Concentration
C0	42.4	5344	126
C1	41.8	6180	148
C5	41.2	63234	154
C9	44.0	5977	136

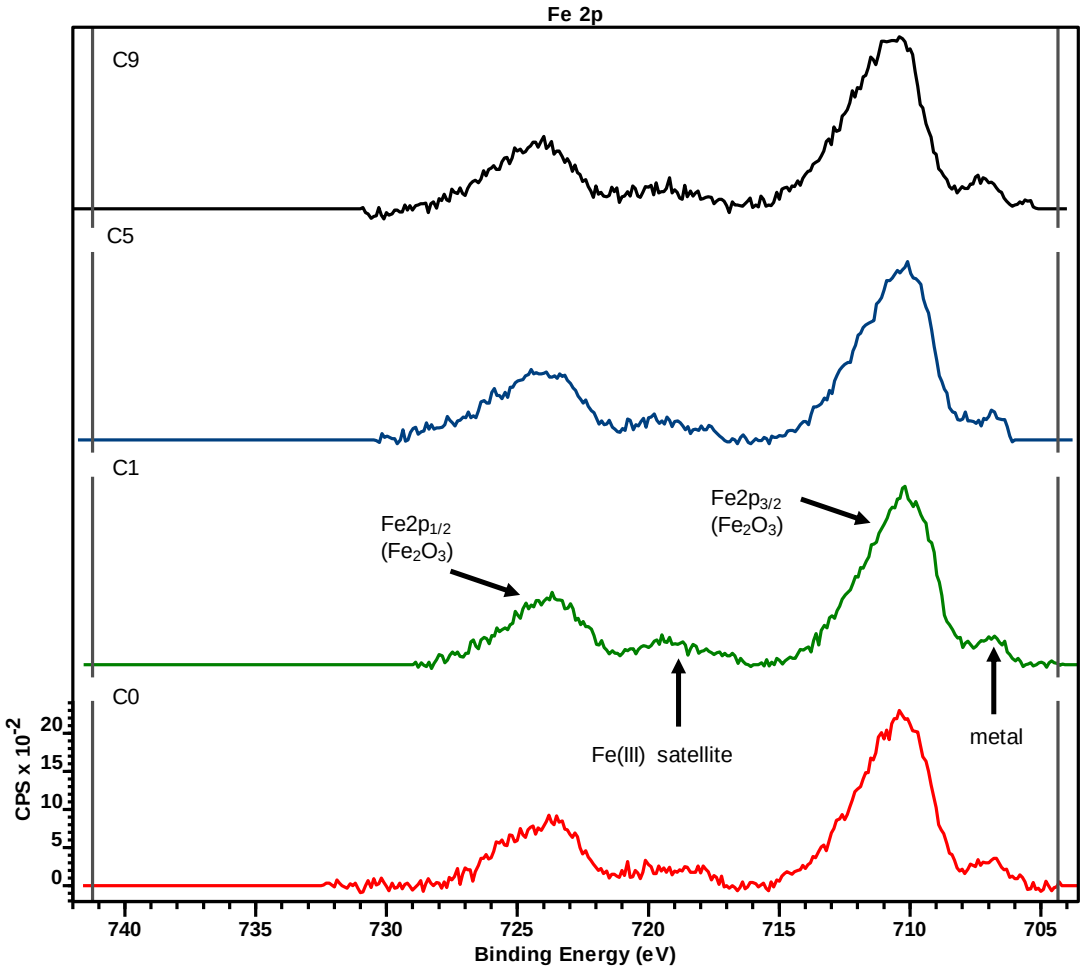

Figure 1.10. XPS scans showing Fe profiles of Fe3+ in iron oxides for C0, C1, C5, and C9.

1.4.1.3. Particle Size Distribution:

The particle size distribution (PSD) determined from sieve analysis is shown in Figure 1.11 as a log plot of representative cycles. From this plot there is little deviation between the amount of powder in each sieve from C0 to C9. The largest variation in this plot occurs in the amount of larger particles found in the 106 µm sieve. The call outs in Figure 1.11 highlight the defining cycles. C0 and C5 had the most particles with a diameter larger than 106 µm. C2 contained the least number of particles in that sieve size. The rest of the cycles fell somewhere in between. The sieve analysis was done mainly to remove any large agglomerates from the reused powder after each deposition cycle, thus these agglomerates

were created during each cycle. Figure 1.12 shows the variation in number of agglomerates created in each cycle by weight percent. These are the agglomerates measured during full PSD sieve analysis only. The change in amount of agglomerates is thought to be influenced by the size of parts that were deposited during each cycle, therefore the amount of particles larger than 150 µm could be partially dependent on what was built with the powder selected for PSD. It was observed that more agglomerates would form during the deposition of either a larger part or under certain melt pool conditions created by different deposition parameters, namely higher powder feed rates or power settings. As a part builds up further from the substrate, the heat sink path becomes narrower and the cooling rates decrease. With increased energy of the melt pool there is an increase in back splatter of partially melted particles that would stick to the nozzles and build up over the deposition time [30].

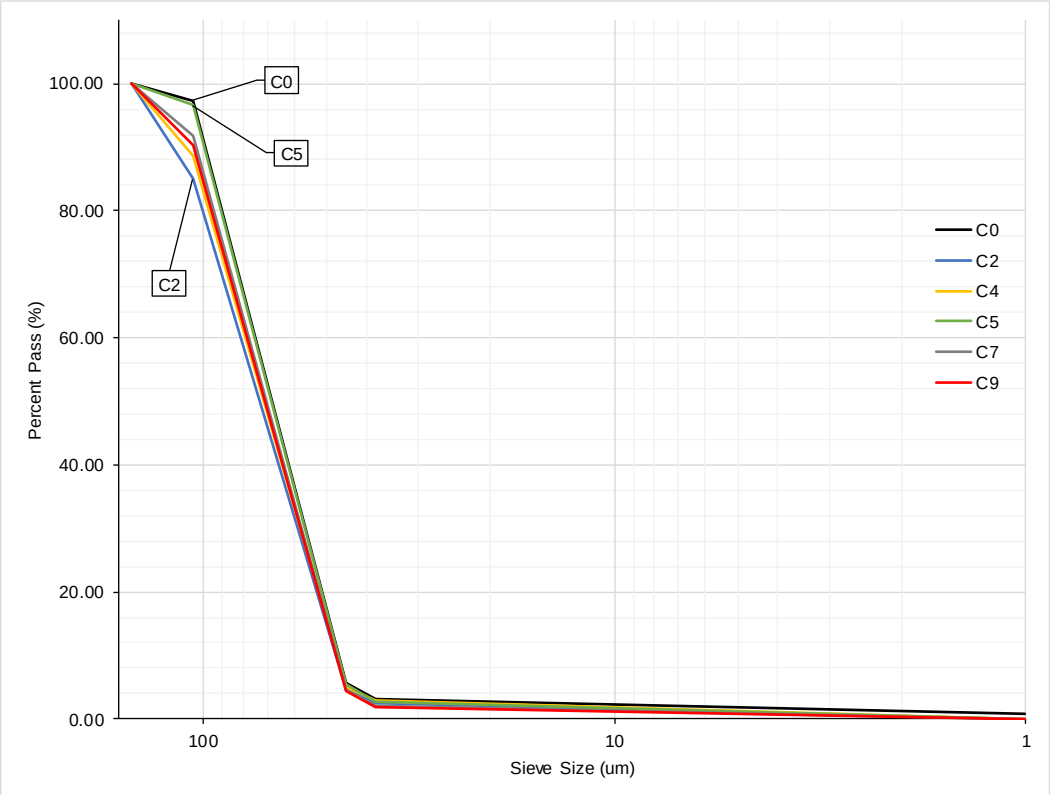

Figure 1.11. PSD as determined from sieve analysis represented on a log scale.

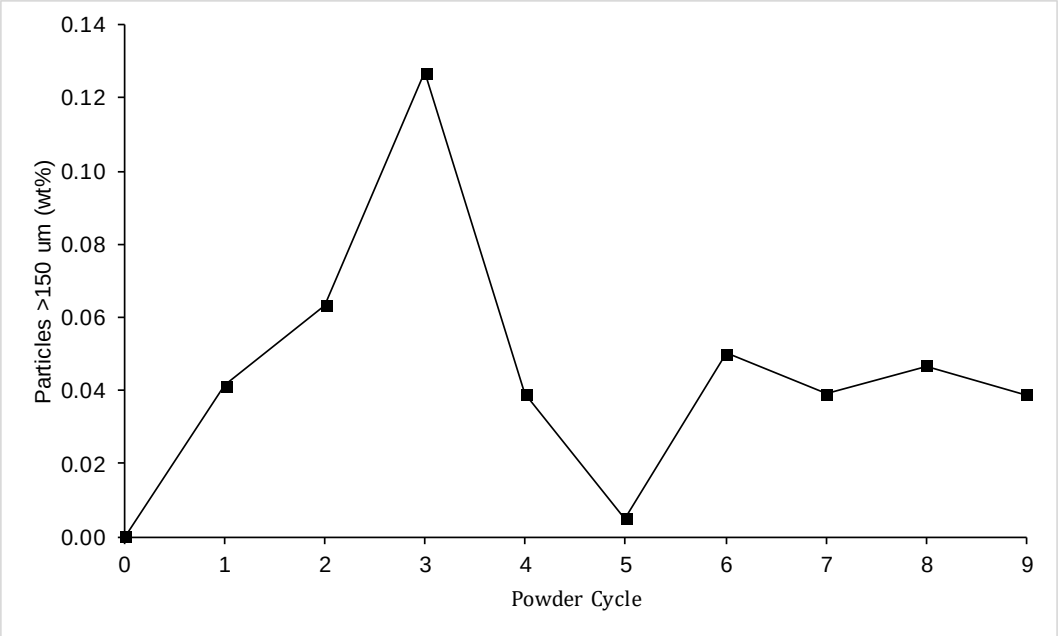

Figure 1.12. Weight percent of particles with diameters larger than 150 μm created after each cycle of deposition.

A closer look at the trend of the smaller particles, <38 μm, from the sieved PSD analysis in Figure 1.13 shows small fluctuations in the first few cycles. After C3 the percentage of smaller particles generally decreases with continued reuse, yet only by < 1.0 wt.%.

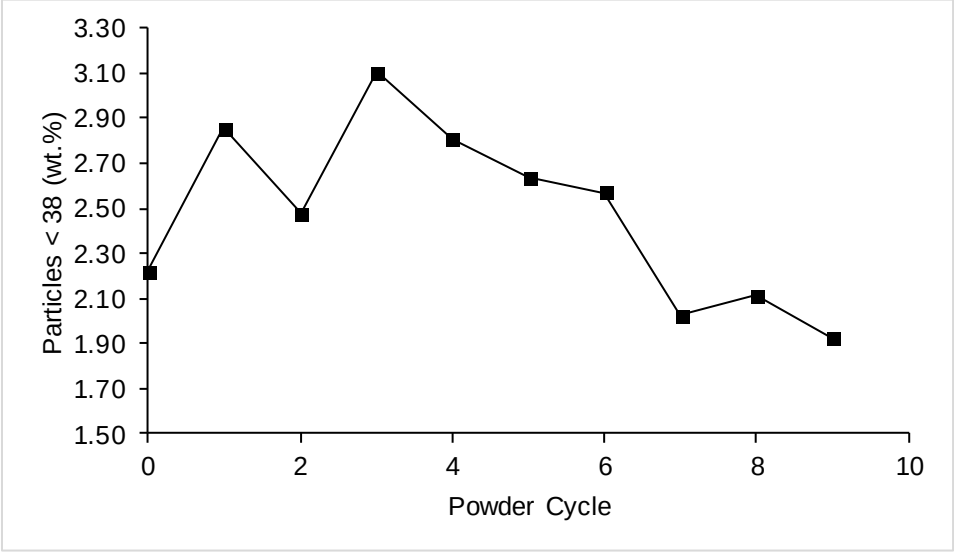

Figure 1.13. Weight percent of particles with diameters smaller than 38 μm from sieving PSD of all cycles.

For a more detailed distribution of particle size, SEM micrographs of morphology samples of powders from C0, C1, C5, and C9 were analyzed with the OM particle analysis software. The resulting PSD is shown in Figure 1.14 and displays a large number of particles with diameters less than 20 µm. This amount decreases with increased reuse. One explanation could be that the smaller particles are less likely to break the surface tension of the melt pool [25] and more likely to be from carried away stage by the turbulence of the argon carrier gas as the deposition head rasters back and forth [15]. Smaller particles have also been found to tend toward agglomeration [31] and therefore could be contributing to the increased mean particle size of C9 compared to C0. Figure 1.15 (a) shows an agglomerate >150 µm in size that consists of mostly smaller particles ranging 10-80 µm. This particle was removed during sieving of C3. Image (b) shows an agglomerate <150 µm from C5 of particles ranging 1-15 µm in size. Particles of this type explain the trend of decreasing amount of particles smaller than 30 µm with increase reuse.

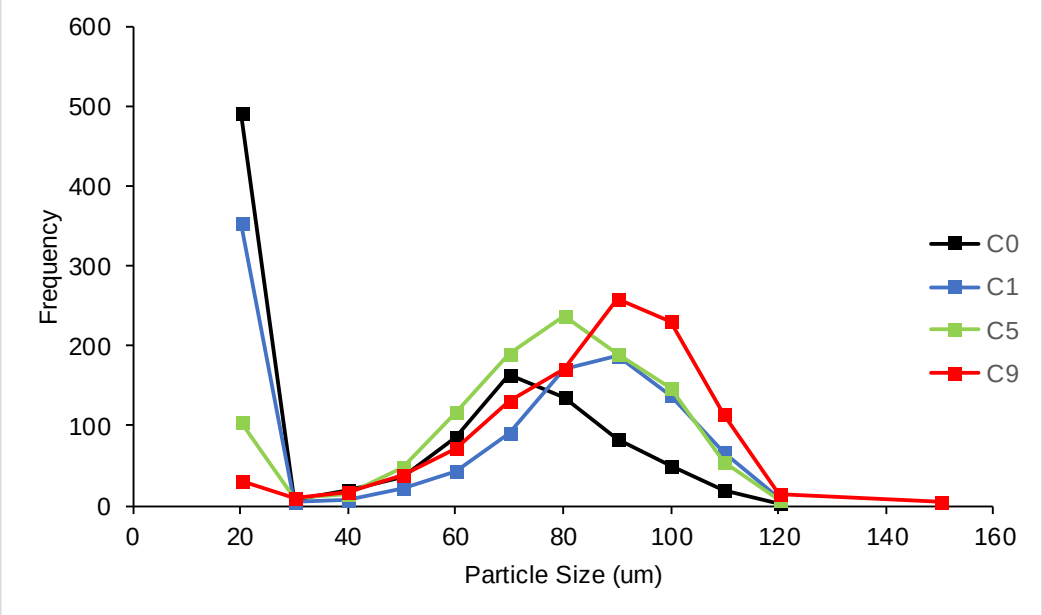

Figure 1.14. Morphology PSD observed from SEM images by OM Stream Basic software.

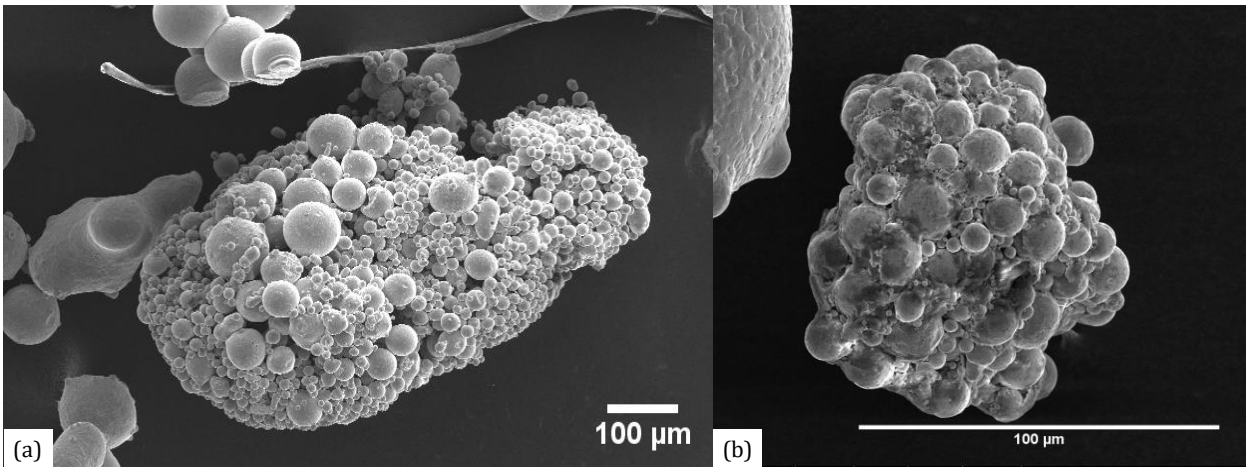

Figure 1.15. Agglomerates from (a) C3 that was removed during sieving and (b) C5 that remained in reuse production after sieving.

A cumulative plot of the morphology PSD data is shown in Figure 1.16 on a log scale. This allows the mean particle size, labeled as the D50 value, for each cycle to be determined. The plot shows the D50 value increases from 50 µm in C0 to 83 µm in C9 while also clearly showing the decrease in smaller particles with increased reuse.

The discrepancy between the plots for sieved PSD and morphology PSD is attributed to sample size and resolution. While the morphology samples and OM software allow for a larger distribution of particle sizes to measured, the number of particles observed from the images is a fraction of those analyzed by sieved PSD. By quantitatively analyzing more morphology samples it is believed that the frequency of smaller particles compared to larger particles would more closely resemble that of the sieved data. The current collection of PSD analysis allows the general trends to be observed while the proportions may not be accurate.

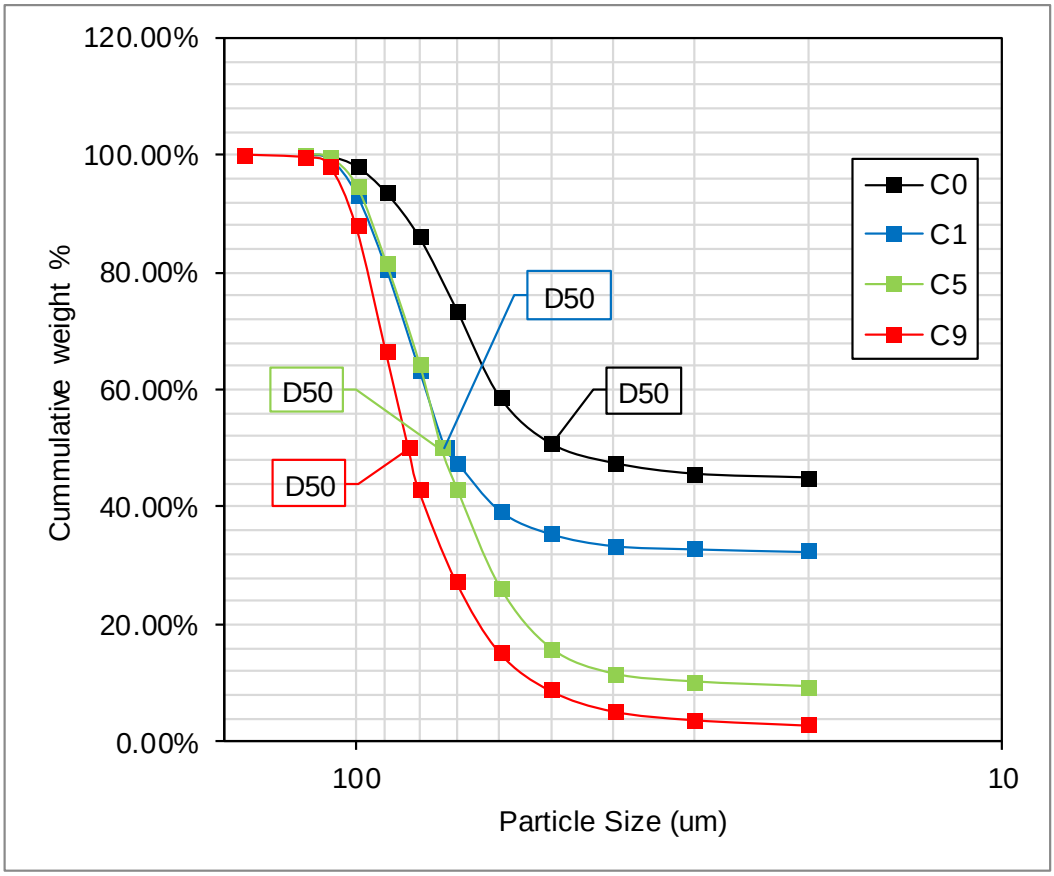

Figure 1.16. Morphology PSD of C0, C1, C5, C9 powder size distribution showing D50 values for each cycle.

1.4.1.4. Morphology:

Powder particles from C0, C1, C5, and C9 were imaged in the SEM to evaluate surface morphology and shape. Micrographs from each cycle are shown in Figure 1.17 and show consistent trends in each cycle. Every cycle contains particles with satellites as well as particles that remain mostly spherical. Images (a) from all cycles tested show similar porosity in particles that appear to be partially hollow. Image C0 (b) as well as C9 (a) show elongated particles that are commonly observed in AR powders. Images (b) and (c) from each cycle show examples of particles that exhibit partial remelting characteristics resulting in agglomerates of irregular shapes. These particle features could be from interactions with the laser or the result of the atomization process because they also appear in the C0 powder.

C1, C5, and C9 contain particles that remelted from laser contact causing agglomeration and/or smooth surfaces mixed with solidification ripples. These ripples are most apparent in the particle marked with a blue star in C1 (b). This type of change in particle morphology is likely caused when particles melt from contact with the laser prior to interaction with the melt pool. Depending on the timing, these particles could solidify too quickly and become partially remelted to another particle or surface [1]. In the case of the particle in C5 (b), marked with a red star, the particle was remelted and then segregated resulting in the flattened edge. From these images, it is clear that some particles experienced interactions with the laser while it is possible that other particles did not throughout the ten cycles.

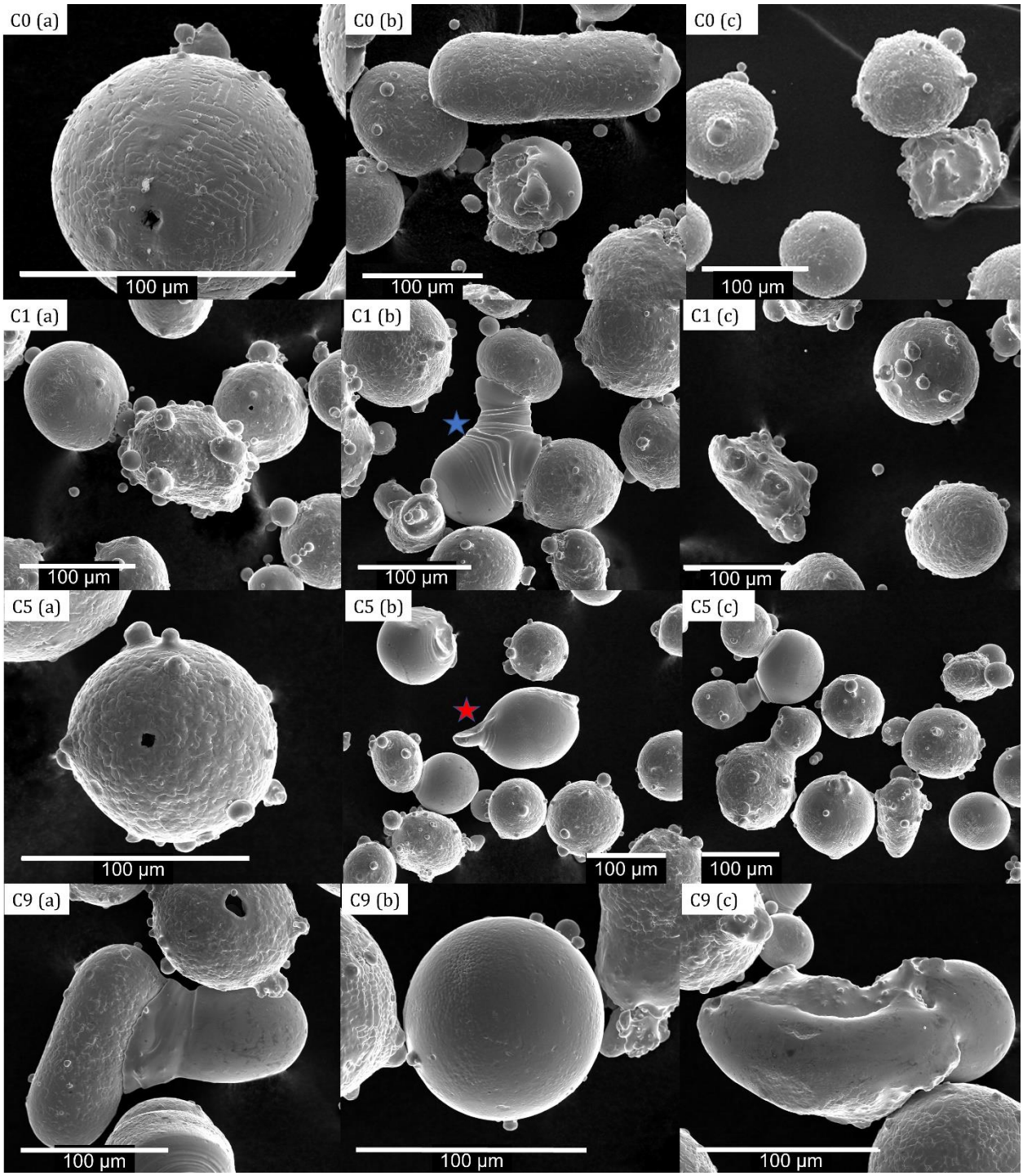

Figure 1.17. SEM micrographs of powder from C0, C1, C5, and C9 showing particle morphology and shape. All scale bars are 100 µm.

With similar features of shape and morphology being evident in each cycle it is difficult to quantify any changes without further analysis. These micrographs of morphology were used to quantify the changing shape of the powders in terms of sphericity. To do this, the OM

particle analysis software was again used and the resulting data is shown in Figure 1.18 as a log plot with cumulative percent. Sphericity is scaled from 0 to 1.0, with 1.0 being a perfect sphere.

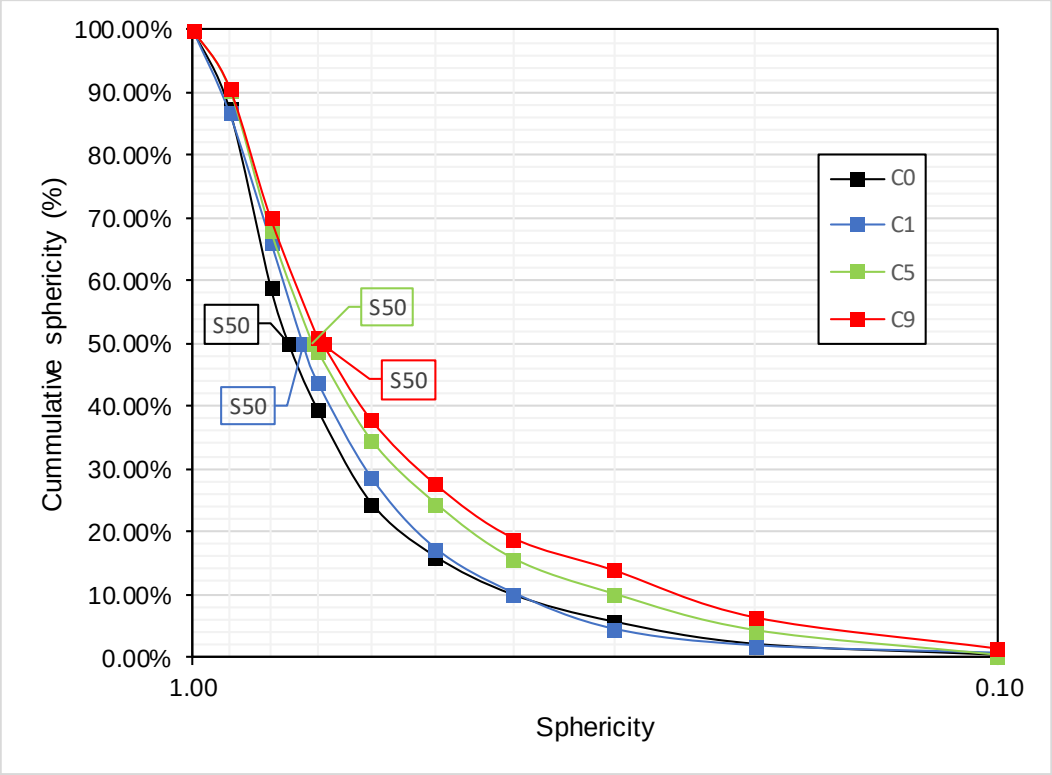

Figure 1.18. Sphericity as determined from morphology samples of C0, C1, C5, C9.

The curves in Figure 1.18 show that with increased reuse the mean sphericity of the particles, S50, decrease indicating that they become more irregular in shape. While the mean particle size is increasing, Figure 1.16, the particles are becoming more irregular. The shape of powder particles influences the interparticle interactions as well as laser interactions [25]. Particles that are spherical in shape will exhibit less friction with other particles than those that are irregularly shaped [32]. This can greatly affect other physical properties of powder such as flowability, which is discussed in a later section of this chapter.

1.4.1.5. Cross-sectional Analysis:

Micrographs of powder particles from C0, C1, C5, and C9 were analyzed for internal porosity. Fully dense particles and particles that contain pores and internal defects were found in each cycle and are shown in Figure 1.19. The porosity in each powder sample was not quantified, however there were similar pores in particles from each cycle. Image C0 (b) and C5 (b) show spherical internal pores that can be attributed to the atomization process [16]. The pores in C9 (b) however are rather large and were not observed in earlier cycles. It is possible this is due to remelting and agglomeration but difficult to confirm without viewing the rest of the particle. The features of particles in images C1 (a) and (b) and C5 (a) show a different kind of porosity that can best be described as the result of an unmelted particle within a particle. This was not seen in any particles from C0. There is a ring around the deformation that includes an open cavity with additional material that appears to be sintered. This area is highlighted in image C5 (a) particularly. Image C9 (a) shows a similar internal defect yet without the remanence of an unmelted particle. This view could be a cross-section at a different location of the defect or this particle could have experienced a higher degree of remelting than the particles from the previous cycles. Regardless, as seen with the morphology characterization, there are consistent features in all cycles as well as features that did not occur in C0 and are likely due to the increased reuse.

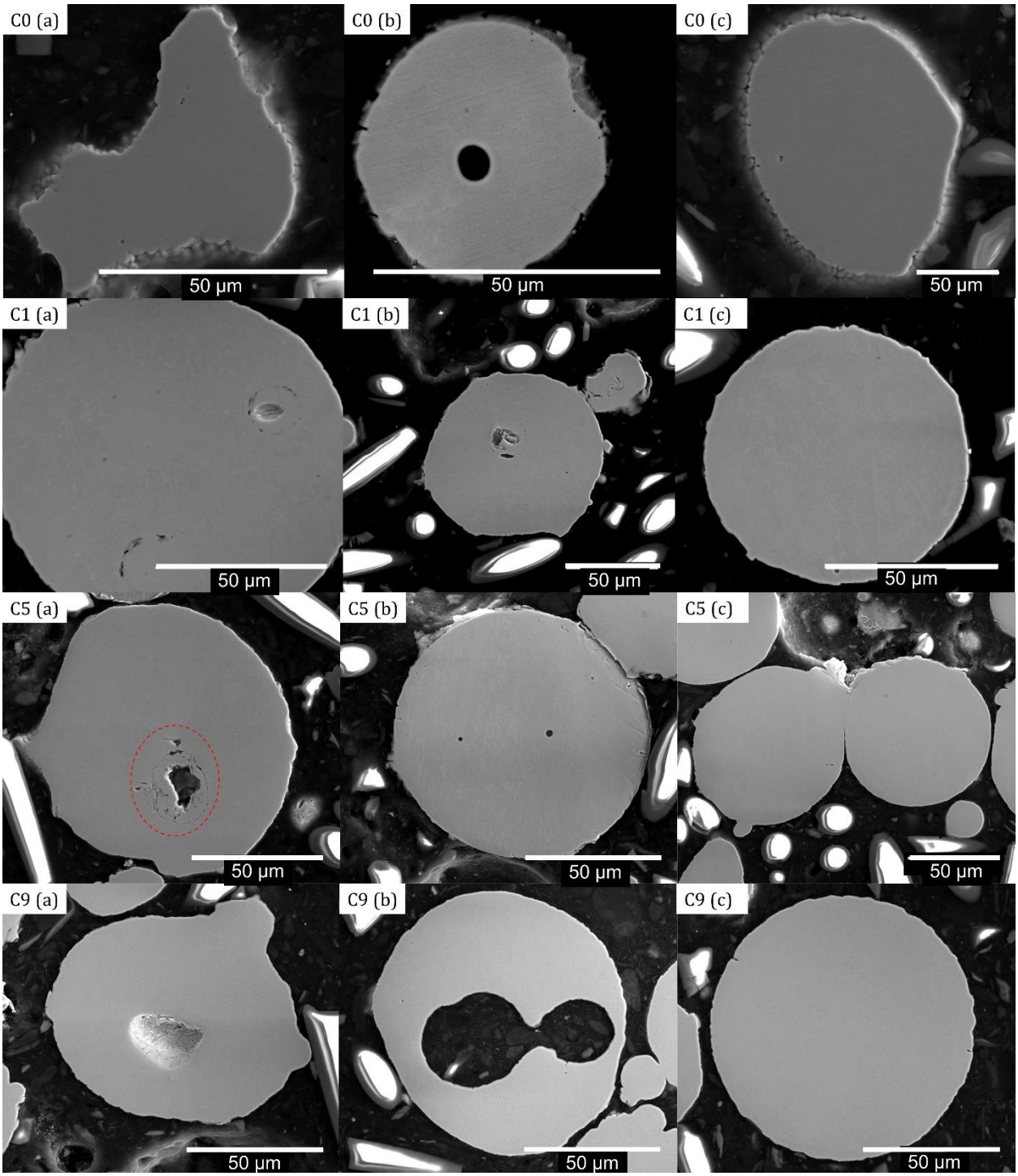

Figure 1.19. Cross-section powder samples from C0, C1, C5, C9 showing range of porosity and particle shapes found in each cycle.

1.4.1.6. Tap Density:

The Hausner ratios, calculated from the ratio of tap density to loose (bulk) density, and Carr index for each cycle are shown in Table 1.6. From both metrics, all powder cycles are classified as having good flowability because the tapped and bulk densities are close together, indicating the interparticle interactions are low. Small fluctuations in the Hausner ratio could be attributed to the change in number of smaller particles from cycle to cycle which would influence packing [33], but the tolerances are minimal and no direct correlation can be made. These values are empirical and do not provide any practical indication of the physical characteristics of the powders nor are they related to the powder behavior within the LENS® deposition process. The Hausner ratio and Carr index are simply metrics by which to compare samples quickly and inexpensively. To properly analyze the recycled powder properties, further analysis is needed on physical characteristics of powders, as discussed in the previous sections, to fully understand the inherent effects of multiple reuse in a DED process.

Table 1.6. Hausner ratio and Carr index for each powder cycle as calculated from Equation 1.3 and 1.4 respectively. Both indicate all powders are classified as having good flowability by the Hausner ratio <1.25 and the Carr index <15.

Cycle	Hausner ratio	Carr index
0	1.06	5.66
1	1.07	6.54
2	1.08	7.41
3	1.04	3.85
4	1.05	4.76
5	1.05	4.76
6	1.08	7.41
7	1.06	5.66
8	1.10	9.09
9	1.08	7.41

1.4.1.7. Flowability Measurements:

The flow rate of powder from each cycle was measured using the Hall Flow meter method. The results show that the flow rate varies from cycle to cycle but there is a general increase in flowability from C0 to C9, shown in Figure 1.20. The units of 50 g/s represent the rate for the 50 g samples to exit the funnel from the test apparatus. This trend closely resembles those of other powder reuse studies utilizing the same test procedure [16], [33].

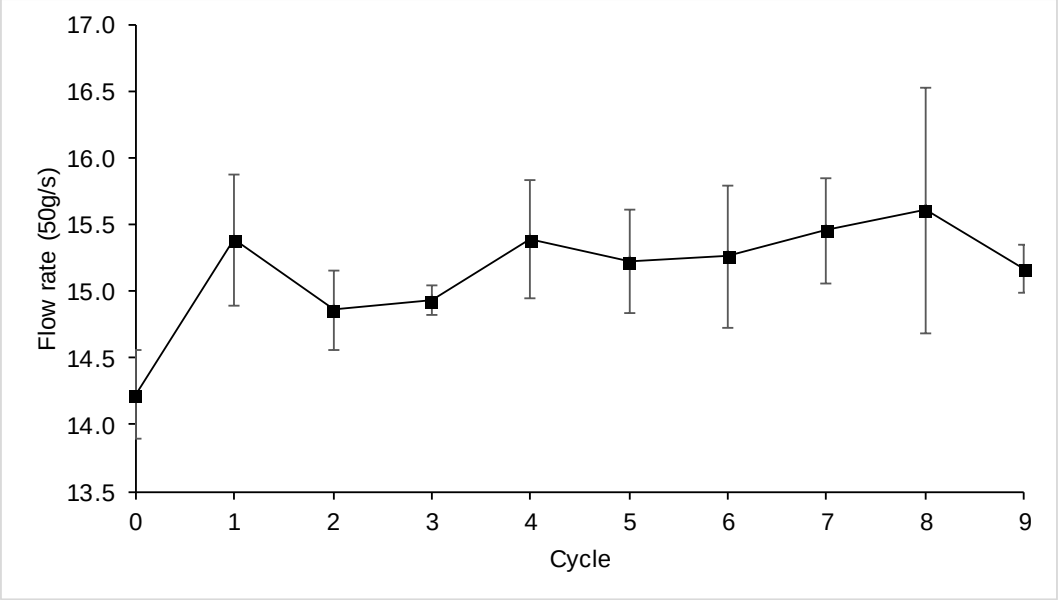

Figure 1.20. Flow rate of powder from C0 through C9 tested with Hall Flow meter method.

The second method used to track the flowability of the powder from each cycle was to measure and calculate the flow in g/min during the deposition process of similar builds with powders from each cycle. The test builds were deposited in each cycle with three different RPM values. The resulting PFR for each cycle from the three different RPM values are plotted in Figure 1.21. In comparison to the flowability determined by the Hall flow meter, the PFRs display a different response to the reused powder by decreasing in flow rate in the initial cycles then fluctuating inversely to the Hall flowability. The PFR shows an overall drop in 2.9

and 3.0 RPM while 2.8 RPM appears to have a similar flow rate in C9 as it did in C0 and thus is overall unchanged.

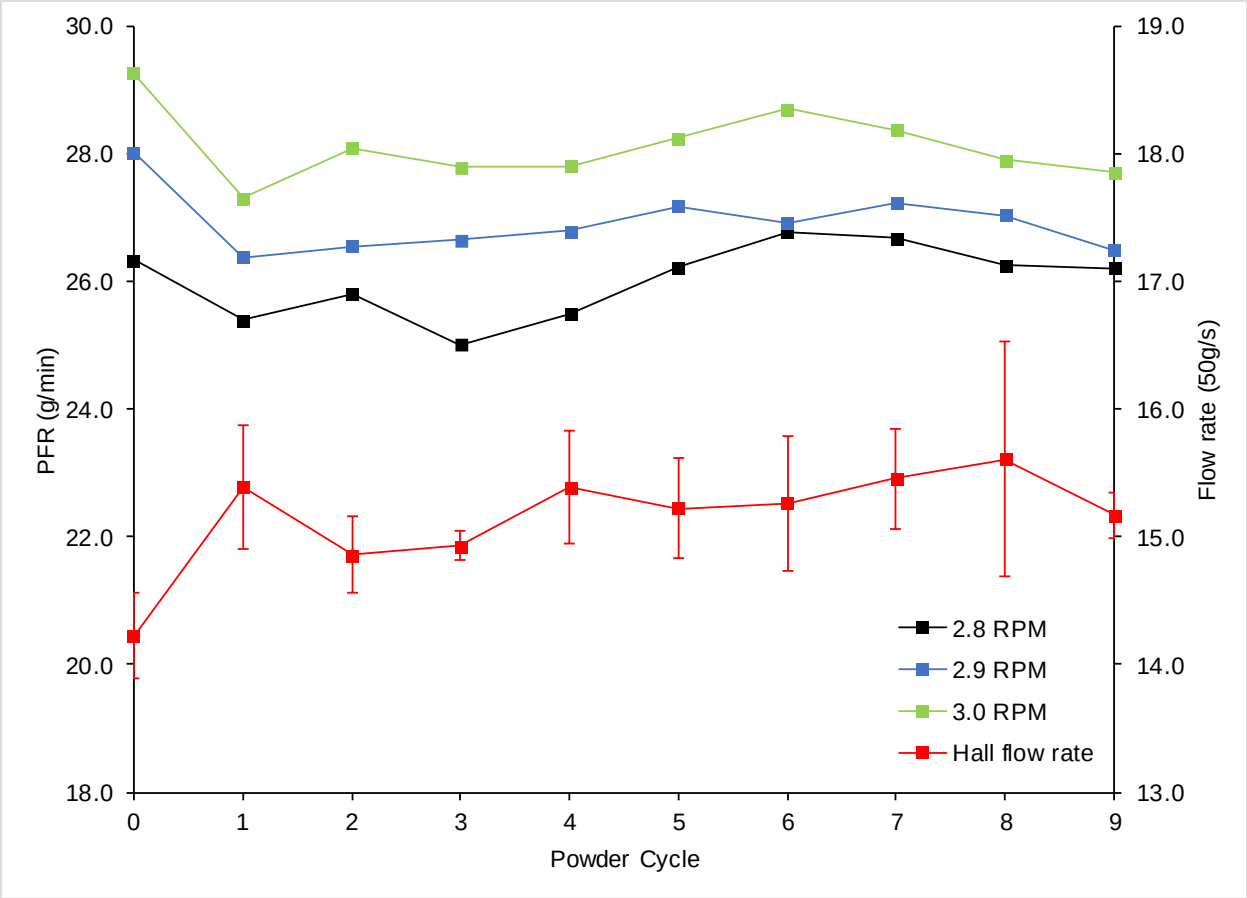

Figure 1.21. PFR of powder from C0 through C9 as measured during the LENS® deposition of the same parts with three different RPM settings compared with flow rate obtained from Hall Flow meter testing.

Flowability was also measured with the Revolution Powder Analyzer from Mercury Scientific Inc. The results of avalanche energy tests on C0, C2, and C5 powders are presented in Figure 1.22. An increase in avalanche energy corresponds to the powder riding the side of the drum longer within a rotation before collapsing back down to the bottom of the drum. The particle interactions are higher in C5, keeping them in place longer, suggesting a lower flowability. This more closely emulates the flowability measured from the PFR but only for C0 and C2. For all RPMs tested, the PFR for C5 was equal to or faster than C2.

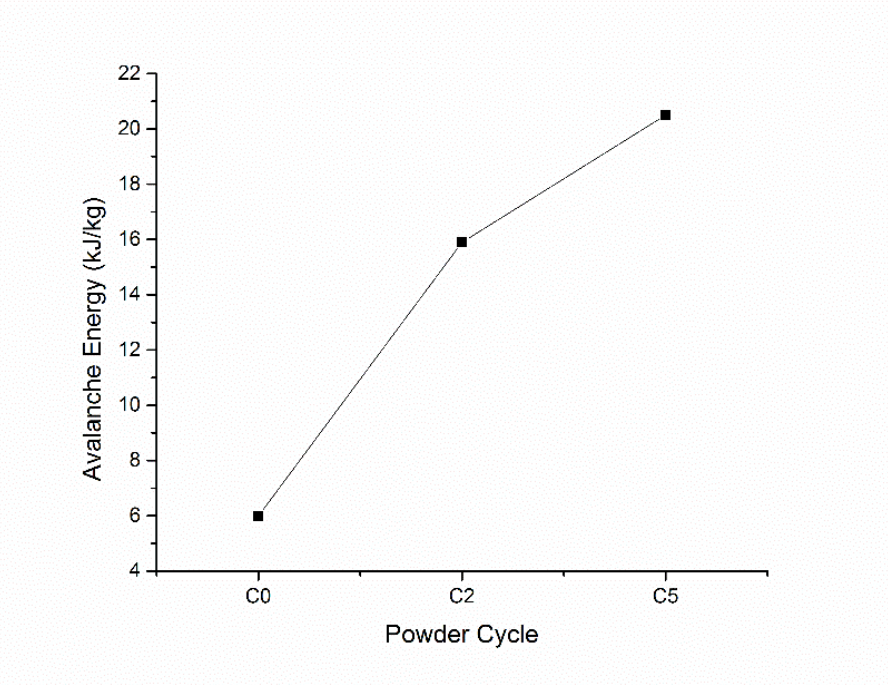

Figure 1.22. Avalanche energy reported for reuse cycles C0, C2, and C5. Powders were tested with the Revolution Powder Analyzer.

To better understand the PFRs of the reuse powders in the LENS® system, the physical properties of the particles can be correlated to their flowability. Reuse studies have reported that changes in particle size distribution and shape affect their flowability. Narrow size distributions are preferred in AM due to small particles tending to agglomerate and decrease flowability [25], [34]. Strondl et al. [35] investigated particle shape on flowability in a SLM system and found that more spherical particles yield less particle interactions, causing less interparticle friction, resulting in better flow properties. Sun et al. [32] reported sphericity decreases in powder particles reused in an EBM system with increased reuse. The irregular particles lead to an increased number of agglomerates due to interactions with the laser [25],[32]. This caused more interparticle friction and lowered the powder flowability. As shown in the previous section, the PSD in this study was narrower with increased reuse and

mean particle size increased while the sphericity of the particles generally decreased. Presumably these properties would have opposing effects on the flowability.

The sieved PSD is compared to the PFR recorded in the LENS® in Figure 1.23, focusing on the weight percent of particles less than 38 µm in diameter from each cycle since they have shown to be most affected by powder reuse in this study. The 2.8 RPM was chosen because it was used most during the test build depositions. In the first five cycles, the amount of small particles fluctuates but generally increases to C3 then drops again to C4. The PFR for 2.8 RPM generally decreases to C3 then increases to C4. From C5 through C9 the change in amount of small particles and the feed rate follow the same trend of generally decreasing.

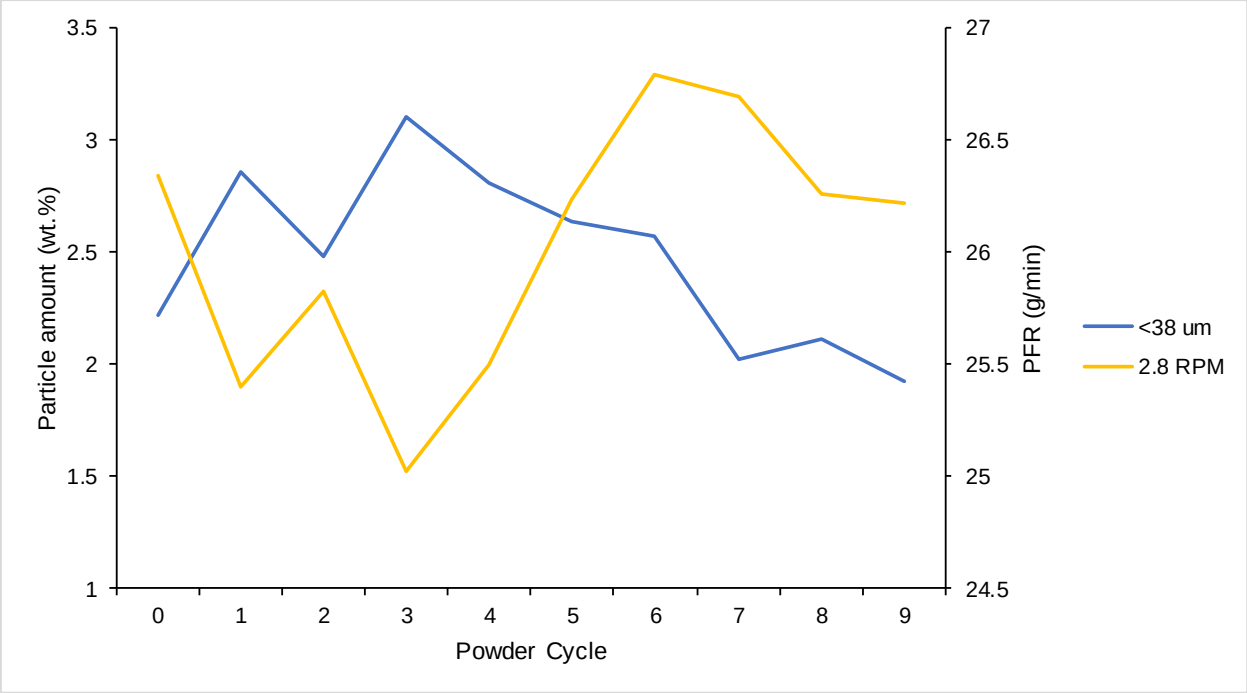

Figure 1.23. Comparison of PFR for 2.8 RPM with the changes in weight percent for particles < 38 µm for cycles C0-C9.

The plots in Figure 1.24 graphically characterize the correlation between small particle quantities and the measured PFR for 2.8 RPM. Each point in the plots represents the change in amount of particles < 38 µm and the corresponding change in PFR at 2.8 RPM from one

cycle to the next. For all ten cycles, the R^2 value for plot (a) is low, 0.57, indicating that there is only a partial correlation between the two data sets. As observed in Figure 1.23, C0-C4 appear to have a codependence so plot (a) is reduced to cover only the first five cycles and plotted in (b), producing a R^2 value of 0.99. This confirms that particle size has some influence on the PFR within the LENS® however there must be other factors to explain the flow behavior.

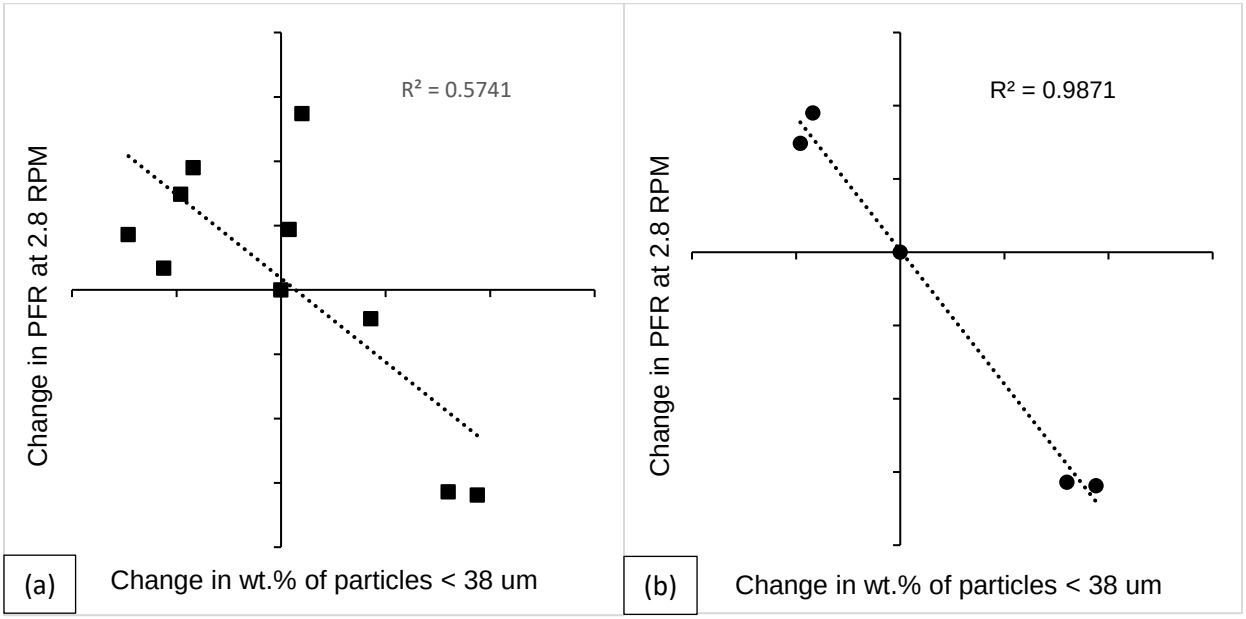

Figure 1.24. Correlation between changes in PFR at 2.8 PRM and changes in amount of particles < 38 μm from sieved PSD in (a) all ten cycles and (b) cycles 0-4.

The PSD, increase in mean particle size with narrower distribution, contributes to an increase in powder flowability. The particles in this study are also increasing in shape irregularity, which should decrease flowability. This supports the constant fluctuation in the feed rates but to understand which has a greater effect on flowability, both size and shape are compared to PFR from C0, C1, C5, and C9. The change in sphericity and the change in mean particle size are compared with the change in PFR at 2.8 RPM in Figure 1.25. The comparisons show that PFR is more dependent on the change in particle size with a higher

R^2 value of 0.77. The data used in these plots is taken from the morphology sample analysis to make an equal comparison of data, however a more comprehensive analysis of the particle shape, by quantifying more particles from all cycles, could provide more insight to the effects of increasing shape irregularity.

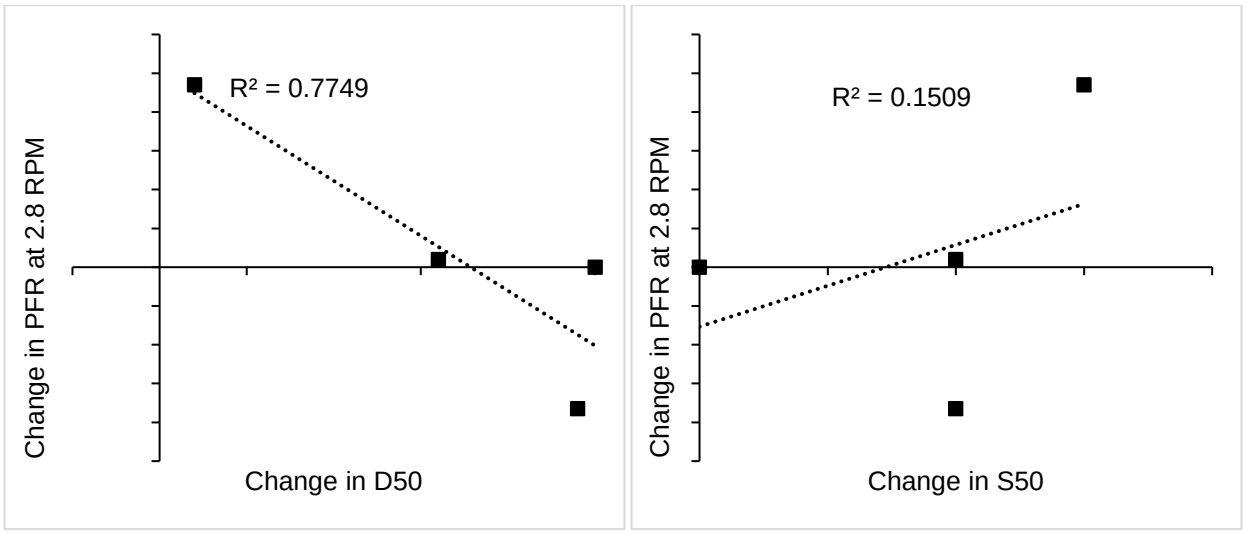

Figure 1.25. Comparison between the change in mean particle size, D50, and mean particle sphericity, S50, with the change in powder feed rate at 2.8 RPM.

From the particle size and shape data of this reuse study there is no clear trend with the measured flow rates of the LENS® process. The discrepancies can be explored by looking at the mechanisms of powder delivery within the system. The LENS® powder delivery system consists of three different sections. First, the hopper where the powder is loaded resembles a silo as shown in Figure 1.26. The powder flows out of the bottom by gravity discharge and the self-weight of the powder as a driving force in mass flow and funnel flow. Mass flow follows the first in first out scenario where all powder is in motion at once [36]. Funnel flow occurs when particles at the top of the hopper migrate to the middle of the hopper creating a central core through which the powder flows down, following a last in last out scenario. The amount of powder in the hopper also determines whether the powder is free flowing or in a cohesive state. A cohesive state occurs when more powder is present in the hopper and

the particles exhibit a compressive force on themselves. If the interparticle frictions are high, as the powder level decreases, the force of compression is outweighed by the particle friction, and flow becomes more difficult [36]. Both cases and the rates at which they occur are influenced by interparticle friction, shape, size, and quantity of the powders.

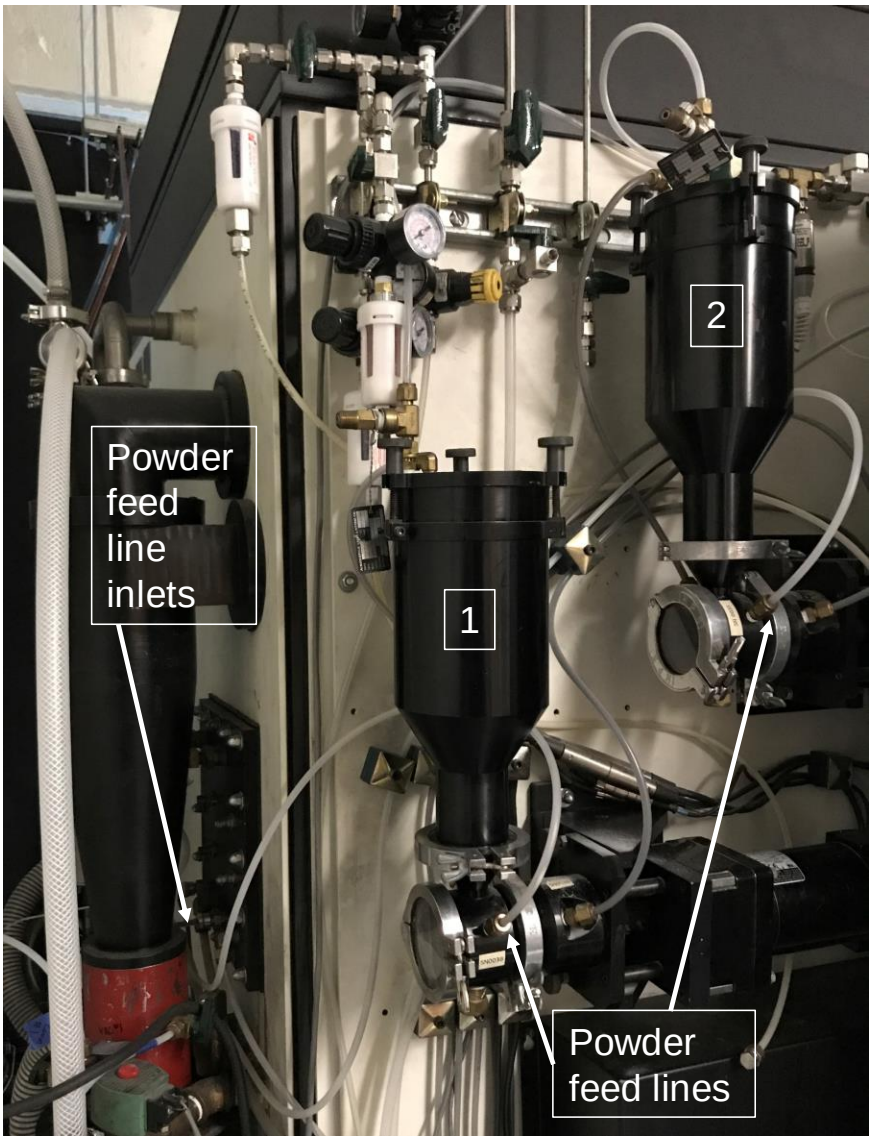

Figure 1.26. LENS® hoppers located outside the chamber with powder feed lines leading to inlets at the back of the chamber.

The next step in the powder delivery system of the LENS® is the polypropylene tubing that directs the fluidized the particles in argon gas flow from the hopper outside the chamber, Figure 1.26, to the deposition head inside the chamber, Figure 1.27. The powder

flow through the tubing is partially controlled by the RPM setting, contributing to the amount of powder leaving the hopper, and the argon gas flow rate controlled by a flow meter. The mechanism of flow in this part of the process resembles a gas-particle flow scenario where mass, density, and particle size can greatly influence the ability of the argon to carry the particles through the tubes [37]. The amount of particles that are feed through the tubes will also affect the flowability. Used tubes will have a coating of particles around the inner diameter and the feed rate will increase compared with new tubes.

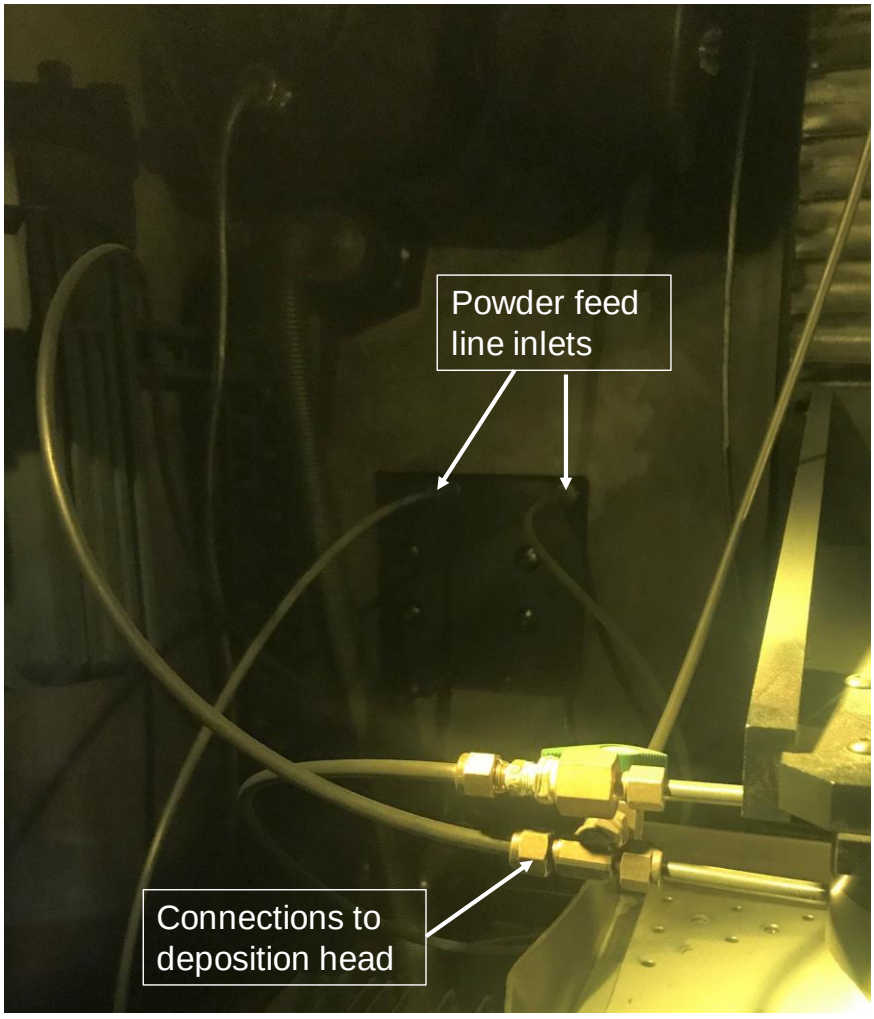

Figure 1.27. LENS® powder feed lines from the inlets to the deposition head inside the chamber.

The last process in the LENS® powder delivery system is the deposition head and nozzle assembly, Figure 1.28. The kinetic energy of the powder particles is greater than the effect of gravity [1] but the powder delivery is also effected by the size of the opening of the nozzles, the amount of powder, and particle size. Smaller particles are more influenced by the turbulence of the argon flow [15] and could be more likely to land elsewhere in the chamber than contribute to the melt pool.

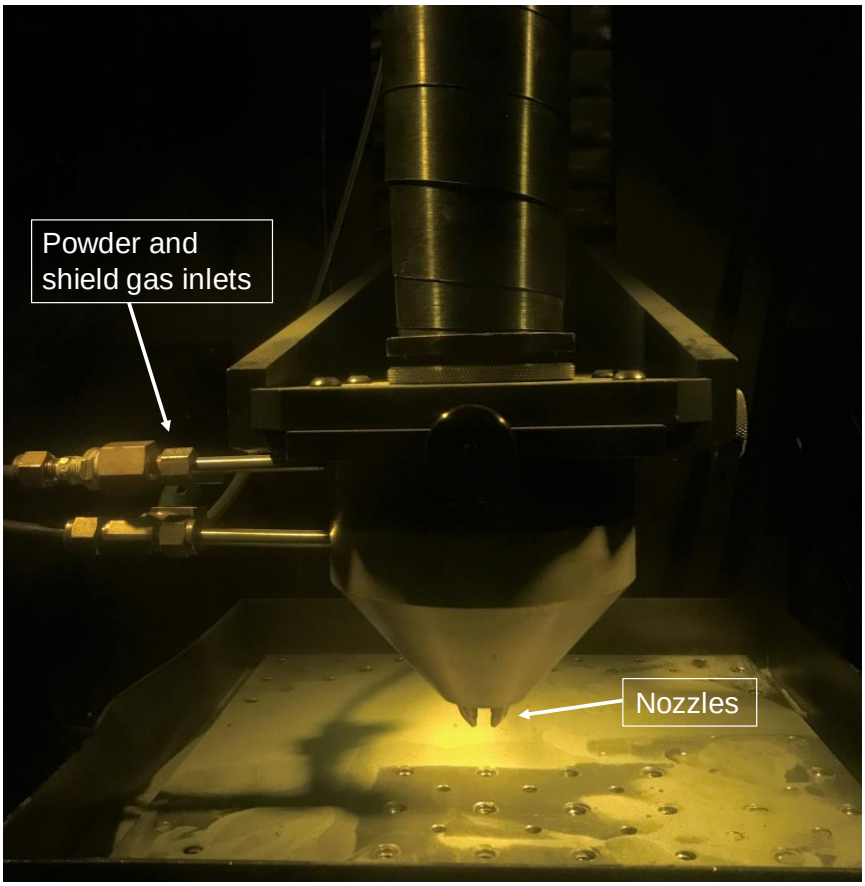

Figure 1.28. LENS® deposition head with powder and shield gas inlets and nozzles.

The complexity of the LENS® powder delivery system implies that more than one test method is needed to fully understand the behavior of powder within the machine. The Hall Flow meter best resembles the hopper step in powder delivery system of the LENS®

however, measurement techniques are needed to mimic the other two steps more accurately in order to completely explain and predict the PFR trends.

1.4.2. Process and Parts Characterization:

1.4.2.1. Powder Efficiency:

The reuse efficiency for the test builds deposited with the same geometry through several cycles was calculated to be between 67.2 - 96.8%, shown in Table 1.7. Data for C0-C3 was not available to include in this analysis. The RPM with the most efficient use of powder on average was the 2.8 setting. PFRs that resulted from 2.8 RPM were also the closest to the target PFR for fully dense parts thus having the best capture efficiency. As expected, the 3.0 RPM, which also produced the higher PFRs in every cycle, is the least efficient in depositions when all other parameters are consistent and results in the most left-over powder. The change in reuse efficiency appears to be related to process conditions, not the reuse of powder.

Table 1.7. Reuse efficiency for test builds deposited at different RPM settings for C4-C9.

RPM	C4	C5	C6	C7	C8	C9
2.8	91.5%	67.1%	95.0%	71.4%	71.8%	68.5%
2.9	84.3%	90.7%	95.0%	94.8%	86.9%	89.5%
3.0	96.0%	95.8%	96.8%	96.3%	90.5%	92.6%

1.4.2.2. Chemical Analysis:

Chemical analysis was conducted with EDS in the SEM on cross-section samples to identify internal particulates and impurities from each build. The elemental EDS results for C0, C1, C5, and C9 builds are shown in Table 1.8. Scans were performed in middle locations of each cross-section sample from the builds. Data for C0 and C5 reported Cu wt% that was not detected in the other builds. As previously mentioned, this type of elemental analysis can be unreliable due to limitations of the detector or sample preparation [25] and is therefore

considered to be relatively qualitative in the measurement comparison. Smaller elements are included with this data with the weight percent of zero to indicate that they were tested but no quantity was detected.

Table 1.2. Elemental analysis of test build cross-sections by EDS.

Element	C0 [wt%]	C1 [wt%]	C5 [wt%]	C9 [wt%]
Fe	68.3	65.4	68.1	65.1
Cr	17.2	18.6	17.6	18.4
Ni	9.8	12.1	9.7	12.2
Mo	1.9	2.2	2.2	2.5
Mn	1.9	1.0	1.6	1.0
Cu	0.4	0.0	0.4	0.0
Si	0.4	0.8	0.4	0.8
O	0.0	0.0	0.0	0.0
P	0.0	0.0	0.0	0.0
S	0.0	0.0	0.0	0.0
Nb	0.0	0.0	0.0	0.0

Using the data from Table 1.2, the Cr_{eq}/Ni_{eq} ratios of the test builds from C0, C1, C5, and C9 were calculated per Equations 1.1 and 1.2 and presented in Table 1.9. Carbon and nitrogen content is unreliable from EDS measurements so these values are estimated using the C and N content from the bulk powder chemical analysis from Table 1.1.

Table 1.9. Ferrite Number (FN) determined from EDS analysis of test builds from select cycles. Carbon and nitrogen content is estimated from powder samples from the same samples.

Cycle	Cr_{eq}	Ni_{eq}	Cr_{eq}/Ni_{eq}	FN
C0	19.2	12.5	1.5	4.0
C1	20.8	14.6	1.4	3.2
C5	19.8	12.4	1.6	7.0
C9	20.9	14.8	1.4	3.2

Based on these estimated FN values there is a drastic change in the solidification structure during the deposition process resulting in a high amount of ferrite content. This amount of ferrite is unlikely for 316L SS however [26] and attributed to limitations of the

EDS scanning as well as the estimation of the welding Cr_{eq}/Ni_{eq} equations applying to the DED process. The chromium weight percent should be between 16-18% but exceeds this amount for C1 and C9. Nickel weight percent is low for C0 and C5, the standard for the 316L SS alloy is between 10-14% [9]. Testing these builds with a ferritescope would properly measure the ferrite content.

1.4.2.3. Build Finish:

The test builds made with consistent parameters were evaluated for surface finish and dimensional accuracy. Table 1.10 shows the relevant parameters of the builds from each cycle. Power and speed of the laser are constant, while there were small variations, < 1 g/min, in the PFR for each cycle. The oxygen level for all deposits was below 5 ppm. Figure 1.29 shows the resulting test builds from C0, C1, C5, and C9.

Table 1.10. Dimensions and deposition parameters for test builds from C0-C9. All other deposition parameters were consistent with Table 1.

Cycle	RPM	PFR (g/min)	Oxygen (ppm)	Build Width (mm)	Build Depth (mm)	Build Height (mm)
C0	2.8	26.3	1.7	15.96	15.98	13.00
C1	2.9	26.4	3.0	15.99	16.01	12.88
C2	2.9	26.6	4.9	15.83	15.80	12.95
C3	2.9	26.7	4.2	16.03	15.96	12.71
C4	2.9	26.8	1.9	15.97	15.89	12.94
C5	2.8	26.2	0.5	15.98	15.80	12.78
C6	2.8	26.8	0.8	15.90	15.82	12.80
C7	2.8	26.7	0.5	15.89	15.85	12.58
C8	2.8	26.3	0.6	15.94	15.86	12.75
C9	2.9	26.5	0.6	15.98	15.88	12.84

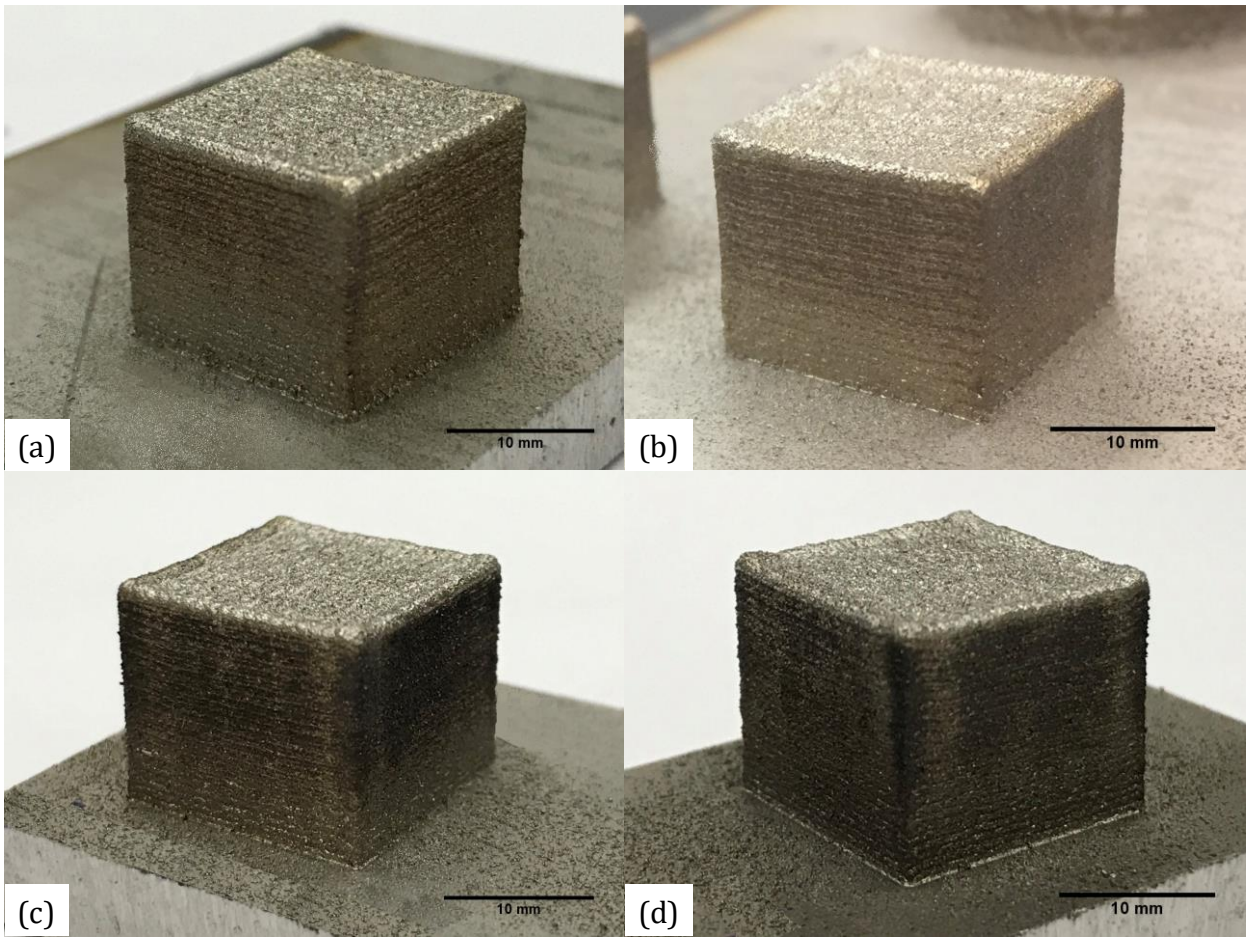

Figure 1.29. Test builds from (a) C0, (b) C1, (c) C5, (d) C9.

The surface finish appears to remain consistent from C0 through C9 showing the typical corrugated top and wall textures from the layered deposition. However, the builds from C5 and C9 are much darker on the surface than the builds from C0 and C1. The discoloration on any build with laser AM is the result of the thermal gradients from the solidification process, particularly the rapid quench solidification of the initial layers [11]. As the heat source of the melt pool moves further away from the substrate, the cooling rates decrease and the previous layers in the build remain at a high temperature longer, causing the color change on the surface in this thermally effected area. The amount of discoloration could depend on process parameters, the intrinsic properties of the material, and the geometry of the build [11]. This discoloration on builds of different geometry from the same cycle are shown in

Figure 1.30. All builds were deposited on substrates of the same size and thickness. Each build has a different discoloration offset from the surface of the substrate that correlates with the layer area of the build. Table 1.11 reports the layer area for each part shown in Figure 1.30, calculated as the build widths in the x and y directions, and the discoloration offset, measured as the height from the substrate to the start of the discoloration. The offset is shown to increase with increasing layer area as to be expected. A larger area allows the thermal gradients to disperse laterally in addition to vertically, thus maintaining the initially cooling rates longer into the build height [10], [11].

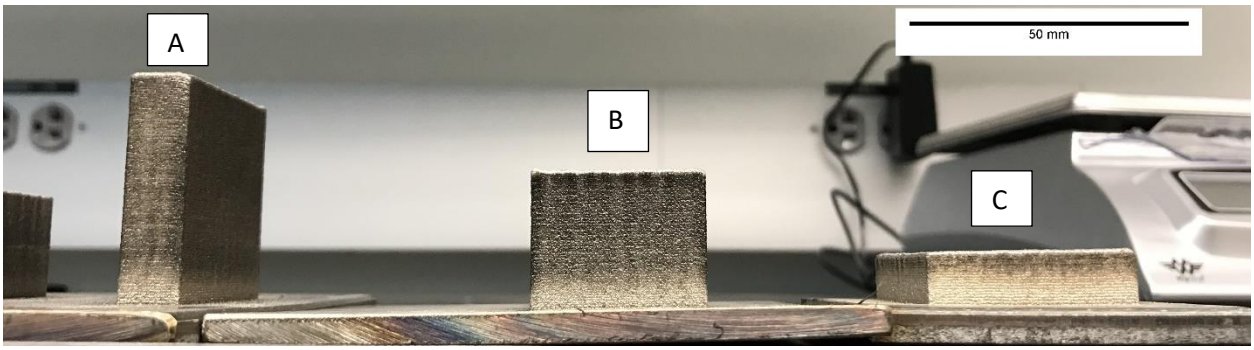

Figure 1.30. Builds of different geometry and volume from the same deposition cycle showing variations in surface discoloration.

Table 1.11 Table of build layer area and associated offset of the surface discoloration with respect to the substrate surface.

Part	Layer Area (mm^2)	Discoloration offset (mm)
A	387.1	3.9
B	929.0	4.9
C	1451.6	5.2

1.4.2.4. Density:

Archimedes' principle was used to determine the density of each build by testing the four cuboids three times and taking the average of the calculated densities from Equation 1.5. The results, shown in Table 1.12, show that all builds were > 99.70% dense compared to a wrought density of 7.95 g/cm^3 [38]. The full density of all builds indicates that there is no

effect on bulk density from the porosity seen in the particles or with the reuse of feedstock powder.

Table 1.12. Densities of test builds from C0, C1, C5, C9 resulting from Archimedes density tests.

Cycle	Density (%)
C0	99.97
C1	99.80
C5	99.70
C9	99.90

1.4.2.5. Microstructure:

1.4.2.5.1. Internal Defects:

The internal porosity and microstructure of the select test builds were evaluated by SEM. Figure 1.31 shows low magnification micrographs of each build examined, C0, C1, C5, and C9, having good build quality and supporting the > 99.7 % density calculations. However, there were some defects found in each sample as observed in the micrographs in Figure 1.32. Open pores and unmelted particles were found in each build. C0 was the only build that exhibited clear lack of fusion porosity, micrograph C0 (b) and (c), evident by the elongated openings occurring horizontally [39]. Micrographs C0 (a), C1 (a), C5 (a), and C9 (a) resemble the porosity observed in the powder particle cross-section samples from micrographs C1 (a) and (b), C5 (a), and C9 (a) in Figure 1.19 and therefore could be attributed to the powder properties rather than the deposition parameters. Micrographs C1 (b), C5 (b), and C9 (b) appear to be open pores likely formed from the trapped argon gas or keyhole porosity [40] [41]. Micrographs C0 (c), C1 (c), C5 (c), and C9 (c) highlight combinations of unmelted particles as well as some lack of fusion. The occurrence of this type of porosity could be attributed to the change in morphology and size of the particles through continued reuse. It

was also reported that slight changes in morphology of particles can drastically change the flow behavior and laser or melt pool interaction [35]. However, there was not a noticeable increase in these features with increased reuse of powder based on this analysis technique. To fully characterize the porosity, X-ray computed tomography (X-ray CT) could be utilized as a nondestructive technique [42]. The calculated densities also support the assumptions that most of the porosity seen in Figure 1.32 is the result of unmelted or partially melted particles and not excessive open voids.

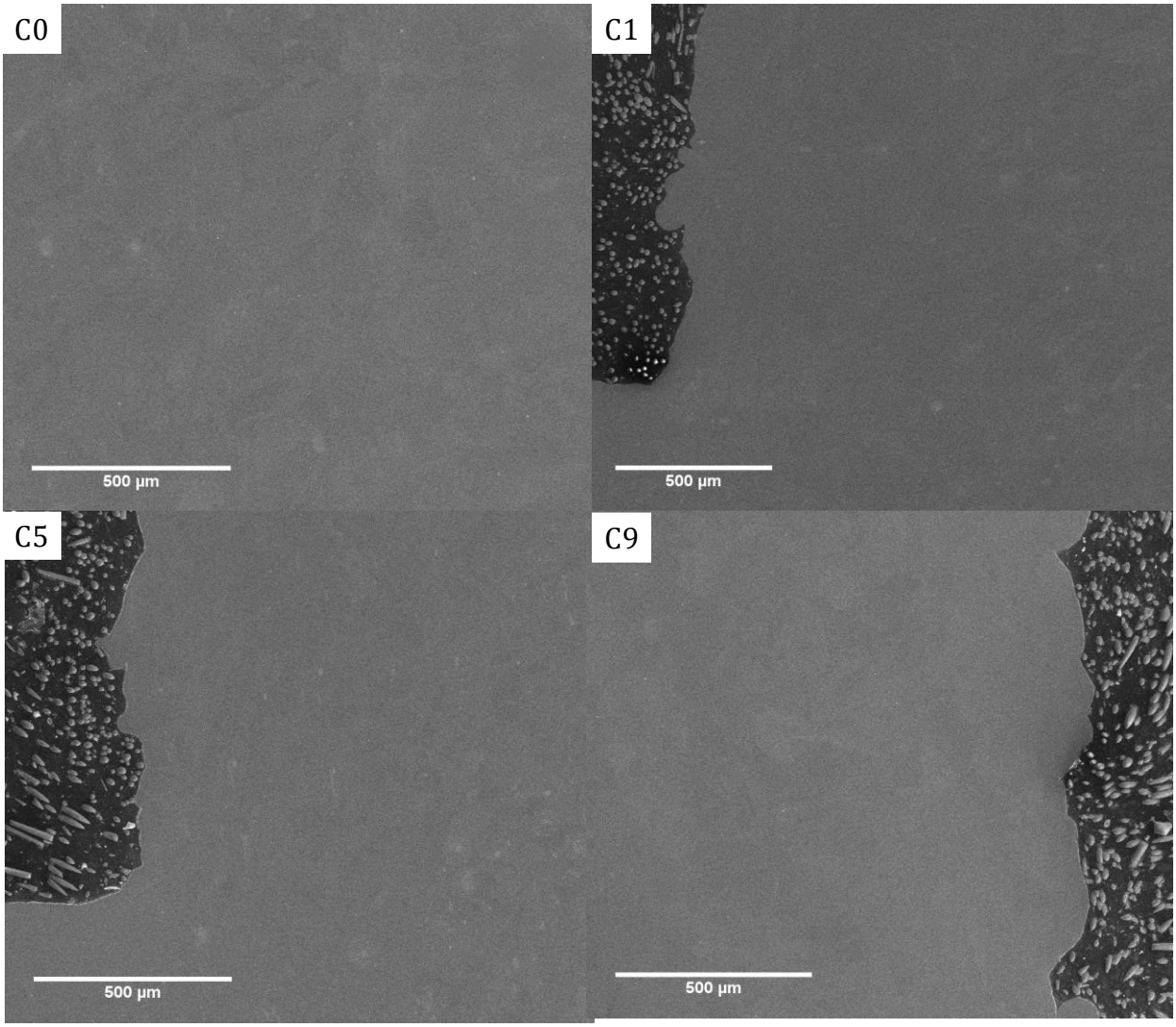

Figure 1.31. SEM micrographs of cross-sections of builds from C0, C1, C5, C9 showing fully dense microstructure.

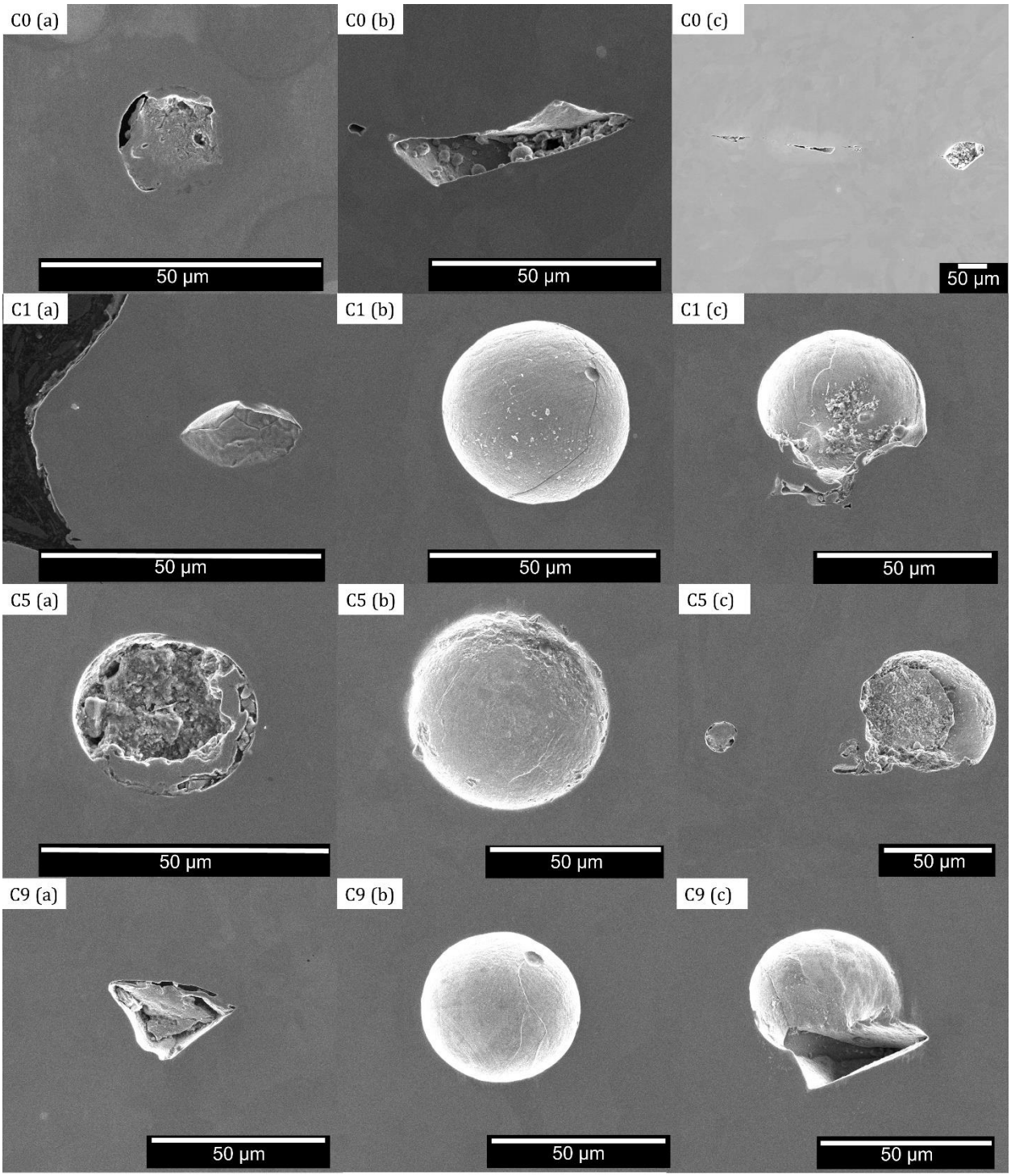

Figure 1.32. SEM micrographs of cross-sections from select test builds.

1.4.2.5.2. Weld Pool and Layer Characteristics:

Microstructure samples from the test builds were etched and characterized using the Olympus OM and ImageJ software. To compare the quality of the builds from cycle to cycle features of the weld pool and layer heights were measured. The shape of the weld pool was determined to quantify the track overlap between layers [43], [44]. The thickness of the dilution layer, which is the first layer deposited onto the substrate, was measured and compared to the thickness of the layers at the top of the builds to understand the amount of remelting that occurs with each laser pass.

The etchant used on the polished cross-sections highlights the boundaries of cellular structures within the microstructure of the builds. Due to the rastering heat source and rapid solidification of the DED process these cellular boundaries occur at the weld pools of the laser [45]. The cross-section samples were cut to be parallel to one edge of the cube and therefore the etched micrograph, seen in Figure 1.33, shows the layered weld pools, Layer B, alternating with perpendicular tracks, Layer A. The weld pool of each test build is measured in width and depth, the average of five measurements from each location, bottom and top of the build, are compared in Table 1.13. The layer dilution was also evaluated for each build as the average of layer thickness at the bottom and top of the build and is presented in Table 1.13 as well. The amount of remelting of the previous layer should be more than the layer height [1], [11], [46]. The thickness will change from substrate to the top of the build if the deposition time is long enough to reach the steady-state associated with the build parameters and location of the melt pool within the critical laser energy region [1]. The deposition conditions for all test builds evaluated here have a set layer height of 0.01” or 254 μm, which is less than all top layer thickness values for each build, indicating good deposition

parameters throughout the powder reuse cycles. Based on the results in Table 1.13, the deposition process was consistent for all builds at the bottom layers. The substrate dilution is within the error range for each cycle as is the weld pool dimension ratio of depth to width, D/W. The D/W ratio for the top portion of each build is also relatively unchanged. The layer thickness at the top of each build shows a different trend. With increased powder reuse, the top layer becomes thicker. Since the deposition conditions for each cycle were consistent, the increase of layer thickness at the top could be attributed to a change in the powder, particularly the oxygen content. The increase in oxygen content within the powder could affect the thermal properties of the particles during interactions with the melt pool. Particles with an oxidation layer can increase the absorption of the laser and increase the melt pool volume, thus causing the deposition tracks to become deeper compared to particles with lower oxygen content [31]. Ultimately, the oxidation layer and slag created on the particles from laser interactions can lead to increase in porosity [31], [47]. Since there is no increase in porosity seen in these builds it is assumed the oxygen levels have not exceeded the limits of these process parameters and the resulting build quality is not affected.

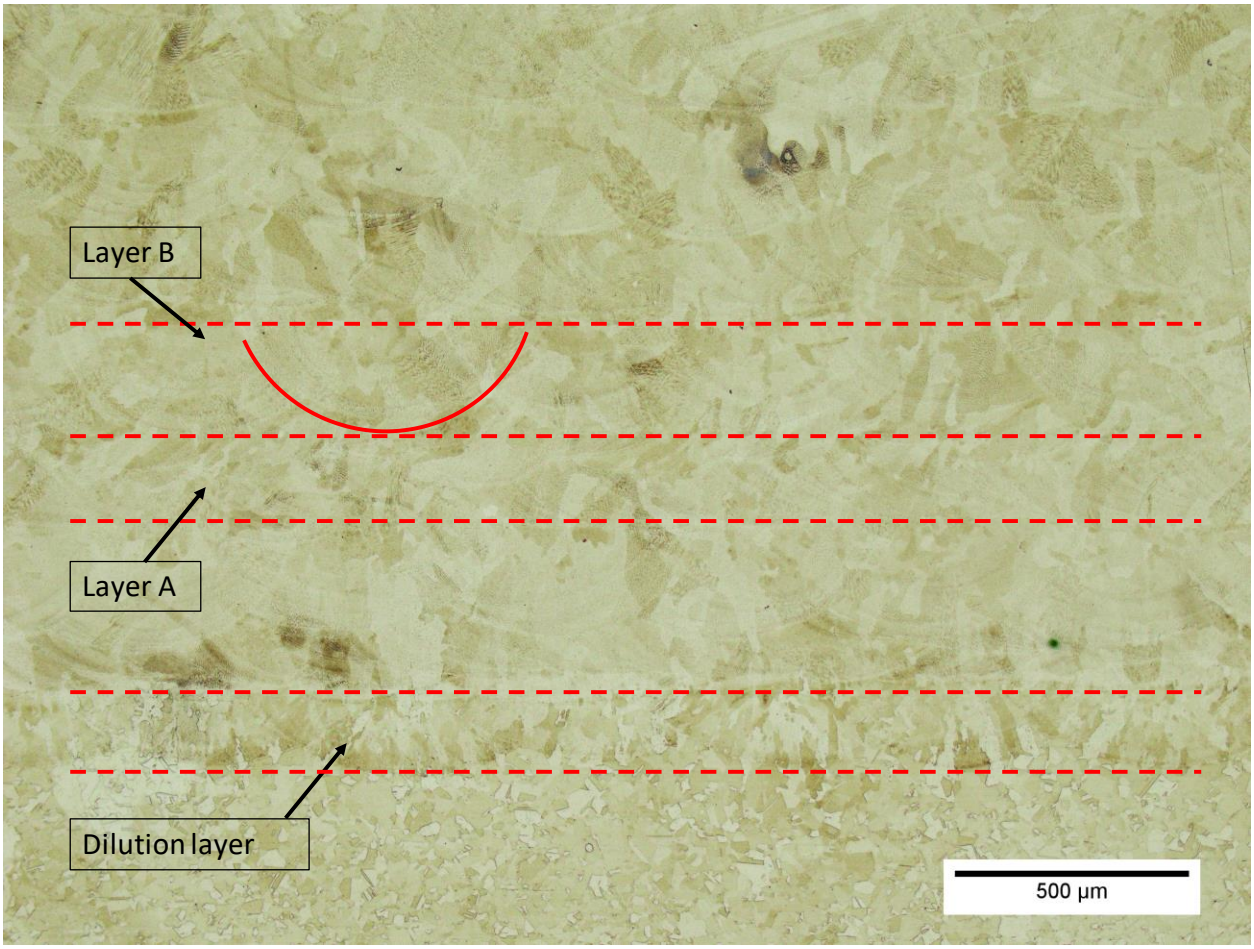

Figure 1.33. Etched OM micrograph of a cross-sectioned sample from C0 showing the dilution layer from the substrate/deposition interface followed by several layers of alternating hatch rotation

Table 1.13. Measured characteristics of weld pool D/W ratio, layer dilution with the substrate, and top layer thickness from C0, C1, C5, C9.

Cycle	Substrate Dilution (um)	Substrate D/W	Top Layer Thickness (um)	Top D/W
0	155 ± 13	0.33 ± 0.03	301 ± 27	0.37 ± 0.07
1	186 ± 14	0.31 ± 0.02	355 ± 30	0.38 ± 0.05
5	178 ± 14	0.36 ± 0.07	358 ± 17	0.33 ± 0.07
9	143 ± 15	0.32 ± 0.03	369 ± 19	0.42 ± 0.06

1.4.2.6. Compression:

The compression testing done on the cuboids from the selected test builds resulted in the average compression yield strengths shown in Table 1.14. While there is a difference of

approximately 50 MPa between C0 and C9 cycle builds, all builds exhibit high compressive yield strengths that are consistent with traditional AM depositions of 316L SS [45]. The general decrease from C0 to C9 could be attributed to the reuse of powder and the increase on oxygen content. Increased oxygen content in the feedstock powder can increase porosity [31] which would be detrimental to mechanical testing. Though large changes in porosity was not detected in the builds from the density measurements, it is possible that there is an increased number of unmelted particles within the center of the C9 build compared to C0 build which could lead to failure during compression testing but not have a large influence on density measurements.

Table 1.14. Compressive Yield Strength for test builds from C0, C1, C5, C9.

Cycle	Compressive Y.S. [MPa]
0	474.4 ± 6.1
1	444.3 ± 6.8
5	468.5 ± 10.7
9	425.7 ± 6.8

1.4.2.7. Microhardness:

The microhardness of each build from C0, C1, C5, C9 was tested with a microhardness indenter using the Vickers Hardness scale, the results of which are shown in Figure 1.34. The hardness values show the builds have highest hardness closer to the substrate with decreasing hardness toward the top layers of the builds. This is as expected due to the higher cooling rates in the initial layers of a deposition since they are closer to the substrate, which acts as a heatsink [11], producing finer microstructures at the base of the builds. The error bars in each cycle result in little deviation between cycles and thus there is no observable trend from the reuse of powder.

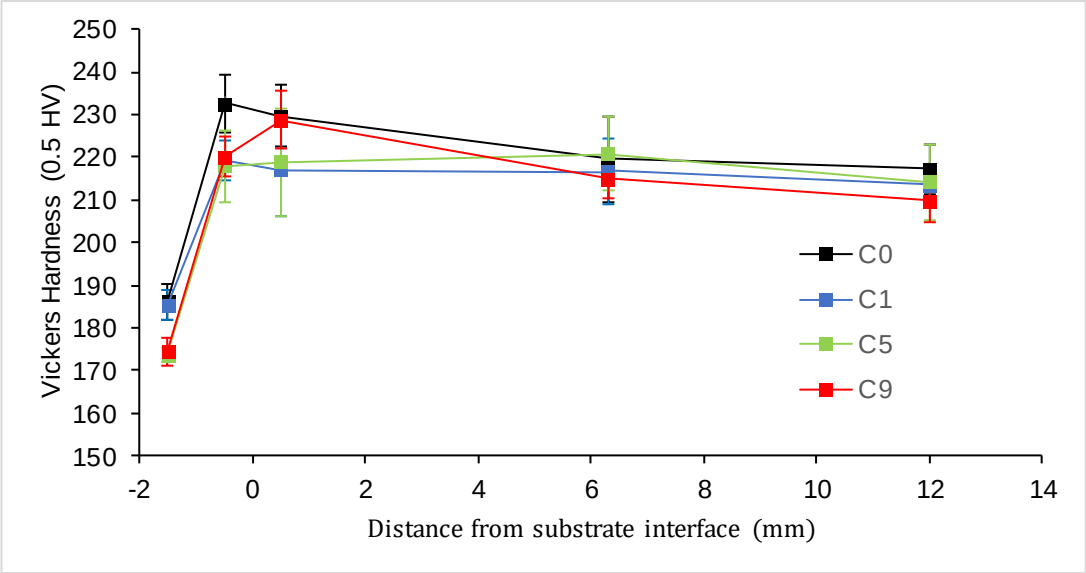

Figure 1.34. Hardness measurements of test build samples from substrate to the top of the build. The substrate is located at 0 mm. Indents were made at 500 gf for 10 seconds.

1.5. Conclusions:

- Powder properties do not change significantly with continued reuse in LENS® deposition, though there are some notable trends. The mean size becomes increasingly larger and the mean shape becomes increasingly irregular. There is a consistent increase in oxygen content with increased powder reuse, however no direct correlation with powder properties was observed.
- Flow behavior of the powder particles varies from cycle to cycle. This can be correlated to changes in particle properties for some cycle ranges however there is no consistent trend. To properly test and predict the flowability of powder within the LENS®, the apparatus should resemble the application and thus more investigation is necessary.
- On build properties, there are constant microstructural and physical properties throughout the reuse cycles. The increase in oxygen content of the particles may

have minimal effect on the build microstructures but the overall quality of the builds is not altered after ten cycles of powder use.

1.6. Suggestions for Future Work:

- To further explore the change in oxygen content of powder particles, humidity content could be evaluated by utilizing a thermal gravimetric analyzer. If the reused powder shows in increase in humidity, adding a baking step after the sieving process could help limit the amount of oxygen retained in the particles during the reuse process.
- To better understand the changes in solidification mechanisms of the builds from cycles of increased powder reuse, the FN should be tested with a ferritescope. An accurate understanding of the solidification phases could elucidate any dependence on the oxygen content of the powder.

CHAPTER TWO

2. Effect of hatch rotation angle on microstructure and mechanical properties of LENS® builds:

2.1. Background:

The process parameters of LENS® directed energy deposition (DED) greatly affect the quality of depositions. Changing input parameters can cause variation in solidification rates and the directionality of heat flow within the material by influencing the local energy of the melt pool and ultimately influencing the microstructural evolution [8], [11]. Varying these input parameters can also lead to the development of manufacturing defects, such as lack of fusion (LOF) [39], [48], keyhole porosity [48], [50], [51], [52], and inconsistent layer dilution [1]. These defects can affect many aspects of build quality, such as build surface finish, geometric accuracy [8], and mechanical performance [53]. Thus, it is important to carefully control input parameters for the given material to achieve the desired build quality and mechanical performance. This chapter details how hatch rotation angle influences build properties of 316L austenitic stainless steel.

The hatch rotation angle is the angle between scanning directions of subsequent layers of the deposition. The typical hatch rotation angle is 90° and is implemented to eliminate defects by filling voids of the previous layers. Figure 2.1 is a top down view of a build showing the scanning direction is offset by the hatch angle, θ, between layer n and n+1.

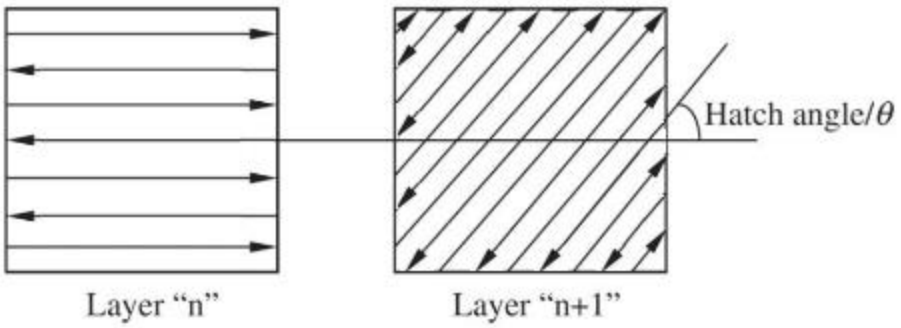

Figure 2.1. Top down view of two build layers with hatch rotation angle offset (adapted from [13]).

Ensz [12] investigated software control for LENS® and found that the build surface finish and geometrical tolerances are highly sensitive to the hatch pattern and stressed the importance of filling in voids between deposition layers while avoiding excessive overlap. It was suggested that the hatch rotation angle of 105° was superior in achieving fully dense parts. Guan [13] expanded this investigation by confirming the effects of the 105° rotation angle with mechanical testing of SLM 304 SS reporting higher tensile properties of ultimate tensile strength, yield strength, and elongation with the 105° hatch rotation angle than any other angle tested. Guan described the effect of an angle between scanning direction in terms of interval number of layers, Figure 2.2, which quantifies the number of layers required to return to the original layer's scanning direction based on the angle θ. A 105° hatch rotation angle gives an interval number of layers of 24. It has been hypothesized that a higher interval number of layers between identical scanning directions increases the randomness introduced into the microstructure by repeatedly altering the directionality of heat flow and limiting preferred grain growth [13], [50]. However, this hypothesis has yet to be verified by detailed microstructural characterization. In this chapter, 316L SS was used to deposit builds with varying hatch rotation angles of 0°, 90°, and 105° to allow the comparison of builds

manufactured with significantly different interval number of layers. Build quality was evaluated for each hatch rotation angle by visual inspection and dimensional accuracy. Electron backscattered diffraction (EBSD) characterization was performed to evaluate the influence of hatch rotation angle on microstructure development. Compression testing was also performed to corroborate the noted physical property effects from literature with the increase in randomness of subsequent scanning directions.

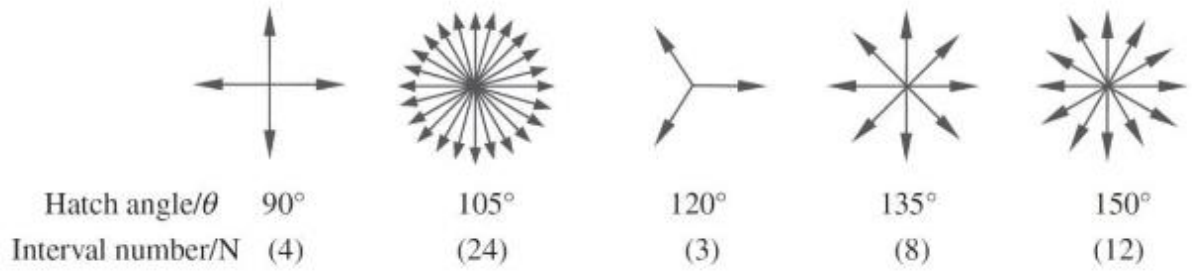

Figure 2.2. Hatch rotation angle and the associated interval number of layers [13].

2.2. Approach:

Builds with each hatch rotation angle were deposited and evaluated per the procedure shown in Figure 2.3. To obtain equivalent size test specimens for each processing condition for consistent analysis, the depositions were first assessed to ensure equal build volume and geometric accuracy. Then two samples were deposited from each set of parameters to evaluate density and mechanical properties. Compression test specimens were extracted from these two deposits in the vertical direction, parallel to build height, and the horizontal direction, normal to build height, to also evaluate the influence of build orientation on mechanical behavior. Mechanical properties were correlated with the microstructure and manufacturing defects of the builds by performing detailed characterization of grain orientation, grain size, and layer and weld pool characteristics.

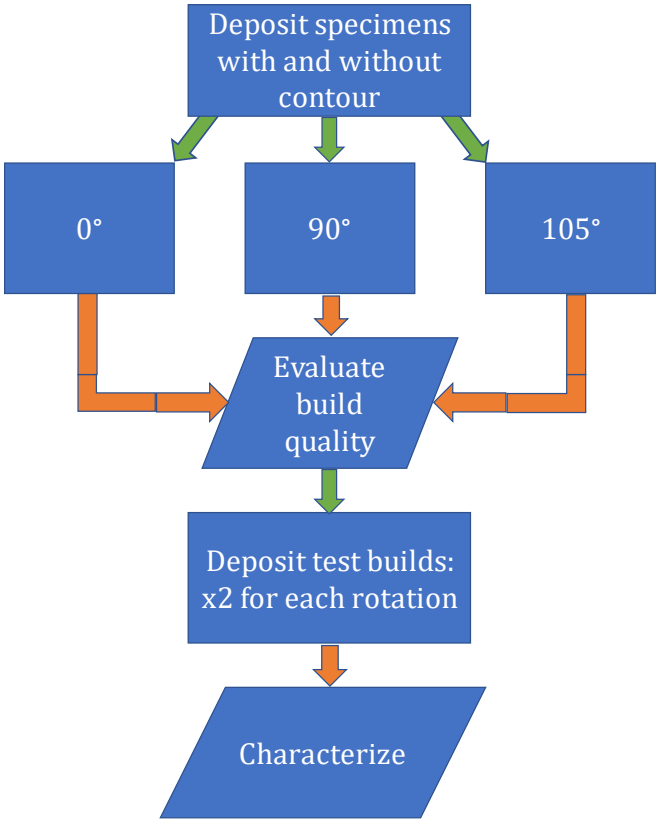

Figure 2.3. Flow diagram of hatch rotation angle depositions and characterization.

2.3. Methods:

2.3.1. Deposition parameters:

The feedstock used for depositing the hatch rotation angle test builds was 316L SS from C0 of the powder reuse project, see Chapter 1. Deposition parameters were selected through another parametric study. The builds for this hatch rotation angle investigation were not manufactured concurrently with builds from the powder reuse project; therefore, the PFR was determined separately. Two builds with a hatch rotation angle of 105° were deposited with different powder feeder settings of 2.7 RPM and 2.8 RPM. Each was cut with a band-saw to evaluate internal porosity. It was found that the build with 2.7 RPM had a slightly higher density, 99.3 % compared to 99.1% of the 2.8 RPM. The 2.7 RPM powder feeder setting gave a PFR of 25.4 g/min and this PFR was consistent for the rest of the depositions for this

project. Two builds were made for each hatch rotation angle. Aside from the hatch rotation angle, all other deposition parameters, Table 2.1, were consistent with the powder reuse project. The build dimensions for this investigation were expanded to a width x length x height of 0.62 in x 0.62 in x 0.52 in to provide more material for characterization specimens.

Table 2.1. Deposition parameters for hatch rotation project.

Power (W)	Laser Speed (in/min)	PFR (g/min)	Layer Thickness (in)	Hatch Spacing (in)	Hatch Pattern	Hatch Rotation (°)	WD (in)
295	40	25.4	0.01	0.016	Serpentine	0, 90, 105	0.28

2.3.2. Cutting:

Builds were sectioned into samples for mechanical testing and microstructural characterization using wire EDM. One test build for each hatch rotation angle was cut into four cuboids from the center of the builds as vertical cuboid samples, and cuboids from the other test build for each hatch rotation angle were cut with the longer side perpendicular to the build direction as horizontal cuboid samples. All cuboids were cut to have aspect ratios of 1.5 and dimensions of 3.8 mm x 3.8 mm x 5.7 mm, the longer side of the cubes being parallel to the test direction. The cutting scheme for the vertical and horizontal samples is shown in Figure 2.4 (a) and (b), respectively. In addition to the cuboids, two microstructural samples were cut from each build. One 2.5 mm thick cross-section cut from the side of the build containing the substrate to the top layer, and one 2.5 mm thick cross-section from the center of the build. The center microstructure samples were cut in the same orientation as the respective test cuboids. The cuboids were used for density and compression testing. Optical microscopy characterization of the side cross-section sample was performed for internal defect analysis and evaluation of weld pool and layer characteristics. EBSD

characterization of the center cross-section sample was performed to evaluate grain size, and grain morphology and texture.

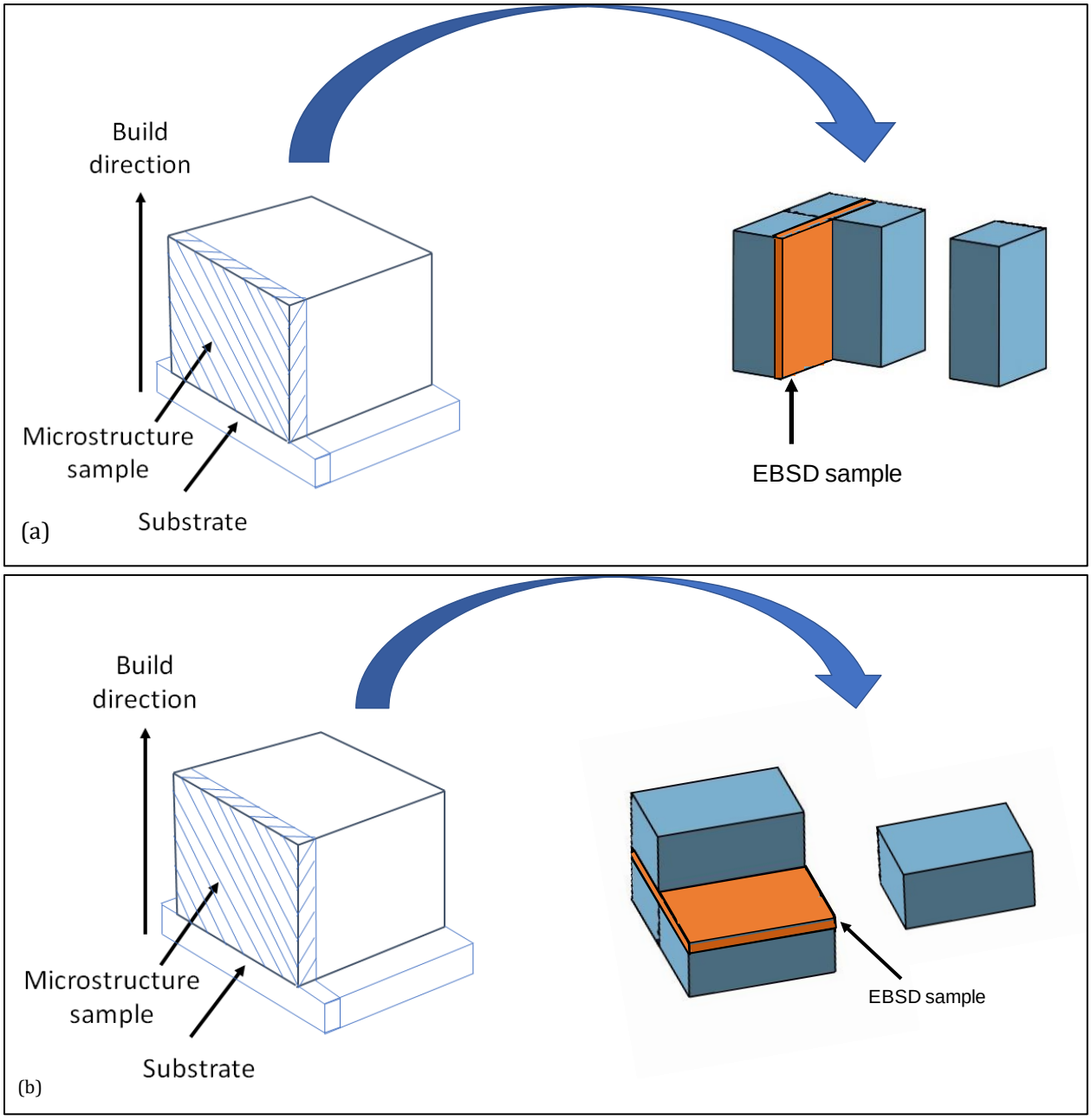

Figure 2.4. Schematic of test builds cut with EDM for (a) vertical and (b) horizontal microstructure analysis samples and density/compression analysis cuboids.

2.3.3. Density:

The Archimedes' density principle was applied to test the density of each build in the same manner as described in Chapter 1. The cuboids were polished to 1200 grit SiC grinding paper on all faces to remove surface roughness. A Mettler Toledo AG204 balance was used to perform the test with ethanol as the liquid medium to submerge the cuboids and measure their buoyancy. The weights of the specimens were measured in air and in the liquid and their density was calculated according to Equation 1.5. The four cuboids from each build were tested three times and the average was taken of all twenty-four test results to be the final density for each hatch rotation angle.

2.3.4. Microstructure:

Microstructure was evaluated with OM micrographs of etched cross-section samples. The edge cross-section samples were mounted in KonductoMet conductive filled phenolic mounting compound using a Buehler SimpliMet 1000 Automatic Mounting Press (Buehler, Lake Bluff, Ill.) and polished metallographically to 0.04 μm colloidal silica suspension. The polished surface was then etched with a mixture of 3:1 hydrochloric to nitric acids for 30 seconds. This etchant highlights cellular features of the weld pools and layer characteristics. The Olympus OM was used to image and characterize these features for comparison between builds.

The center cross-section samples were used for EBSD characterization in a Helios 660 dual beam SEM/FIB (FEI, USA) equipped with a Nordlys Nano EBSD detector (Oxford Instruments, UK). These samples were metallurgically polished to a 1 μm diamond finish. Electropolishing with a LectroPol-5 electropolisher (Struers, Denmark) using a 10 vol% perchloric acid solution (Struers A3) as the electrolyte was then performed to remove

residual surface deformation from mechanical polishing and produce a flat surface. A flat surface is required for accurate grain analysis. During EBSD, diffraction patterns are produced from electrons beam interactions with the atomic planes of the crystals near the sample surface. The diffraction patterns can be measured to provide details on crystallographic orientations of the sample. Misorientations between pixels of orientation maps can be compared and quantitatively measured to determine grain size. Crystallographic texture can also be represented in pole figures from the crystallographic orientations. The orientation measurements appear as points in the pole figure, and the clustering of these points with respect to different poles represents the occurrence of preferred orientations in the sample. The EBSD scan step size was set to 400 nm and achieved greater than 99.7% indexing.

2.3.5. Compression testing:

The cuboids used for density testing were subjected to compression tests with the Instron 8801 universal tester. Strain was measured using a laser interferometer. The cuboids were prepared by grinding all faces to a 1200 grit surface finish to achieve and maintain the appropriate aspect ratio of 1.5 for compression testing per ASTM E9-09 [24]. The cuboids were mounted between the anvils with WC platens as shown in Figure 1.4 and lubricated with moly-petrolatum lubricant. Each test was performed at a strain rate of 10^{-3} s^{-1} and stopped at 70% strain to maintain equivalent test procedures for all specimens. The test data provided by Bluehill software were postprocessed to account for the initial gauge length difference between the offset of the WC spacers and the actual height of each specimen. The corrected engineering strain was calculated by multiplying the recorded axial strain by the ratio of measured strain to sample height. The engineering stress was corrected by

multiplying the recorded stress by one minus the corrected engineering strain. The resulting engineering stress strain curve was used to calculate the 0.2% offset from the elastic deformation response to determine the corrected compressive yield strength. Three specimens for each test build were tested and the average yield strength is presented along with representative stress-strain curves from each hatch rotation angle and test orientation.

2.4. Results and Discussion:

2.4.1. Deposition parameters:

Initial depositions were designed with a contour, as is typically done with DED processes. The 90° and 105° builds were geometrically consistent with the target dimensions and desired surface finish. However, the 0° build did not meet these requirements. There was significant thermal warping on the front and back walls parallel to the scan direction. The three builds with a contour are shown in Figure 2.5. The side walls perpendicular to the scan direction did not experience the same warping yet they still did not reach the target dimensions.

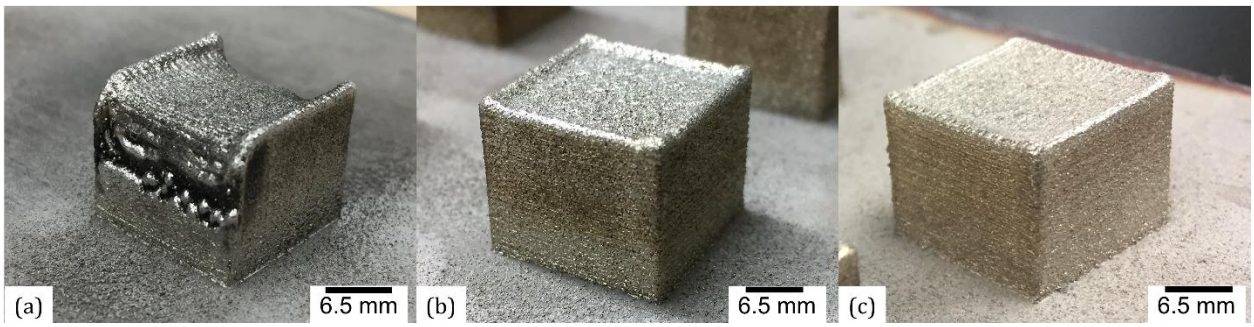

Figure 2.5. Surface finish of builds deposited with a contour for hatch rotations of (a) 0°, (b) 90°, and (c) 105°.

Overlapping of parallel deposition tracks, or of the hatch pattern for successive layers (i.e., when the hatch rotation angle is 0°), with the contour can create a situation where it is not possible to deposit layers of the designed thickness with a given set of processing

parameters [1]. This occurs when the surface height and melt pool location approaches the limits of the critical beam energy density region of the laser. Thermal cycling from repeated passing of the laser, even in areas far away from the laser, melt pool, and heat affected zone (HAZ), can contribute to the change in melt pool location with respect to the energy density region [10], [11]. The amount of cycling depends on the time between laser passes. For the 0° rotation builds the same scanning direction and start and end positions were repeated for each layer. When combined with the added scan of the contour, the sides parallel with the laser scan direction could have experienced excessive cycling and slower solidification rates causing the tracks to not retain the desired height [1], [11]. After a few layers, the build height on the parallel sides was too low and the scanning for the next layer began below the exposed region of the laser focal plane and the convergence of the powder flow and no deposition occurred. The point in the laser beam that interacts with the material did not have enough energy to form a melt pool and the laser only reheated the surface of the previous layers without adding additional material [1]. This reheating was observed during the deposition process for the first 2-3 passes of the hatch pattern on the parallel sides. Microstructural evidence of reheating can be seen in Figure 2.6 as the weld pools within the deposition layers of the 0° build slant downward towards the edge of the build due to lack of material capture. The 90° build in Figure 2.6 shows layers slanting upwards at the edge of the build with the additional material from the contour pass.

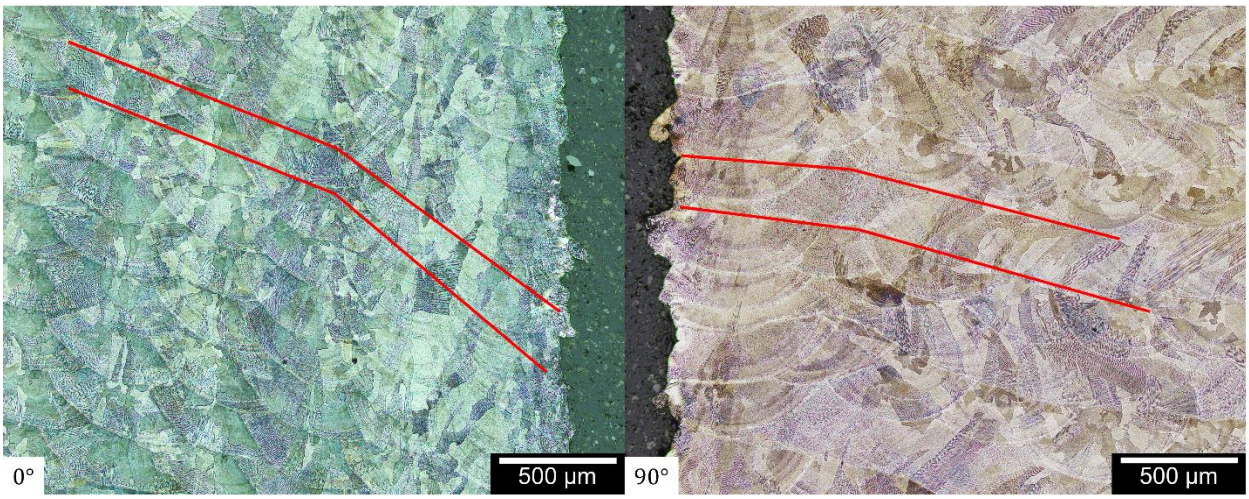

Figure 2.6. Micrographs of 0° and 90° build side cross-section showing slanting weld pools at edge of build parallel to scanning direction.

The thermal cycling seen by the perpendicular edges of the 0° builds have a different effect on the solidification process. This portion of the build is not effected by the HAZ in the same manner as the parallel sides because the time between laser passes is longer than for the parallel sides. The cooling rates for these sides could therefore have been faster than the parallel sides and they were able to achieve a higher build height [1]. However, the effects of the repeated laser scanning pattern still limit the amount of material that can be deposited and the heights do not match the other builds.

To achieve the necessary build volume for the 0° samples, depositions without the contour were explored and the resulting builds for each rotation angle are shown in Figure 2.7. The build with 0° hatch rotation angle improved while the other two builds were further from the target dimensions. The 90° and 105° appear to have experienced similar effects of thermal cycling as the 0° in Figure 2.5 (a). The gaps and uneven end points of the hatch pattern were not filled by the contour between layers resulting in lack of buildup of material and the laser focal plane seems to once again be out of the critical energy density region for deposition at the build edges. The sides were only reheated after a certain number of layers.

The 0° build was closer to the target dimensions with the elimination of the added pass of the contour on the sides parallel with scanning direction. Without the reheating of this contour pass, the solidification rates were maintained and the layer height never fell below the critical deposition region from Figure 2. To confirm the effect of thermal cycling on the relationship between the contour and hatch rotation angle, further investigation can be done with thermal imaging of the builds. The addition of longer dwell times between the hatch pattern and contour pass, or build geometries with larger layer area, could be employed to understand this effect.

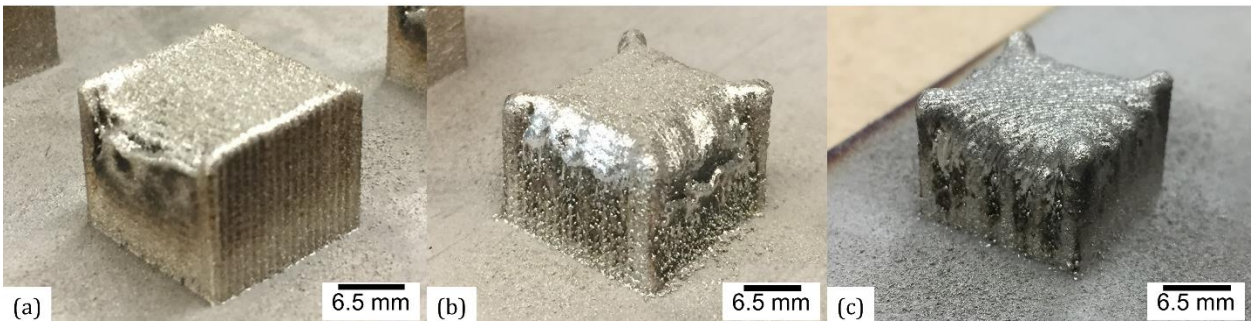

Figure 2.7. Surface finish of builds deposited without a contour for hatch rotations of (a) 0°, (b) 90°, and (c) 105°.

Given the effects of the deposition parameters on the build volume, the chosen samples to move forward in this project were the 0° without a contour and the 90° and 105° with a contour. The resulting build dimensions from each parameter set and the target build dimensions from the original CAD drawing are summarized in Table 2.2. The builds used for further characterization are highlighted in red.

Table 2.2. Dimensions of hatch rotation angle builds deposited with and without a contour before each layer.

Build	With Contour			Without Contour		
	Width (mm)	Length (mm)	Height (mm)	Width (mm)	Length (mm)	Height (mm)
0°	16.56	16.51	11.61	15.77	16.28	12.52
90°	16.48	16.56	13.31	15.95	15.98	12.27
150°	16.51	16.59	13.34	16.23	16.26	11.58
Target	15.75	15.75	13.21	15.75	15.75	13.21

2.4.2. Density:

The results of the Archimedes' principle density testing are shown in Table 2.3. The 90° and 105° cuboids were measured to be greater than 99% dense while the 0° cuboids were greater than 98% dense. It is known that alternating the scanning direction will fill the voids between layers so differences in density are expected due to the hatch rotations angles.

Table 2.3. Average relative density for builds with varying hatch rotation angle compared with wrought density of 7.95 g/cm^3 [38].

Build (°)	Density (%)
0	98.5 ± 0.1
90	99.5 ± 0.03
105	99.2 ± 0.2

The microstructure was examined for build defects and porosity. Optical micrographs in Figure 2.8 show porosity found in samples from each hatch rotation angle. The largest pores were found in the 0° and 105° and were approximately 50 μm in diameter. Smaller pores were observed in the 90° sample and were approximately 13 μm in diameter. These spherical pores were found at the bottom or between two weld pools in each sample. This is an indication of the entrapment of carrier gas during deposition or residual porosity from the gas atomization process of the powder feedstock [40]. The as-received (AR) powder particles, used for these depositions and analyzed in Chapter 1, show porosity of approximately 10 μm in diameter. This powder porosity could be affecting the build porosity,

particularly for the 90° build. In addition, the process parameters of the 0° and 105° builds could be more conducive to trapping of carrier gas.

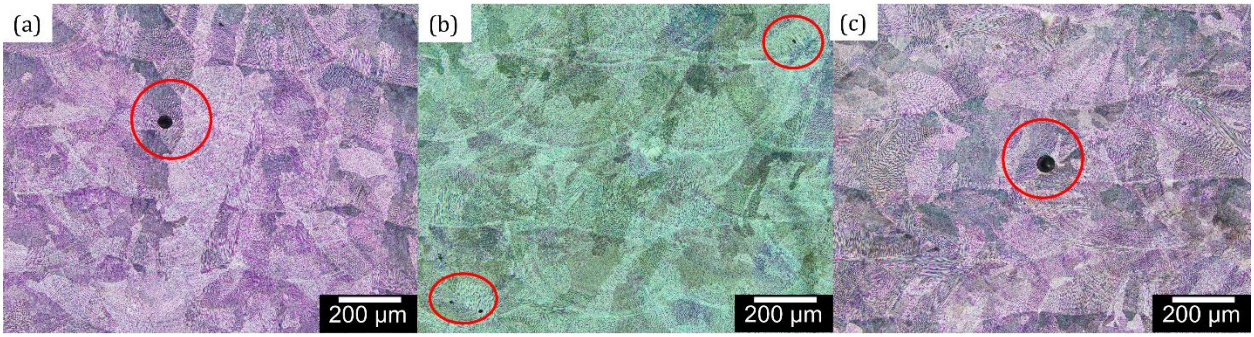

Figure 2.8. Optical micrographs showing porosity observed in builds of (a) 0°, (b) 90°, and (c) 105° hatch rotation angles.

Lack of fusion (LOF) porosity was found with an unmelted particle between two layers in the 105° build, the largest of which was 63 µm long and is shown in Figure 2.9. This type of porosity was not seen in the other side cross-section samples, however that does not exclude the possible presence of LOF porosity elsewhere within those builds. Based on the density measurements it is concluded that there was minimal occurrence of such porosity in all builds.

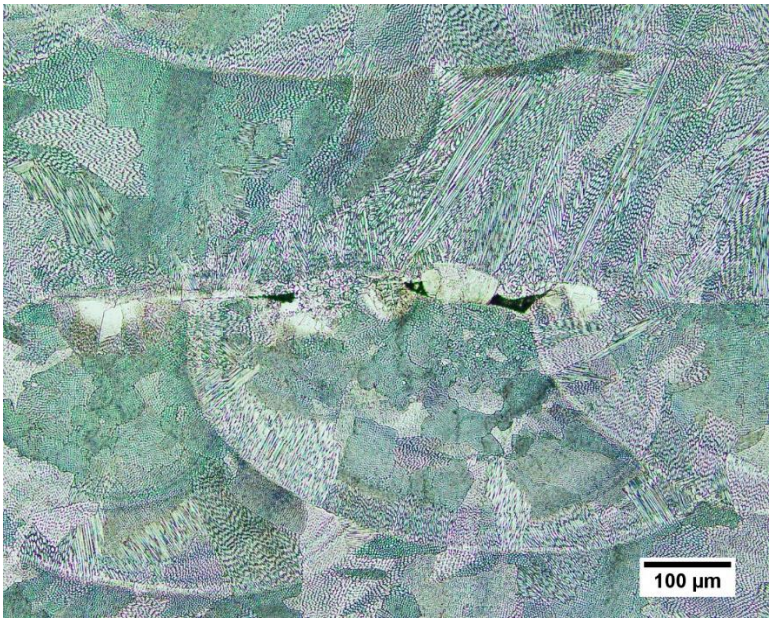

Figure 2.9. Lack of fusion porosity found in sample from 105° build.

2.4.3. Microstructure

To characterize the microstructure the etched side cross-section samples from each build were evaluated from low magnification OM micrographs with a polarizing light filter providing contrast. Since these samples were cut parallel with the edge of the builds there is a clear designation of the scanning directions. The 90° hatch side cross-section sample in Figure 2.10 shows the typical layered structure found in most DED builds of stainless steel [8], with alternating scanning directions between subsequent layers. The figure highlights the scalloped geometry of the weld pools in a single layer where the scanning direction was normal to the sample face. The scanning direction of the next layer was parallel to the sample face such that the view is of a length-wise cross-section of a single track. This pattern is repeated from the substrate to the top of the build.

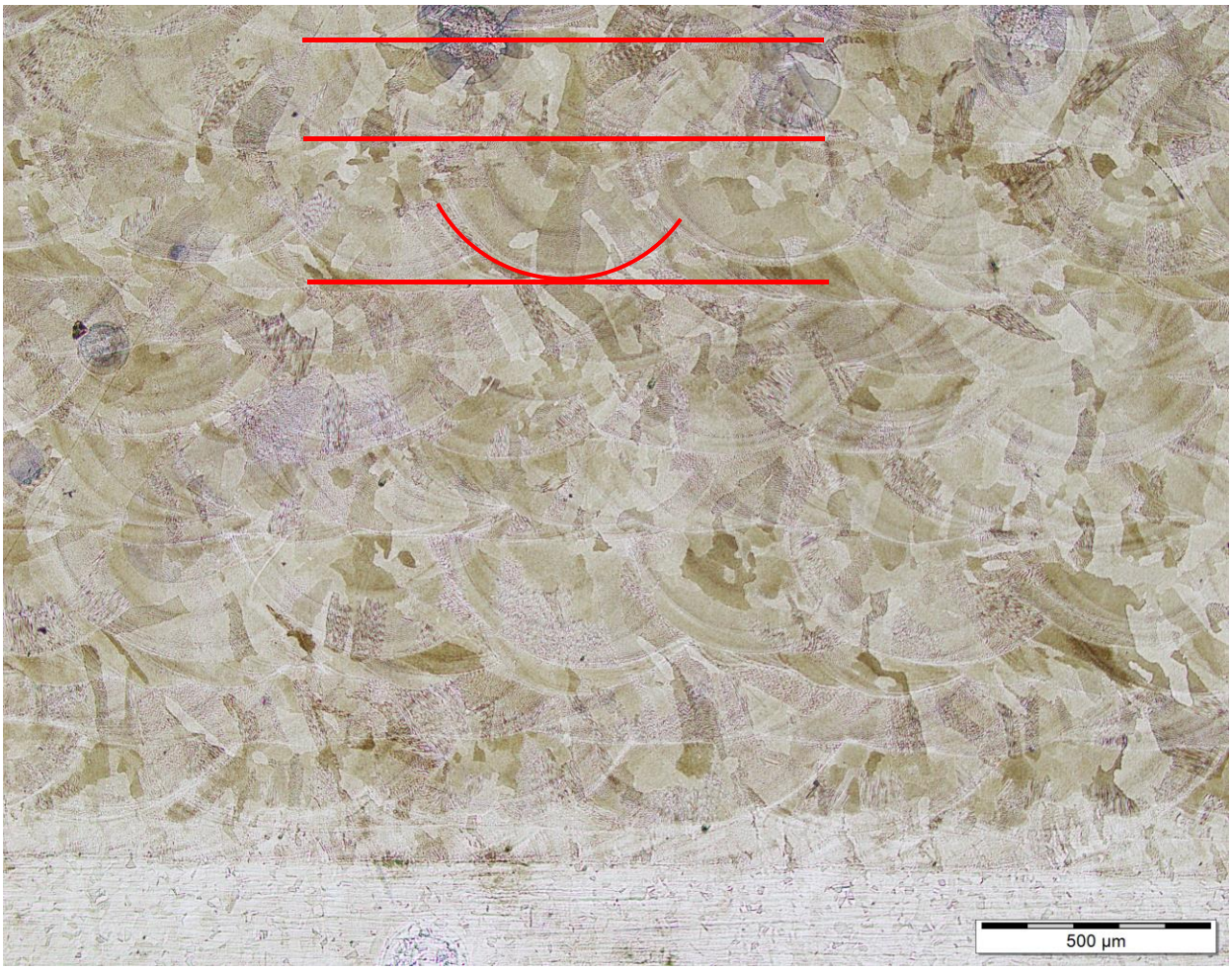

Figure 2.10. Optical micrograph of etched test build with 90° hatch rotation angle. The red lines outline the layers with alternating scanning direction. A weld pool fan geometry in the layer with the scanning direction that is orthogonal to the sample surface is outlined in red as well.

In the 0° hatch rotation angle micrograph, Figure 2.11, the scalloped geometry of the weld pool is distinctive because the scanning direction was orthogonal to the sample face. The weld pools from each layer aligned vertically due to the lack of rotation between layers. Also shown in this figure and the high magnification micrograph in the inlet is the elongated grains that exhibit an epitaxial growth as they span through several layers. This is quite unique for LENS® deposited SS microstructures, however long epitaxial growth was observed with SLM 316L SS with excessive laser power [55]. Epitaxial growth is also seen in the microstructures of titanium alloys [50] with the SLM process. The alternating layers of

the 90° side cross-section sample impedes epitaxial grain growth to no more than two or three layers as seen in Figure 2.10. In the 0° sample grains are shown to grow through as many as six layers. Since each new pass of the laser is in the same direction, the solidification direction is unchanged and epitaxial grain growth is less inhibited.

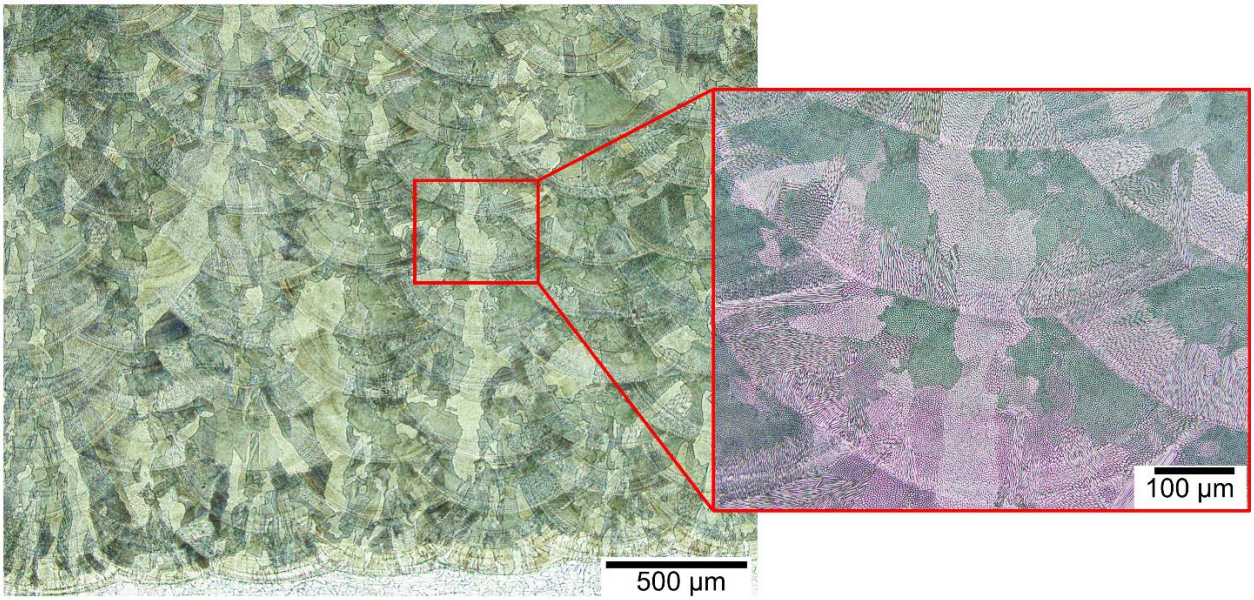

Figure 2.11. Optical micrograph of etched test build with 0° hatch rotation.

The microstructure of the 105° side cross-section sample shows less repetition than the previous two samples. From Figure 2.12 the horizontal layering is still distinguishable however the weld pools appear more elongated in this view. The sample face was cut parallel to the edge of the build as with the previous two samples, however the 105° rotation results in scanning directions that will only be orthogonal to the sample face every twelve layers. This degree of randomness limits the epitaxial grain growth across layer boundaries as seen in the 90° sample. Thus, the epitaxial growth across multiple-layers is more prevalent in the parallel-hatched sample (0°) than the cross-hatched samples (90° and 105°).

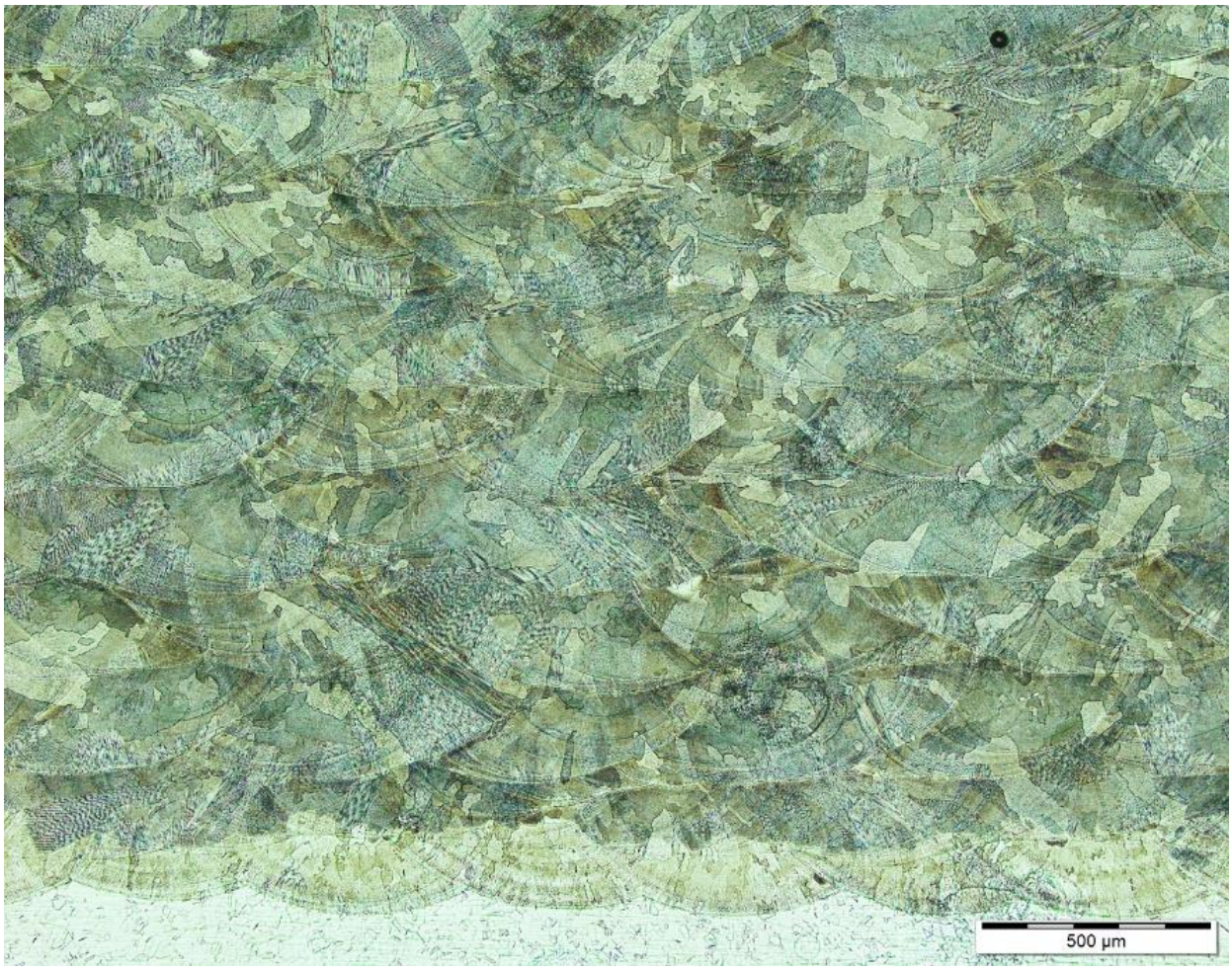

Figure 2.12. Optical micrograph of etched test build with 105° hatch rotation angle.

2.4.4. Grain size and orientation:

EBSD analysis was performed on the vertical center cross-section samples to quantitatively assess differences in grain size and orientation between the hatch rotation angles. The vertical center cross-section samples show the grain features through multiple layers as opposed to the horizontal center cross-section samples which represent grains of one layer. The grain size analysis results are presented in Table 2.4 as the average grain size in terms of length and breadth with 95% confidence interval (CI). The grains in the 0° rotation were the longest with an average length of 72 µm compared to the 50 µm for the other hatch rotation angles. The average grain breadth however does not vary with hatch

rotation angle. This supports the microstructures seen in Figure 2.10 - 2.12 and shows that the hatch rotation angle affects the grain morphology, however there seems to be little difference between the cross-hatches of 90° and 105°.

Table 2.4. Grain size comparison of length and breadth between vertical EBSD samples from each hatch rotation angle deposits. Calculations represent a confidence index of ± 95%.

Hatch angle [°]	Grain length [µm]	Grain breadth [µm]
0	72 ± 10	24 ± 3
90	49 ± 4	23 ± 2
105	50 ± 4	21 ± 2

The EBSD scans also provided insight into preferred grain orientations, particularly the maps obtained in the x-direction, Figure 2.13. The 0° center cross-section sample was cut orthogonal to the side cross-section sample according to Figure 2 (a) causing the sample face to be parallel to the laser scanning direction as opposed to perpendicular as was seen in the etched micrograph of Figure 2.11. Still, grain elongation across multiple layers, as observed in Figure 2.11, is apparent in Figure 2.13 (a). Similar grain elongation across multiple layers does not appear in the maps of the 90° or 105° samples in Figure 2.13 (b) and (c), respectively.

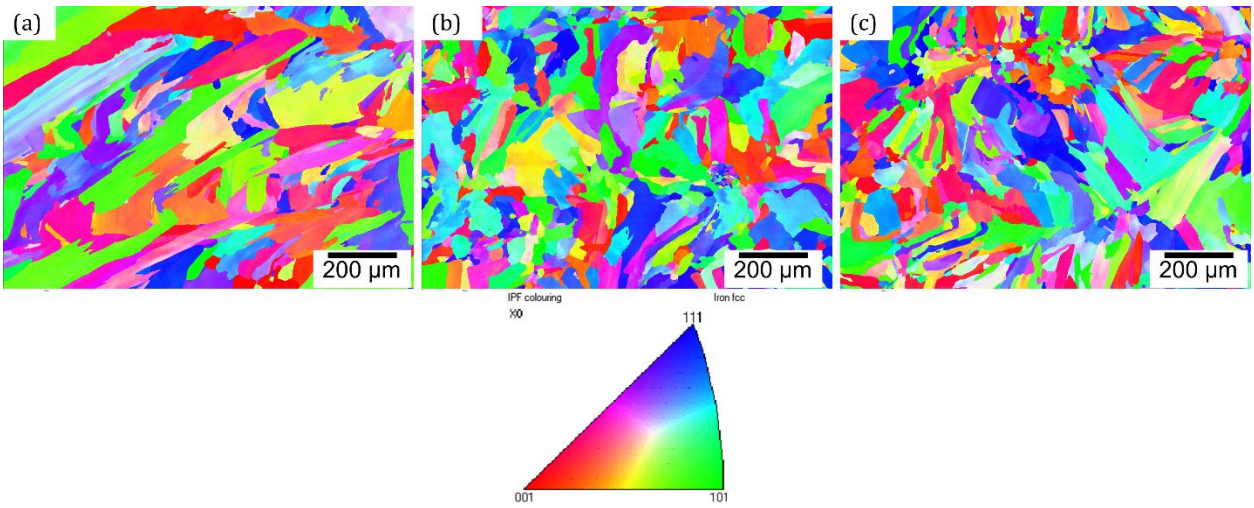

Figure 2.13. Comparison of EBSD grain orientation data from x-direction scans in (a) 0°, (b) 90°, (c) 105° vertical samples.

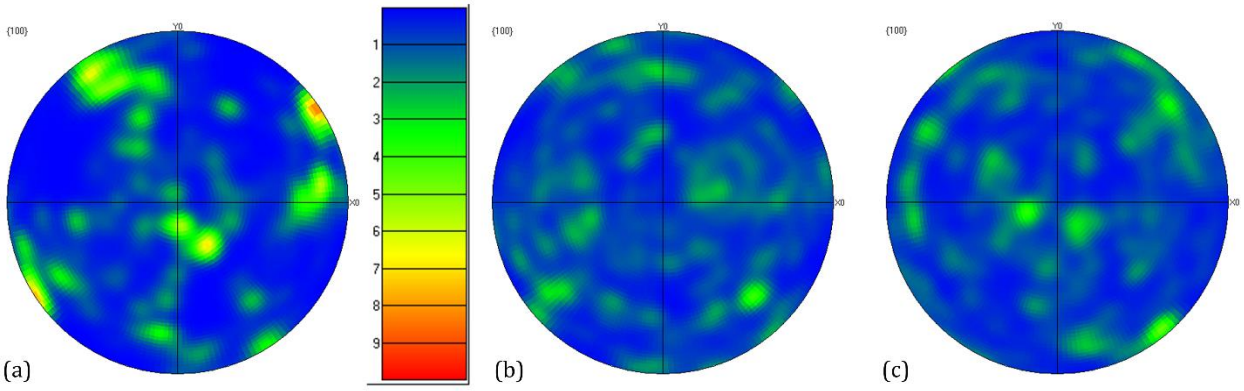

Figure 2.14. Pole figures of <001> direction for (a) 0°, (b) 90°, and (c) 105° hatch rotation angles.

Contoured pole figures from the same EBSD scans are shown in Figure 2.14 and reveal a strong <001> fiber texture direction for the 0° hatch rotation angle build that was not observed in the other builds. Epitaxial solidification of materials with cubic crystal structures, such as the FCC austenite phase of the DED 316L SS, favors crystal growth along the easy growth <001> directions occurring parallel to the direction of maximum heat flow [56]. The grain elongation and strong texture shown for the 0° rotation sample both occur at approximately the same angle of 30° from the scanning direction for this view, Figure 2.15. This angle is a result of the maximum directional heat flow from the melt pool with respect

to the laser source and solidification growth [8] [55]. By applying a cross-hatch scan strategy of either 90° or 105°, the preferred orientation is diminished.

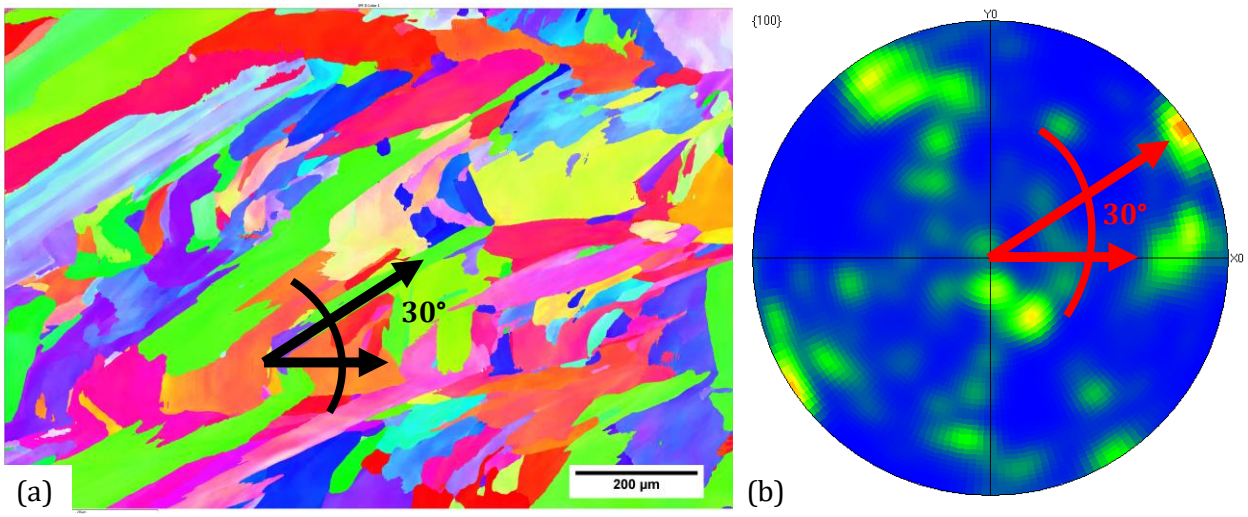

(a) (b)

Figure 2.15. Comparison of 0° (a) EBSD x-direction scan and (b) <001> pole figure texture occurring at the same angle of 30° from the scanning direction.

2.4.5. Compression testing:

Compression tests were performed on the vertical and horizontal cuboids cut from each rotation angle, the resulting stress-strain diagrams, see Figure 2.16, show representative curves for the three cuboids tested for each sample. The compression yield strengths are consistent with those reported for LENS® deposited 316L SS tested in tension [8], [57]. In the horizontal samples shown in Figure 2.16 (a), the stress strain curve for the 90° and 105° samples are quite similar, while the 0° sample does not reach the same stress values with increasing strain. The 0° hatch rotation angle specimens also have the lowest yield strength. In the vertical samples, shown in Figure 2.16 (b), the stress-strain response for the 0° samples more closely resembles that of the other hatch rotation angle samples yet the yield strength is still lower than the 90° and 105° rotation samples. The yield strength (Y.S.) of the cross-hatch samples for each direction tested is approximately 10% larger than the

respective Y.S. of the parallel-hatch samples. Thus, the cross-hatch scanning strategy improves the overall strength of the LENS® DED 316L SS builds.

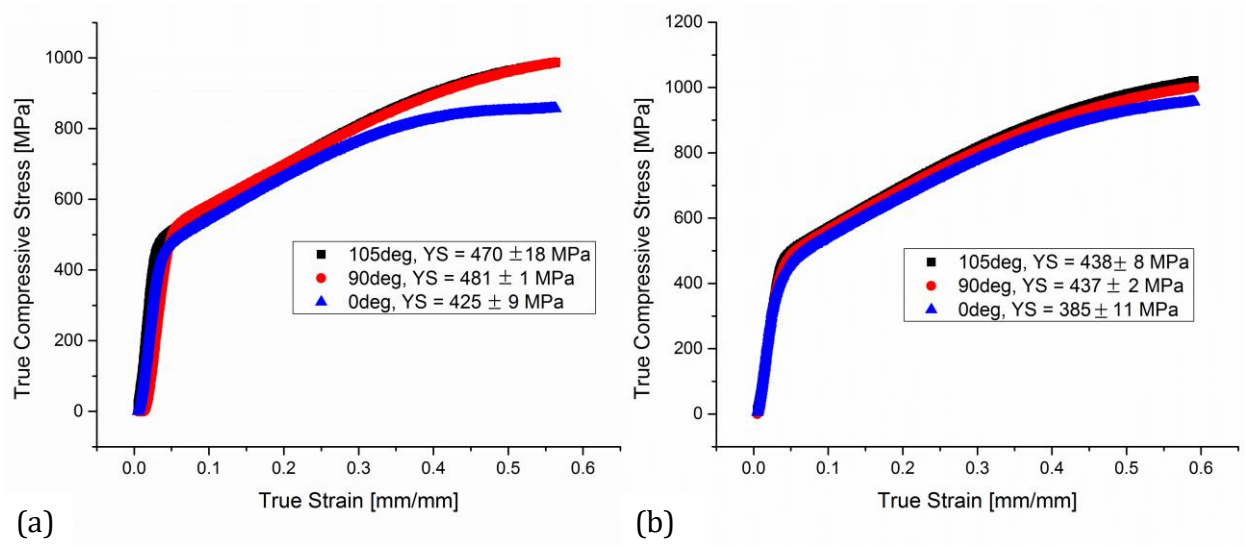

Figure 2.16. Compression stress-strain curves for (a) horizontal and (b) vertical cuboid samples from each hatch rotation build.

To characterize the anisotropy, the percent difference in directional yield strength was calculated for each build condition as the change in horizontal and vertical compression responses and is shown as a percent yield strength (Y.S.) anisotropy in Table 2.5. The 105° hatch rotation angle build shows the smallest percent Y.S. anisotropy, although only by approximately 2% compared with the other samples. Regardless of the angle between scanning directions and the interval number of layers, the compression response was comparable for all samples tested.

Table 2.5. Yield strength anisotropy for each hatch rotation angle, calculated as the percent change in compressive response between horizontal and vertical samples.

Hatch Rotation Angle [°]	Y.S. Anisotropy [%]
0	9
90	9
105	7

2.5. Conclusions:

- The hatch rotation angle was found to influence the build quality by altering the local deposition conditions, which led to geometrical inaccuracies.
- The hatch rotation angle affects microstructural development by promoting or inhibiting epitaxial grain growth during solidification.
- Applying a cross-hatch, the 90° or 105° angle for this investigation, during DED 316L SS improves the build density and compressive yield strength, but has negligible effect on yield strength isotropy compared to parallel-hatching.

2.6. Future work:

- To further explore the thermal warping that occurred during deposition of the parallel-hatch builds with a contour and the cross-hatch builds without a contour, in situ thermal imaging could provide information on cooling rates associated with the critical energy density region of the laser beam. The relationship can be tested by implementing a pause between contour and hatch pattern deposition. The layer geometry could also be expanded which would effectively create the same scenario by increasing the local dwell time.
- The cross-sections of compressed cuboid samples could be imaged to further analyze the effect of epitaxial growth on the generation of shear bands and possibly indicate any correlation with the noted texture and hatch rotation angle.

CHAPTER THREE

3. LENS® Issues, Operation, and Procedures:

3.1. Background:

The LENS® system requires proper operation and preventative maintenance to maintain productivity and good working conditions without unexpected down time. The Optomec manual has a significant amount of information on the system and should be utilized when starting to work with the LENS®. However, after over 900 hours of operation and troubleshooting time, there are some procedures and techniques that I have learned from experience and prepared as additions to the existing manual. Aside from input parameters, the nozzle alignment, power output, amount of feedstock powder in the hopper and condition of the substrate all contribute to the build quality and could affect final build properties. During the course of the projects discussed in Chapter 1 and Chapter 2, 250 lbs of powder were used to manufacture over 200 parts. From these depositions, several LENS® phenomena were observed. Examples of these along with the procedures for consistent depositions and general maintenance are discussed in this chapter.

3.2. Procedures for Consistent Depositions:

3.2.1. Powder Feed Nozzles:

3.2.1.1. Alignment:

The four nozzles that surround the laser are located at 90˚ from each other and angled at approximately 25˚ towards the laser. The nozzles and laser shroud are shown in Figure 3.1. This convergence angle is set by the deposition head that the nozzles are threaded into, however the alignment with the laser is adjustable. After any modifications or replacements of the nozzles the alignment procedure should be followed to confirm the laser beam is in

the center of the powder dispersion. If the nozzle and lasers are misaligned the powder will not be evenly injected into the melt pool and build defects can occur, such as the slanted corner shown in Figure 3.2.

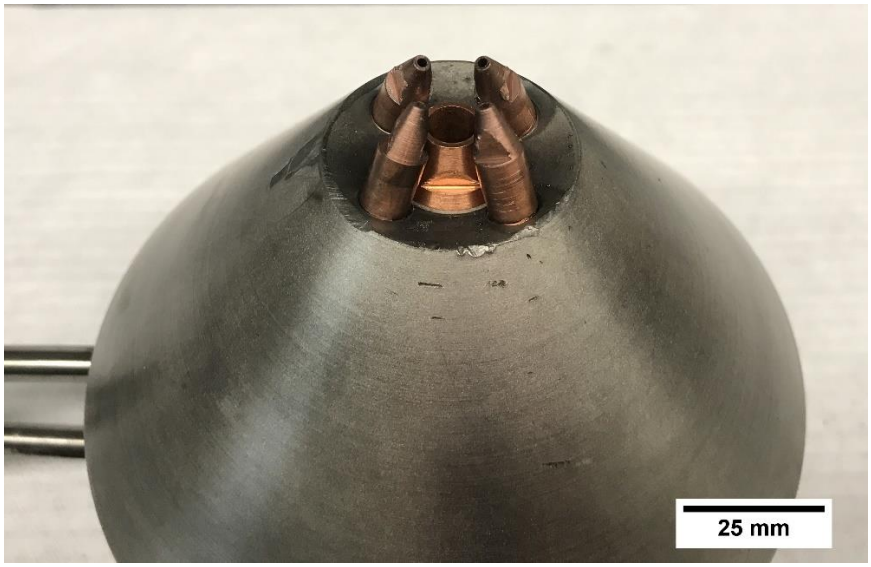

Figure 3.1. Deposition head disassembled from LENS® showing laser shroud surrounded by powder feed nozzles.

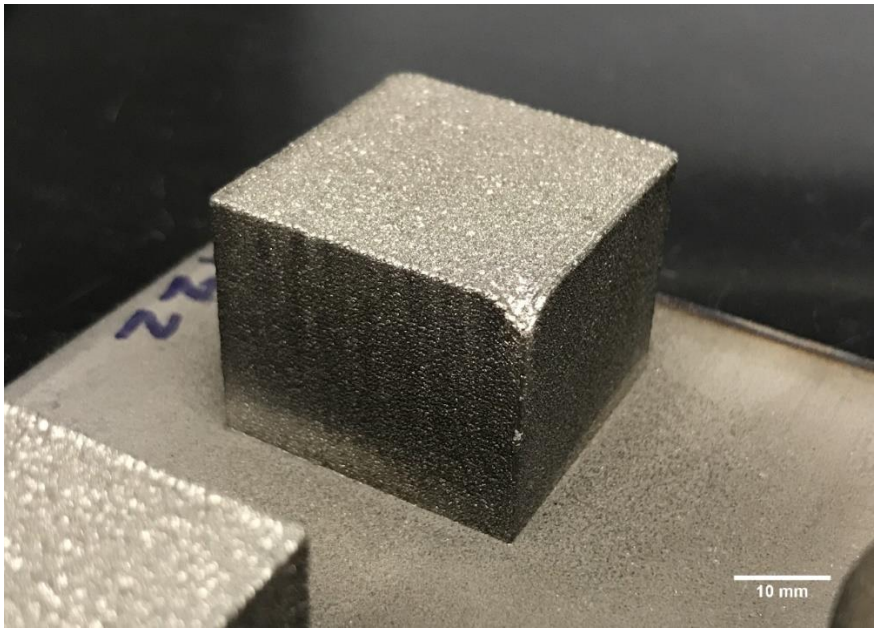

Figure 3.2. Build showing defect of slanted corner as the result of misaligned nozzles with the laser beam.

To align the nozzles, obtain a substrate or piece of scrap metal to be the alignment test piece and cover a portion of the surface with a black Sharpie as shown in Figure 3.3. Place the test piece flat on the stage and lower the deposition head so that the nozzles are just above the test piece, approximately 0.1 in, without touching them to the test piece. Ensure that all four nozzles are over the marked portion of the test piece. Set the RPM to 3.0 for sufficient powder flow and turn on the powder feeder for 30 s. The force of the powder through the nozzles will wear away the Sharpe in the dispersion pattern. After ~30 s of powder flow, turn the laser on at 150 W for approximately 5 s so there is a mark left by the laser on the test piece. Turn the laser and powder feeder off. Gently remove the test piece from below the nozzles and examine the markings. As shown in Figure 3.3, the four powder dispersion circles should form a square pattern with the small bead or mark left from the laser directly in the middle. If the laser mark is not in the middle, adjust the alignment knobs on the deposition head and repeat the procedure. In addition to the laser mark being in the middle of the nozzle pattern, the circles left by the powder dispersion should be equivalent. If one or more circles are not the same shape or density then nozzles should be replaced. In order for the powder to be injected evenly into the melt pool, the nozzles need to be aligned and the dispersion pattern should be equal.

Figure 3.3. Alignment test piece coated with black Sharpie and the resulting powder dispersion pattern with aligned laser mark.

3.2.1.2. Unclogging:

Prior to each deposition, the nozzles should be cleared of left over powder or melt pool splatter. The deposition parameters often result in splatter or sparks of melted particles ejecting from the melt pool like a fountain. This can be seen in Figure 3.4. The splatter can land on the part, the substrate, or if it has enough energy it could be ejected upwards toward the nozzles where it can stick. It has been observed that the amount of splatter and subsequent powder sticking to the nozzles depends also on the geometry of the build. If enough splatter is being ejected continually throughout the build there is the tendency for it to build up into metal droplets on the nozzles. As the droplets grow from added material and increased proximity to the laser, they can interfere with the laser beam, drop off the nozzles and land on the build. It is imperative to the build quality that these buildups are removed from the nozzles before they get so big that they interfere with the deposition process. This is commonly done with metal tweezers by simply knocking the droplets off the nozzles and

onto the stage away from the build. Several builds throughout the deposition process for the powder reuse project described in Chapter 1 were unable to be saved from the metal droplets landing and sticking on the surface of the build. Once they land, the droplets are often unable to be removed and the deposition process continues over them. If this happens early enough in the build, the subsequent layers will absorb the droplet and eventually it will not be seen. This is another example of the effect of the critical energy region of the laser.

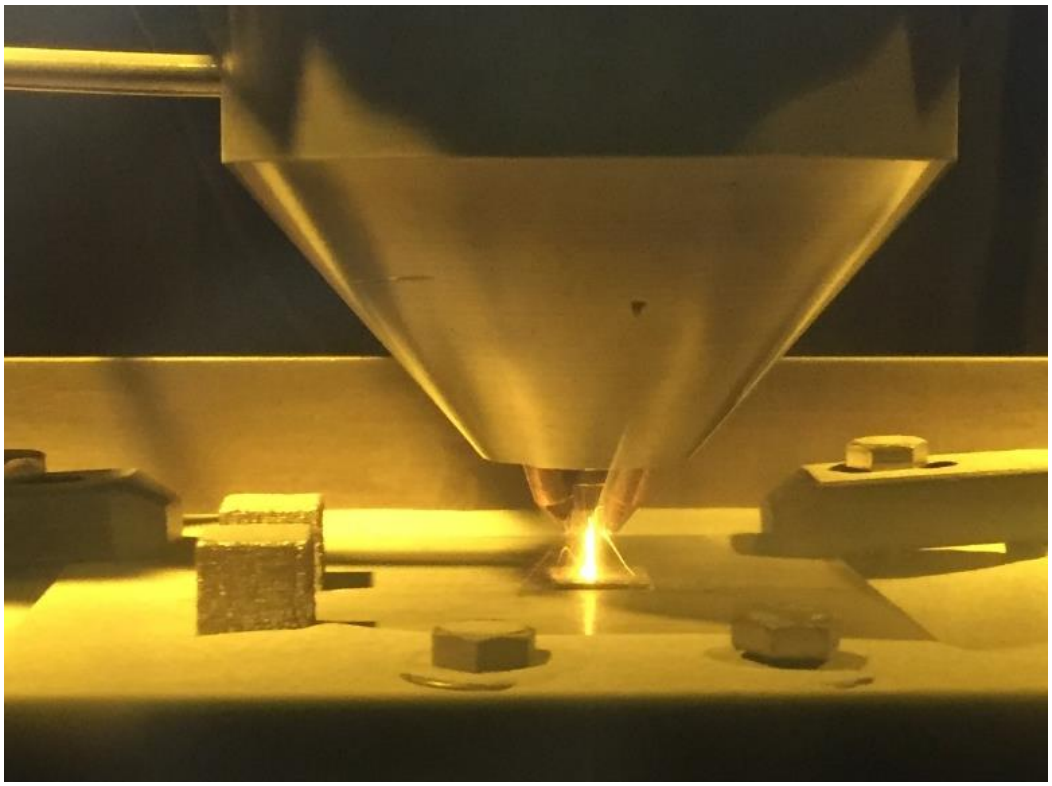

Figure 3.4. Melt pool splatter during deposition.

After the deposition, the nozzles cool and any remaining material from the powder stream or melt pool splatter could impede powder flow of the next deposition. To ensure the nozzles are clear, a thumb tac is inserted into each nozzle to remove any obstruction. Great care should be taken when performing this procedure so the gloves are not punctured and the nozzles are not damaged. It has been confirmed that even with all other deposition procedures equivalent, if the nozzles are not cleared prior to a build the PFR will vary. For

instance, a setting of 3.5 RPM produced a PFR of 22.1 g/min without clearing nozzles before deposition. After the nozzles were cleared, 3.5 RPM produced a 26.0 g/min PFR.

3.2.2. Powder Feed Rate Calibration:

The powder feed rates associated with RPM settings of the hoppers can varying depending on material used and conditions of the feed lines. Before starting deposits with new powder or after changing the feed lines, the PFR should be measured at various RPM settings and put into a calibration plot for the current conditions of the LENS® system.

Measuring the PFR is a four-step process:

Step 1: Fill the hopper with a known amount of powder and then evacuate the powder from the bottom port without collecting any extra powder that does not flow freely out of the hopper.

Step 2: Weigh the collected powder and return it to the hopper as the new initial mount of input powder to be delivered to the melt pool.

Step 3: After re-pressurizing the hopper, run the powder feeder at the set RPM to be tested for 10 min or a complete test deposition. Make sure to record the exact duration of time the powder feeder is on.

Step 4: Collect the remaining powder from the bottom port of the hopper, again only collecting the freely flowing powder. Weigh this amount and subtract it from the input amount. The difference in mass divided by the run time of the powder feeder is the PFR in g/min.

To maintain consistency the powder collection sequence from the hopper must be the same every time. Repeat this procedure for a range of RPMs. The plot in Figure 3.5 is the PFR

calibration used for the powder reuse and hatch rotation studies described in Chapter 1 and Chapter 2.

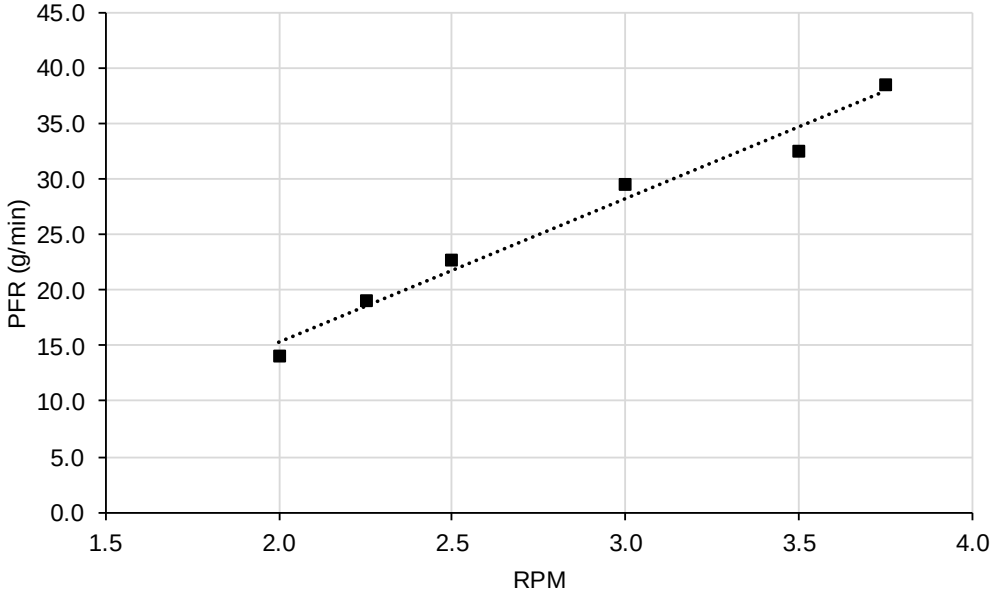

Figure 3.5. Calibration plot of PFR vs RPM for 316L SS.

3.2.2.1. Amount of Powder Feedstock in Hopper:

To maintain a consistent deposition for the same parts, it is important to keep all parameters the same including the PFR. There were several factors discussed previously that are known to affect the flow of powder through the LENS® system, even when the same RPM setting is used. In addition to the nozzles being cleared and the feed rate being properly calibrated, the amount of initial powder in the hopper can cause variations with the PFR. The hopper delivery system is dominated by the shape of the hopper, the flow of argon carrier gas, and the turning of the rotary mechanism that pushes the powder from the bottom of the hopper through the feed lines. The bottom of the hopper is shaped like a funnel which can cause a bottle-neck in the powder flow. How the powder flows through this portion of the hopper is determined by the powder shape and size, discussed in Chapter 1, as well as the weight of the powder on top of itself. The data in Table 3.1 show the effects of different initial

powder amounts on a repeated deposition of the same geometry and build parameters. This shows the PFR is increased with a larger amount of initial powder within the hopper.

Table 3.1. Deposition data on effect of initial powder on identical depositions PFRs.

Part	Starting powder (g)	RPM	PFR (g/min)
14	1193	3.1	25.9
15	2490	3.1	29.7

3.2.2.2. Optimizing PFR

A common lesson throughout the projects of this thesis is that optimizing LENS® deposition parameters for a particular material is crucial to build quality. The variation of one parameter can have a drastic effect on the build properties. During the powder reuse project, two builds of with target dimensions of 30.5 mm x 30.5 mm x 25.4 mm were manufactured, build #117 with 3.0 RPM, Figure 3.6 (a), and build #118 with 3.5 RPM, Figure 3.6 (b). All other parameters were kept consistent. The resulting parameters of build height and calculated PFR are shown in Table 3.2. During the deposition of build #117, it was noticeable at the build height of 6.3 mm that the working distance from the build surface to the powder feed nozzles was increasing. In addition, there was a large plume from the melt pool, and indication of vaporization of the melt pool and creation of black powder. The deposition of build #118 produced a smaller and less frequent plume from the melt pool, however there was more splatter that resulted in buildup on the nozzles. From these depositions, it can be concluded that with all other parameters identical, a low PFR can result in the melt pool and deposition plane falling below the critical beam energy regime and result in excessive smoke from the melt pool and low build height. A high PFR results in deposition conditions that produce excessive splatter from the melt pool and collection on the nozzles.

Table 3.2. Build parameters resulting from varying RPM.

Part	RPM	PFR (g/min)	Build Height (mm)
117	3	23.6	21.8
118	3.5	34.3	26.1

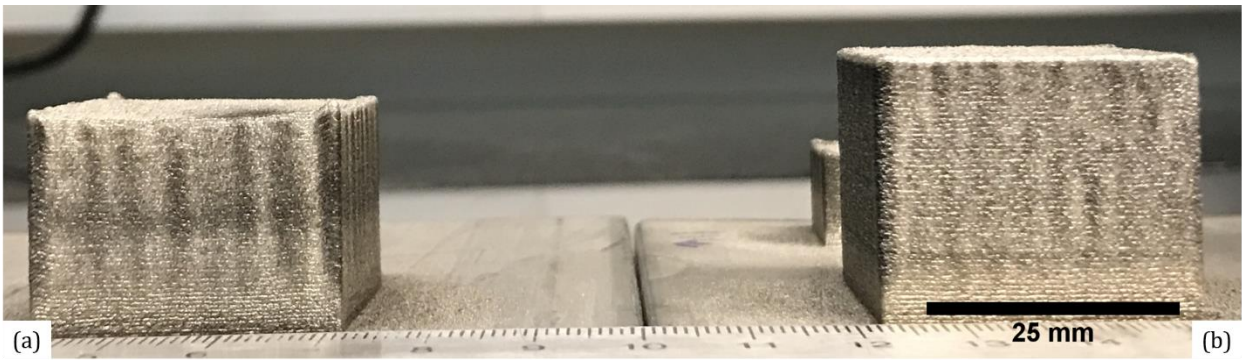

Figure 3.6. Two builds deposited at different RPMs with all other parameters identical. Build #117 (a) resulted in a height lower than the target dimension while the height of build #118 (b) was higher than the target dimension.

3.2.2.3. Effect of Build Dimensions on PFR

Another trend observed throughout the deposition of parts for the powder reuse project was the effect of build geometry on PFR. The deposition of build #117 discussed in the previous section was performed with the same parameters as build #61, shown in Table 3.3. Both depositions were cubes with varying dimensions. The noticeable change in PFR indicates that as the deposition time increases, the average powder feed rate decreases. To better understand the evolution of the PFR, each step in the powder delivery, process discussed in Chapter 1, needs to be investigated further. The change in powder flow over time could have varying effects on the build process of large deposits and result in unexpected microstructural properties.

Table 3.3. Build parameters resulting from varying deposition geometry.

Part	Cycle	Target Dimensions (mm x mm x mm)	RPM	PFR (g/min)
61	3	15.7 x 15.7 x 12.7	3.0	27.8
117	3	30.5 x 30.5 x 25.4	3.0	23.6

3.2.3. Power Calibration:

Power calibration should be performed prior to the start of a new deposition sequence and after any change or cleaning of the focal lens or lens cover. The power puck laser sensor measures power by sampling a 20 s exposure of the laser power and converts it to watts to be read from a dial. Determine the range of power settings to be tested, the lowest power should be tested first followed by the next in sequential order. Set the laser power output to the power to be tested. Move the deposition head to a z height of 5 inches. Hold the puck just above the stage, with the top face perpendicular with the laser, as shown in Figure 3.7. With the puck positioned below the laser, turn the laser on to absorb the power for 20 seconds. After 20 seconds turn the laser off and immediately read the output from the dial. Record the dial number in watts as the output for the set power on the workstation. Allow the puck to cool to < 10 W prior to testing the next power setting, this could take up to an hour depending on the power setting.

Figure 3.8 is the power calibration used for the powder reuse and hatch rotation studies. The plot shows the power measurements prior to changing the lens cover, 'Measured 10/2017', and the power measurements after changing the lens cover, 'Measured 3/2017'. It should be noted if the argon flow is turned on while testing the power. Figure 3.8 also shows the power tested after the lens cover change but with the argon on, 'Measured with Ar 4/2017'. The 'Displayed' data is the power output on the power supply module for each power setting.

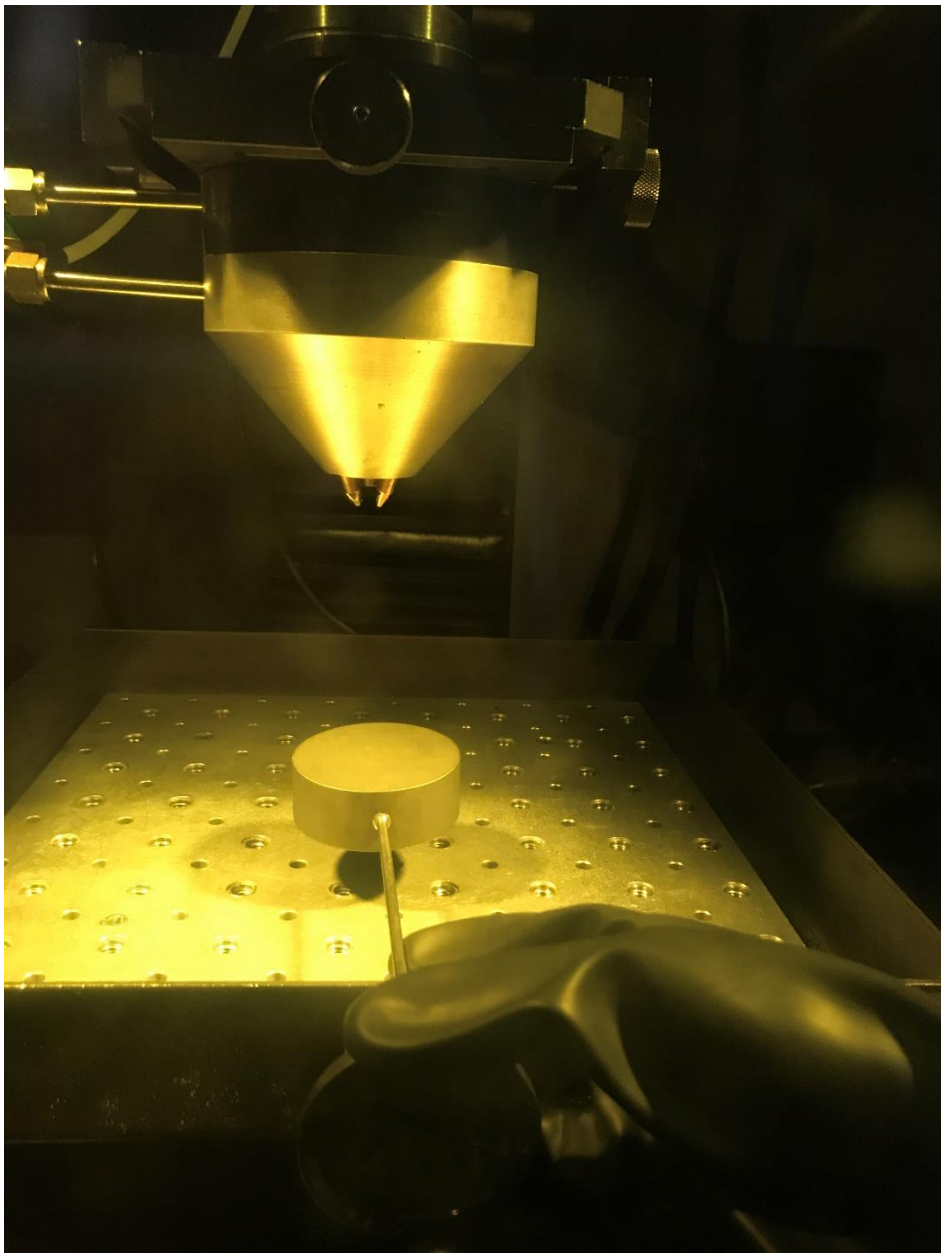

Figure 3.7. Orientation of the power puck laser sensor for calibrating output power.

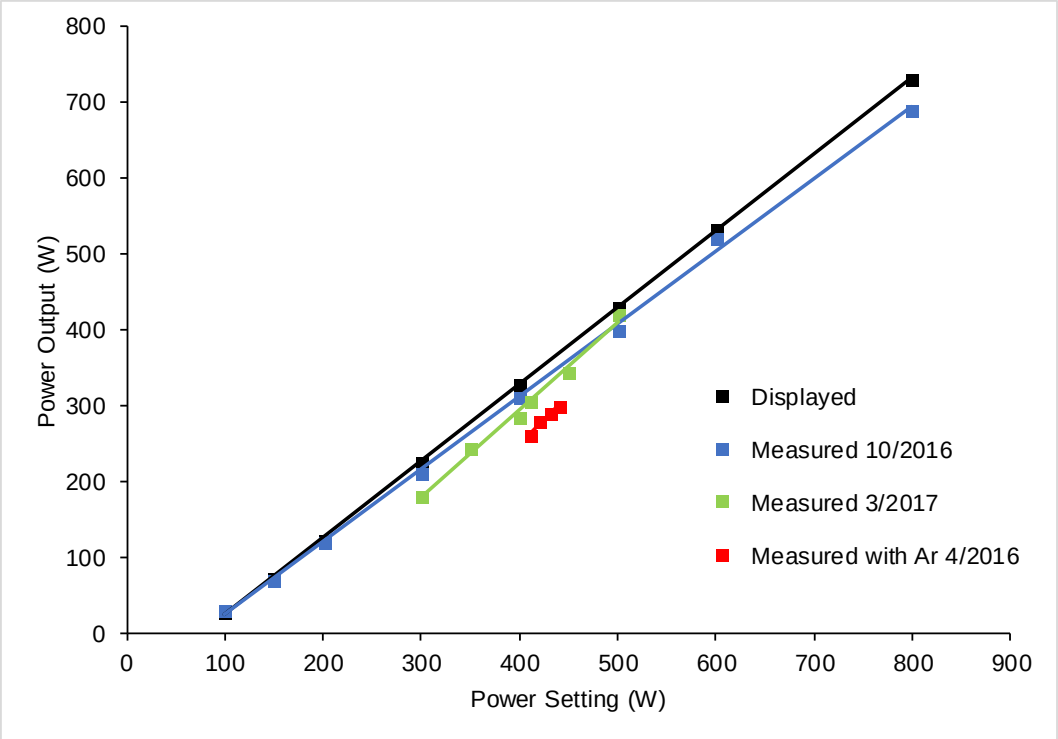

Figure 3.8. Power calibration for LENS® with power puck laser sensor. Plots shown for Displayed output from power supply, Measured 10/2016 prior to changing lens cover, Measured 3/2017 after changing lens cover, and Measured with Ar 4/2017 with same lens cover as Measured 3/2017.

3.2.4. Substrate Properties:

The substrate acts as the heat sink for the deposited part for the first several layers, as was discussed in Chapter 1 [10], [11]. The volume of the substrate affects the heat flow and thermal history of the builds. If the substrate is not mounted properly or if the build is not deposited in the center of the substrate, the thermal changes that occur from the deposition process will cause the substrate to warp. The substrate should also be allowed to fully cool between depositions so that the next build has a proper heat sink. Figure 3.9 shows several cubes deposited on one substrate. The last cube, front right, was deposited without the proper cooling period and thus exhibits a significantly different surface color change than the previously deposited builds, an indication of a different thermal history.

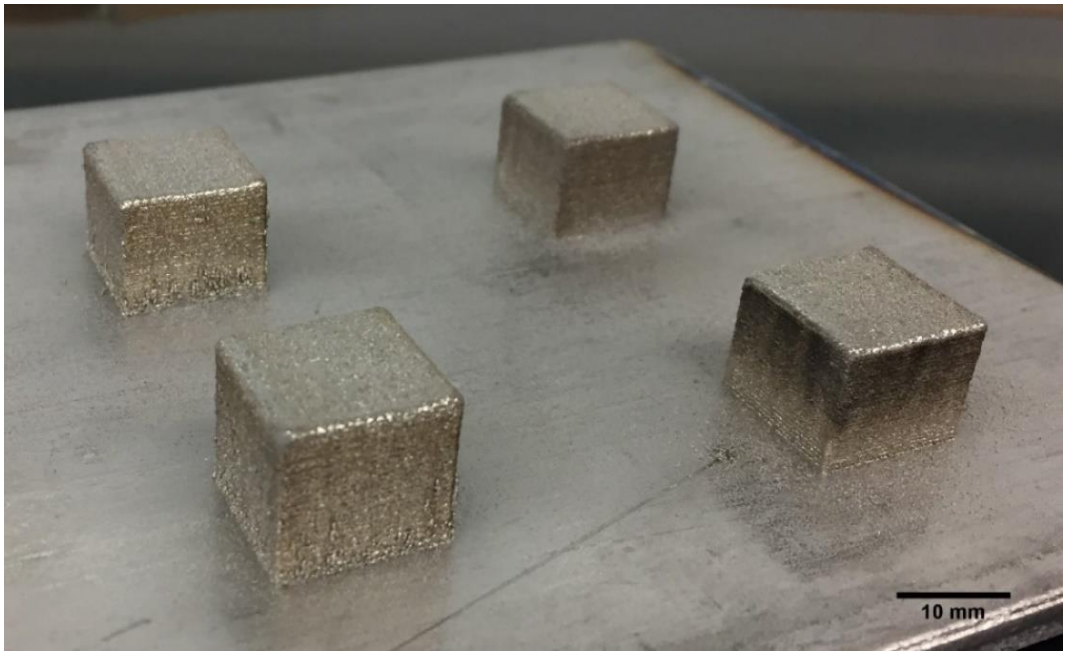

Figure 3.9. Cubes deposited on one substrate. The front right cube was deposited last and by the noted surface color change experienced a different range of thermal gradients than the previous builds.

3.3. Operation Guidelines:

3.3.1. Running a new program on the LENS®:

When starting a new project, it is crucial to run the initial test build in the center of a substrate, with the deposition head elevated above the support brackets. The program can be run without the powder feed on, with the laser set to a low power, 150 W, for the first contour pass to ensure the build space of the part is known and the nozzles will not be damaged by running into the support brackets or a previous build. Once the area of the substrate required for the build is known, the program can be aborted, working distance set, and the starting position reset by selecting to move to part zero. This lesson was learned when testing the build for the 105° hatch rotation angle for the project in Chapter 2. The current software configuration of the LENS® workstation allows for up to six hatch rotation angles in the conversion of the stl file to an sli file. If an alternative hatch rotation angle

between layers is desired, the text file needs to be manually altered, as was done for the 105° builds. Instead of using the 750 Workstation to convert the sli file to the DMC code used to run the stage and z height motors, this code was converted on a MR-7 Workstation by a lab mate. Upon the initial test run of the 105° DMC code, the deposition head was set up to run in the presumed direction as all other builds of the same size. However, this code started in the opposite direction, running directly into a previous build and bending the back-left nozzle at a 90° angle before it could be aborted. This error caused a delay of one day to remove the nozzles, replace them, and realign the laser.

3.3.2. Set up:

To set up a build, the calibration steps previously discussed in this chapter should be confirmed. Mount a clean substrate to the stage using support brackets at each corner of the substrate and screws of the appropriate length. Screws should only be five threads into the stage and tightened ¼ of a turn past hand tight. Over tightening of screws that are too deep into the stage can cause galling of the threads from stress due to thermal cycling during and after a deposition. If it is difficult to secure the screw in the desired position, use the tap provided in the tool box in the chamber to clear the hold of any debris or relocate the bracket to a different hole. Inspect the end threads of the screw to confirm they are in good condition and not flattened out. If there is a screw that cannot be removed after a deposition, do not force the removal. When time permits between depositions, remove the stage from the chamber and use an anti-seize lubricant to remove the screw.

With the substrate secured, lower deposition head while shaking the column to ensure it stretches appropriately and does not pop off the deposition head. If the column does detach,

the lens and lens cover should be inspected to ensure they are still clean and there is no debris before reattaching the column. Lower the head to the desired working distance.

3.4. Maintenance:

3.4.1. Filter replacement:

The filters inside the chamber for the argon recirculation pump and the dri-train should be replaced after approximately three hoppers full of powder has been deposited. Remove the front two filters inside the chamber and place each of the old filters in a double Ziploc bag. Remove the bags through the anti-chamber and place them in a designated metal bucket. The bucket should be placed in a safe place outdoors for approximately one week to allow oxygen to slowly leach into the bags and react with the filters. After extensive use, the filters will be black from the fine black powder discussed in Chapter 1. If this powder is exposed to high levels of oxygen immediately after removing from the argon environment the filters can combust, as shown in Figure 3.10.

Figure 3.10. Burned filters after immediate exposure to air. The filter on the left is partially melted while the filter on the right melted down completely.

3.4.2. Changing oil of vacuum pump:

The vacuum pump is an integral part of the dri-train system, purifying the chamber environment and maintaining the oxygen levels below 10 ppm. It is crucial that the oil level of the pump is maintained. If the level is low, refill with new oil through the filler hole. Add the oil slowly and allow the level to settle before adding more to avoid overfilling. To replace the oil, follow the procedure in the manual for a single-phase RV3 Edwards vacuum pump.

3.5. Standard Operating Procedures:

The following procedures are included in the appendices and provide systematic instructions for powder feedstock preparation, cleaning maintenance of the LENS®, and user responsibilities.

I. Sieving

Sieving was performed on 316L SS for all cycles of the powder reuse project. The procedure was adapted from ASTM B214 [20] for this alloy specifically.

II. LENS® Cleaning

The LENS® cleaning procedure is intended to be used as a basic guideline for cleaning the LENS® chamber after excessive use or when changing feedstock material. Some steps can be modified depending on the material composition and specific deposition mode of operation. The laboratory safety officer should be consulted when cleaning new materials. Cleaning should not be done alone.

III. Dri-train Regeneration

A regeneration cycle should be performed every 6 months to one year depending on machine usage. The dri-train beads should also be replaced yearly per the Optomec LENS® user manual.

IV. User Log

The User Log is now located in the Optomec LENS® user manual. The log sheet should be filled out once per deposition period of material use and operation configuration. The intent is to have a record of machine operation time as well as a record of configuration and material type. This information will dictate the necessary cleaning and set up requirements for the next user.

V. User Hand-off

In addition to the data included in the User Log, the Hand-off checklist provides steps for the current user to ensure the system is ready for the next user without causing change-over delays.

VI. Calculation for Powder Usage

The amount of powder needed to complete the powder reuse study of 10 deposition cycles with the LENS® process was calculated using an algorithm that considers deposition parameters, size, and quantity. The deposition time is calculated from the linear path of the laser for number of tracks and contours per layer. The powder feed rate is then used to determine the amount of powder required for the calculated deposition time. The loses of powder during deposition in the chamber and sieving were estimated from previous processes.

VII. Deposited Parts List

All parts deposited with the 316L SS powder used for the recycle project of Chapter 1 and the hatch rotation angle project of Chapter 2 are listed in this appendix in order of deposition. To complete the recycle project with enough powder to deposit the C9 parts, a total of 211 parts were manufactured.

3.6. Conclusions:

- Many variables of the LENS® system require calibration to ensure consistency of depositions and good build quality. If these procedures are followed diligently, consistent manufacturing is possible.

3.7. Future Work:

- Updates to the LENS® system could improve the reliability of the system. From the study presented in this thesis, a major update would be the accurate monitoring of powder feed rates. With all other parameters properly calibrated, the powder feed rate, for large builds specifically, could still cause deposition inconsistencies. The

implementation of a real-time mass loss monitoring system of the powder from the hopper could start the investigation into where the PFR starts to change during a long build. Subsequent in situ testing could lead to predictable feed rates for more reliable microstructures.

References

[1] I. Gibson, D. Rosen, and B. Stucker, "Directed Energy Deposition Processes," in *Additive Manufacturing Technologies*, Springer, New York, NY, 2015, pp. 245–268.

[2] M. Tomlin and J. Meyer, "Topology Optimization of an Additive Layer Manufactured (ALM) Aerospace Part," presented at the 7th Altair CAE technology Conference, 2011.

[3] H. Clemens and H. Kestler, "Processing and Applications of Intermetallic γ-TiAl-Based Alloys," *Adv. Eng. Mater.*, vol. 2, no. 9, pp. 551–570, Sep. 2000.

[4] S. L. Sing, J. An, W. Y. Yeong, and F. E. Wiria, "Laser and electron-beam powder-bed additive manufacturing of metallic implants: A review on processes, materials and designs," *J. Orthop. Res.*, vol. 34, no. 3, pp. 369–385, Mar. 2016.

[5] A. L. Jardini *et al.*, "Cranial reconstruction: 3D biomodel and custom-built implant created using additive manufacturing," *Journal of Cranio-Maxillofacial Surgery*, vol. 42, no. 8, pp. 1877–1884, Dec. 2014.

[6] F. Oney, "Video: Go big or go home—Navy creates first submarine hull on giant 3-D printer | The American Ceramic Society." [Online]. Available: http://ceramics.org/ceramic-tech-today/video-go-big-or-go-home-navy-creates-first-submarine-hull-on-giant-3-d-printer. [Accessed: 18-Aug-2017].

[7] Optomec, "LENS_MR-7_Datasheet." [Online]. Available: https://www.optomec.com/wp-content/uploads/2014/04/LENS_MR-7_WEB.pdf. [Accessed: 23-Aug-2017].

[8] B. Zheng, Y. Xiong, and J. Nguyen, "Powder additive processing with laser engineered net shaping (LENS)," in *Powder Metallurgy Research Trends*, 2009, pp. 125–190.

[9] J. A. Brooks and A. W. Thompson, "Microstructural development and solidification cracking susceptibility of austenitic stainless steel welds," *International Materials Reviews*, vol. 36, no. 1, pp. 16–44, Jan. 1991.

[10] B. Zheng, Y. Zhou, J. E. Smugeresky, J. M. Schoenung, and E. J. Lavernia, "Thermal Behavior and Microstructural Evolution during Laser Deposition with Laser-Engineered Net Shaping: Part I. Numerical Calculations," *Metallurgical and Materials Transactions A*, vol. 39, no. 9, pp. 2228–2236, Sep. 2008.

[11] S. M. Thompson, L. Bian, N. Shamsaei, and A. Yadollahi, "An overview of Direct Laser Deposition for additive manufacturing; Part I: Transport phenomena, modeling and diagnostics," *Additive Manufacturing*, vol. 8, pp. 36–62, Oct. 2015.

[12] M. T. Ensz, M. L. Griffith, and L. D. Harwell, "Software Development for Laser Engineered Net Shaping," Sandia National Labs., Albuquerque, NM (United States), SAND--98-1849C; CONF-980826--, Aug. 1998.

[13] K. Guan, Z. Wang, M. Gao, X. Li, and X. Zeng, "Effects of processing parameters on tensile properties of selective laser melted 304 stainless steel," *Materials & Design*, vol. 50, pp. 581–586, Sep. 2013.

[14] L. C. Ardila *et al.*, "Effect of IN718 Recycled Powder Reuse on Properties of Parts Manufactured by Means of Selective Laser Melting," *Physics Procedia*, vol. 56, pp. 99–107, Jan. 2014.

[15] H. P. Tang, M. Qian, N. Liu, X. Z. Zhang, G. Y. Yang, and J. Wang, "Effect of Powder Reuse Times on Additive Manufacturing of Ti-6Al-4V by Selective Electron Beam Melting," *JOM*, vol. 67, no. 3, pp. 555–563, Feb. 2015.

[16] P. A. Carroll *et al.*, "The effect of powder recycling in direct metal laser deposition on powder and manufactured part characteristics," in *Proceedings of AVT-139 Specialists Meeting on Cost Effective Manufacture via Net Shape Processing*, NATO Research and Technology Organisation, 2006.
[17] "ASTM B215-15 Standard Practices for Sampling Metal Powders." [Online]. Available: https://doi.org/10.1520/B0215-15. [Accessed: 23-Aug-2017].
[18] D. J. Kotecki and T. A. Siewert, "WRC-1992 constitution diagram for stainless steel weld metals: a modification of the WRC-1988 diagram," *Welding Journal*, vol. 71.5, pp. 171–178, 1992.
[19] D. L. Olson, "Prediction of Austenitic Weld Metal Microstructure and Properties," *Weld. J. (Miami); (United States)*, vol. 64:10, Oct. 1985.
[20] "ASTM B214-16 Standard Test Method for Sieve Analysis of Metal Powders," *ASTM International*, 2016.
[21] "ASTM B527-15 Standard Test Method for Tap Density of Metal Powders and Compounds," *ASTM International*, 2015.
[22] "ASTM B213-17 Standard Test Methods for Flow Rate of Metal Powders Using the Hall Flowmeter Funnel," *ASTM International*, 2017. [Online]. Available: https://doi.org/10.1520/B0213-17. [Accessed: 23-Aug-2017].
[23] "FLOWABILITY Analysis with the REVOLUTION | Mercury Scientific Inc." [Online]. Available: http://www.mercuryscientific.com/instruments/flowability-analysis-revolution. [Accessed: 23-Jun-2017].
[24] "ASTM E9-09 Standard Test Methods of Compression Testing of Metallic Materials at Room Temperature," *ASTM International*, 2009. [Online]. Available: https://doi.org/10.1520/E0009-09. [Accessed: 23-Aug-2017].
[25] A. T. Sutton, C. S. Kriewall, M. C. Leu, and J. W. NewKirk, "Powders for Additive Manufacturing Processes: Characterization Techniques and Effects on Part Properties," presented at the 27th Annual International Solid Freeform Fabrication Symposium – An Additive Manufacturing Conference, 2016.
[26] J. C. Lippold, "Solidification Behavior and Cracking Susceptibility of Pulsed-Laser Welds in Austenitic Stainless Steels," *Welding Journal Including Welding Research Supplement*, no. 73.6, p. 129s, 1994.
[27] M. Vasudevan, M. Murugananth, A. K. Bhaduri, B. Raj, and K. P. Rao, "Bayesian neural network analysis of ferrite number in stainless steel welds," *Science and Technology of Welding and Joining*, vol. 9, no. 2, pp. 109–120, Apr. 2004.
[28] "NIST X-ray Photoelectron Spectroscopy (XPS) Database, Version 3.5." [Online]. Available: https://srdata.nist.gov/xps/Default.aspx. [Accessed: 17-Aug-2017].
[29] T. Yamashita and P. Hayes, "Analysis of XPS spectra of Fe2+ and Fe3+ ions in oxide materials," *Applied Surface Science*, vol. 254, no. 8, pp. 2441–2449, Feb. 2008.
[30] J. Kummailil, C. Sammarco, D. Skinner, C. A. Brown, and K. Rong, "Effect of Select LENS™ Processing Parameters on the Deposition of Ti-6Al-4V," *Journal of Manufacturing Processes*, vol. 7, no. 1, pp. 42–50, Jan. 2005.
[31] A. Simchi, "The role of particle size on the laser sintering of iron powder," *Metall and Materi Trans B*, vol. 35, no. 5, pp. 937–948, Oct. 2004.
[32] Y. Y. Sun, S. Gulizia, C. H. Oh, C. Doblin, Y. F. Yang, and M. Qian, "Manipulation and Characterization of a Novel Titanium Powder Precursor for Additive Manufacturing Applications," *JOM*, vol. 67, no. 3, pp. 564–572, Mar. 2015.

[33] C. T. Schade, T. F. Murphy, and C. Walton, “Development of atomized powders for additive manufacturing,” in *Powder Metallurgy and Particulate Materials*, Orlando, FL, 2014, pp. 215–225.
[34] E. C. Abdullah and D. Geldart, “The use of bulk density measurements as flowability indicators,” *Powder Technology*, vol. 102, no. 2, pp. 151–165, Mar. 1999.
[35] A. Strondl, O. Lyckfeldt, H. Brodin, and U. Ackelid, “Characterization and Control of Powder Properties for Additive Manufacturing,” *JOM*, vol. 67, no. 3, pp. 549–554, Jan. 2015.
[36] R. McGregor, “Can Particle Size Predict Powder Flow Behavior?,” *Brookfield Engineering*, 25-Jun-2012. [Online]. Available: https://www.pharmaceuticalonline.com/doc/can-particle-size-predict-powder-flow-behavior-0001. [Accessed: 30-Jul-2017].
[37] M. P. Sharma and C. T. Crowe, “A numerical model for gas-particle flow through an orifice,” *Mathematical Modelling*, vol. 9, no. 9, pp. 691–700, Jan. 1987.
[38] M. F. McGuire, *Stainless Steels for Design Engineers*. ASM International, 2008.
[39] C. Teng *et al.*, “Simulating Melt Pool Shape and Lack of Fusion Porosity for Selective Laser Melting of Cobalt Chromium Components,” *J. Manuf. Sci. Eng*, vol. 139, no. 1, pp. 011009-011009-11, Aug. 2016.
[40] D. F. Susan, J. D. Puskar, J. A. Brooks, and C. V. Robino, “Quantitative characterization of porosity in stainless steel LENS powders and deposits,” *Materials Characterization*, vol. 57, no. 1, pp. 36–43, Jul. 2006.
[41] W. E. Frazier, “Metal Additive Manufacturing: A Review,” *J. of Materi Eng and Perform*, vol. 23, no. 6, pp. 1917–1928, Jun. 2014.
[42] J. A. Slotwinski, E. J. Garboczi, P. E. Stutzman, C. F. Ferraris, S. S. Watson, and M. A. Peltz, “Characterization of Metal Powders Used for Additive Manufacturing,” *J. Res. Natl. Inst. Stand. Technol.*, vol. 119, pp. 460–493, Sep. 2014.
[43] A. Angelastro, S. L. Campanelli, G. Casalino, A. D. Ludovico, and S. Ferrara, “A methodology for optimization of the Direct Laser Metal Deposition process,” in *Key Engineering Materials*, 2011, vol. 473, pp. 75–82.
[44] Y. J. Huang, “Characterization of dilution action in laser-induction hybrid cladding,” *Opt. Laser Technol.*, vol. 43, no. 5, pp. 965–973, Jul. 2011.
[45] B. Zheng, Y. Zhou, J. E. Smugeresky, J. M. Schoenung, and E. J. Lavernia, “Thermal Behavior and Microstructure Evolution during Laser Deposition with Laser-Engineered Net Shaping: Part II. Experimental Investigation and Discussion,” *Metallurgical and Materials Transactions A*, vol. 39, no. 9, pp. 2237–2245, Sep. 2008.
[46] W. Hofmeister and M. Griffith, “Solidification in direct metal deposition by LENS processing,” *JOM*, vol. 53, no. 9, pp. 30–34.
[47] C. Hausner, T. H. C. Childs, K. W. Dalgarno, and R. B. Eane, “Atmospheric Control During Direct Selective Laser Sintering of Stainless Steel 314S powder,” in *Solid Freeform Fabrication Symposium 1999*, 1999.
[48] T. Mukherjee, J. S. Zuback, A. De, and T. DebRoy, “Printability of alloys for additive manufacturing,” *Sci Rep*, vol. 6, Jan. 2016.
[49] R. Rai, J. W. Elmer, T. A. Palmer, and T. DebRoy, “Heat transfer and fluid flow during keyhole mode laser welding of tantalum, Ti–6Al–4V, 304L stainless steel and vanadium,” *J. Phys. D: Appl. Phys.*, vol. 40, no. 18, p. 5753, 2007.

[50] T. Vilaro, C. Colin, and J. D. Bartout, "As-Fabricated and Heat-Treated Microstructures of the Ti-6Al-4V Alloy Processed by Selective Laser Melting," *Metall and Mat Trans A*, vol. 42, no. 10, pp. 3190–3199, Oct. 2011.
[51] W. E. King *et al.*, "Observation of keyhole-mode laser melting in laser powder-bed fusion additive manufacturing," *Journal of Materials Processing Technology*, vol. 214, no. 12, pp. 2915–2925, Dec. 2014.
[52] J. D. Madison and L. K. Aagesen, "Quantitative characterization of porosity in laser welds of stainless steel," *Scripta Materialia*, vol. 67, no. 9, pp. 783–786, Nov. 2012.
[53] N. Shamsaei, A. Yadollahi, L. Bian, and S. M. Thompson, "An overview of Direct Laser Deposition for additive manufacturing; Part II: Mechanical behavior, process parameter optimization and control," *Additive Manufacturing*, vol. 8, pp. 12–35, Oct. 2015.
[54] P. Hanzl, M. Zetek, T. Bakša, and T. Kroupa, "The Influence of Processing Parameters on the Mechanical Properties of SLM Parts," *Procedia Engineering*, vol. 100, pp. 1405–1413, Jan. 2015.
[55] T. Niendorf, S. Leuders, A. Riemer, H. A. Richard, T. Tröster, and D. Schwarze, "Highly Anisotropic Steel Processed by Selective Laser Melting," *Metall and Materi Trans B*, vol. 44, no. 4, pp. 794–796, Aug. 2013.
[56] M. Rappaz, S. A. David, J. M. Vitek, and L. A. Boatner, "Analysis of solidification microstructures in Fe-Ni-Cr single-crystal welds," *MTA*, vol. 21, no. 6, pp. 1767–1782, Jun. 1990.
[57] M. L. Griffith *et al.*, "Understanding the Microstructure and Properties of Components Fabricated by Laser Engineered Net Shaping (LENS)," *MRS Online Proceedings Library Archive*, vol. 625, Jan. 2000.

Appendix I

Sieving 316L Stainless Steel Powders

Sieving is a critical step in the reusing of powder for additive manufacturing. During the deposition process powder particles can partially melt and agglomerate to sizes outside the operating range for the system. The Sandia study requires at least 10 cycles of reusing previously deposited powder. The designated geometries require approximately 250 lbs of powder under the least efficient deposition conditions. Given the amount of powder that will be recycled and sieved for this project, following the recommended sieve analysis amount for metal powders per ASTM B214 (110 g per 15 minute shake period) is not feasible within the time constraint. ASTM E276 (sieve analysis of metal-bearing ores and related materials) was used as a guide to determine a reasonable amount of powder to sieve per shake period without damaging or losing excessive reusable particles.

Approach:

Sieve trials of 500 g up to 1100 g were timed and measured following ASTM E276. The powder was sieved until additional shake time did not produce more than 0.3% by mass of additional powder through the 106 μm sieve. Small amounts of powder require more hands on attention while large amounts overload the sieve. Ideally a sample fraction should not exceed more than a few particle layers from the surface of the sieve, per vendor recommendation. The most efficient quantity was 650-700 g for two periods of 7 ½ minutes with the 106 μm sieve being dry brushed between measurements to dislodge any clogged particles.

Sieving Procedure:

1. Confirm all sieves to be used are clean and dry.
2. Arrange the sieves in increasing mesh size from bottom to top with target mesh sizes (45 μm, 106 μm, 150 μm) in the middle of the stack, sieve pan at the bottom, and lid at the top.
3. Weigh out 700-1000 g of powder and evenly distribute it over the surface of the 106 μm sieve.
4. Gently place sieve stack in the shaker and secure by tighten the three knobs of the hold down bar. The side knobs of the bar should be tightened on the threaded area of the rods.
5. Set the timer to 15 minutes and press start. Monitor shaker for first minute to ensure knobs do not loosen right away and are still tight. Pause shaker to retighten if necessary.
6. Close the doors of the sound proof enclosure.
7. When the timer is done, remove the sieve stack.
8. Using a large funnel, poor the remaining powder in the 150 μm sieve into a clean, empty bottle.
9. Turn the 150 μm sieve upside down on a clean paper towel. Gently brush the underside of the mesh with a sieve brush in a circular motion to dislodge any clogged particles. Add the particles to the powder collected from the sieve.
10. Repeat step 9 to collect all powder from the sieves in designated bottles by particle size.
11. Dry brush each sieve from the bottom side of the mesh to dislodge any clogging particles.
12. Add dislodged particles to the designated bottle for that sieve.
13. Repeat sieving process until all powder is sieved.

14. After sieving is complete, clean sieves per cleaning procedure.
15. Clean up sieve area of all powder and personal items.
16. Return clean sieves and sieve brushes to designated drawers after use.

Sieve Cleaning Procedure:

1. Use only mild soap and water. No chemicals. No DI water.
2. Use sieve brush in a circular motion on the bottom side of mesh to gently dislodge remaining particles.
3. If necessary, place sieve in sonicator on the low setting to remove remaining particles.
4. Rinse thoroughly.
5. Separate to dry, do not stack.

Appendix II

General LENS® Cleaning

The procedure presented in this appendix is intended to be used as a basic guideline for cleaning the LENS® chamber after excessive use or before changing feedstock material. Some steps can be modified depending on the material composition and specific deposition mode of operation. The laboratory safety officer should be consulted when cleaning new materials. Cleaning should not be done alone.

1. Wear appropriate PPE: Lab coat, gloves, eye protection, respirator.
2. Place filters in double bagged Ziplocs while still under argon atmosphere. Make sure the bags are open when putting them in the anti-chamber. Remove closed bags with the filters (one per bag) from chamber through the anti-chamber and place in a designated black bucket outside.
3. Empty rear vacuum chamber using black buckets and foil lid. Cycle pinch valve to remove all powder.
4. Set dri-train blower speed to 0%.
5. Turn dri-train circulation valve switch off.
6. Isolate argon line, close argon valve on tank.
7. Turn off O_2 sensor.
8. Set lab pressure limits: Low = -0.5
9. Let O_2 into the chamber slowly to saturate environment prior to removing window.
10. Remove front window.
11. Collect powder from stage in appropriate recycled powder bottle.
12. Dry brush all surfaces to remove powder remnants. Depending on material last deposited, use wet towels or HEPA filter shop vac to collect remaining powder from chamber floor.
13. Clean anti-chamber.
14. Clean focusing lens and cover with appropriate cleaning technique and lens paper (See Baolong).
15. Replace filters for argon, x2 20 μm filters for front two filter housings and x1 100 μm filter for back filter housing.
16. Replace oxygen sensor.
17. Reseal front window.
18. Reset lab pressure limits: High = +3, Low = +1
19. Confirm argon tank is sufficiently full. Connect and open tank valve and open inlet valves.
20. Turn on argon recirculation power.
21. Start purge cycle for 1 hour to re-pressurize chamber.
22. Check O_2 level is below 100 ppm prior to leaving sensor on.
23. Continue to purge until O_2 is below 100 ppm.
24. Once O_2 level is below 100 ppm, turn dri-train circulation valve switch on and turn blower to 50 %.

Appendix III

Dri-train Regeneration

A regeneration cycle should be performed every 6 months to one year depending on machine usage. The dri-train beads should also be replaced yearly per the Optomec LENS® user manual.

1. Connect forming gas to regen regulator. Open regen line valves at regulator and side glovebox port.
2. Set regulator on forming gas to 40 psi.
3. Turn off argon re-circulation system.
4. Close dri-train circulation valves on side of glovebox.
5. Turn dri-train blower all the way down.
6. Turn off O_2 sensor.
7. Turn on vacuum pump.
8. Turn LENS® Workstation to dri-train menu, press Function to enter regeneration menu and start regeneration.
9. Confirm sufficient flow of forming gas.
10. When regeneration of dri-train is complete, close valve on forming gas.
11. Press escape to return to main option menu.
12. Open main circulation valves on glovebox.
13. Turn on blower, set at 50%, using the up arrow on the control panel.
14. Turn on O_2 sensor.

Appendix IV

User Log

The User Log is now located in the Optomec LENS® user manual. The log sheet should be filled out once per deposition period of material use and operation configuration. The intent is to have a record of machine operation time as well as a record of configuration and material type. This information will dictate the necessary cleaning and set up requirements for the next user.

Date	Name	Laser Mode (Cont. / Gate)	Powder Mode (Hopper / Bed)	Material	Issues (List / None)

Appendix V

User Hand-off

In addition to the data included in the User Log, the Hand-off checklist provides steps for the current user to ensure the system is ready for the next user without causing change-over delays. For specific details of LENS® operation and troubleshooting please refer to Optomec user manuals located in the LENS® laboratory.

1. Prior to the last day of your reservation (or the first day if you are the next user) reach out to the next user (or current user) to confirm the schedule is still on track, or give warning if you're project is delayed. Refer to LENS® google calendar for the up-to-date schedule.
2. Communicate with the person/s who will be using the LENS® after you about what condition they are using it in (what atmosphere) and what material they will be using. This should let you know how much cleaning needs to be done to remove your material and whether the glove box should be in an argon environment or not when you're done cleaning. Coordinate the cleaning process so no one does it on their own.
3. If you are using argon or will be using argon, make sure there is enough for the next person to get started. Please order argon for your project if you are in need or replacing our stock for the next person.
4. Tasks that should be done every time the chamber is opened and especially if the material used in the LENS® is changing. These include (but not limited to):
    a. Changing filters (x4)
    b. Purging powder feed lines (replace if necessary)
    c. Vacuuming out hoppers
    d. Vacuuming glove box (stage, floor, walls, ceiling, etc)
    e. Replace HEPA vacuum bag in portable vacuum
    f. Emptying glove box vacuum (located on the back of the LENS®)
    g. Clean inside of window and gloves to remove all powders
    h. Cleaning focusing lens (this should be done by Baolong or James until someone else is properly trained)
    i. Clean anti-chamber
    j. Confirm proper seal on window and anti-chamber doors
    k. Clean tools in glove box and tool box (remember to return tools to the glovebox prior to sealing)

Appendix VI

Calculation for Powder Usage

The amount of powder needed to complete the powder reuse study of 10 deposition cycles with the LENS® process was calculated using an algorithm that considers deposition parameters, size, and quantity. The deposition time was calculated from the linear path of the laser for number of tracks and contours per layer. The powder feed rate is then used to determine the amount of powder required for the calculated deposition time. The loses of powder during deposition in the chamber and sieving were estimated from previous projects.

Table VI.1. Build parameters for consistent cube and cylinder depositions.

Build Type (Cycles)	Dimensions			Speed (in/min)	Hatch Spacing (in)	Layer Increment (in)	Contour	PFR (g/min)	Build Quantity
	x	y	z						
Cubes (0-9)	0.6	0.6	0.52	40	0.016	0.01	1	28	4
Cylinders (0,1,5,9)	1	1	2	40	0.016	0.01	1	28	2

Table VI.2. Calculated build time and powder required to deposit consistent depositions for recycle project.

Build Types (Cycles)	Build Time (min)	Powder needed (lbs)	Hopper loss (lbs)	Machine loss (%)	Sieve loss (%)	1 Cycle Input (lbs)
Cubes (0-9)	32.37	1.998	0.364	0.02	0.07	8.527
Cylinders (0,1,5,9)	328.21	20.260	0.364	0.02	0.07	41.718

The parameters in Table VI.1 were used to determine the build time estimate shown in the table below, by calculating the linear tracks the laser would deposit per layer including the contour. Based on the calculations from Table VI.2, a total of 375 lbs estimated to be required to deposit the cubes and cylinders for the four select cycles, and the consistent cubes deposited for the other 6 cycles. However, the actual machine and sieving losses were less than predicted. The deposition efficiency also was much lower than 10% for some cycles thus creating more reusable powder. The combination of these resulted in the actual amount of powder used for the entirety of this project being only 250 lbs.

Appendix VII

Deposited Parts List

All parts deposited with the 316L SS powder used for the recycle project of Chapter 1 and the hatch rotation angle project of Chapter 2 are listed in this appendix in order of deposition. The cylinders deposited for C0, C1, C5, and C9 are not included in this list. To complete the recycle project with enough powder to deposit the two C9 cylinders, a total of 211 parts were manufactured.

Build Number	Cycle	Geometry/Shape	Dimensions (WxDxH) (in)	Build Time (hr.min.sec)
1	0	Cube	0.60x0.60x0.52	36.00
2	0	Cube	0.60x0.60x0.52	34.67
3	0	Cube	0.60x0.60x0.52	35.50
4	0	Cube	0.60x0.60x0.52	34.50
5	0	Cube	0.60x0.60x0.52	35.50
1	1	Cube	0.60x0.60x0.52	34.02
2	1	Cube	0.60x0.60x0.52	33.45
3	1	Cube	0.60x0.60x0.52	33.46
4	1	Cube	0.60x0.60x0.52	33.15
5	1	Cube	0.60x0.60x0.52	33.15
6	1	Cube	0.60x0.60x0.52	33.15
7	1	Cube	0.60x0.60x0.52	33.15
8	1	Cube	0.60x0.60x0.52	33.55
9	1	Cube	0.60x0.60x0.52	17.18
10	1	Cube	0.60x0.60x0.52	18.09
11	1	Cube	0.60x0.60x0.52	33.45
12	1	Cube	0.60x0.60x0.52	33.25
13	1	Cube	0.60x0.60x0.52	33.55
14	1	Cube	0.60x0.60x0.52	33.55
15	1	Cube	0.60x0.60x0.52	24.30
16	1	Cube	0.60x0.60x0.52	12.57
17	1	Cube	0.60x0.60x0.52	34.15
18	1	Cube	0.60x0.60x0.52	--
19	2	Cube	0.60x0.60x0.52	7.43
20	2	Cube	0.60x0.60x0.52	8.21
21	2	Cube	0.60x0.60x0.52	33.25
22	2	Cube	0.60x0.60x0.52	21.06
23	0	Cube	0.60x0.60x0.52	6.00
24	0	Cube	0.60x0.60x0.52	20.29
25	0	Cube	0.60x0.60x0.52	34.42
26	0	Cube	0.60x0.60x0.52	34.52
27	0	Cube	0.60x0.60x0.52	34.42

Build Number	Cycle	Geometry/Shape	Dimensions (WxDxH) (in)	Build Time (hr.min.sec)
28	0	Cube	0.60x0.60x0.52	34.13
29	0	Cube	0.60x0.60x0.52	34.13
30	1	Cube	0.60x0.60x0.52	34.42
31	1	Cube	0.60x0.60x0.52	34.42
32	1	Cube	0.60x0.60x0.52	34.42
33	1	Cube	0.60x0.60x0.52	34.42
34	1	Cube	0.60x0.60x0.52	34.42
35	1	Cube	0.60x0.60x0.52	--
1	0	Cube	0.60x0.60x0.52	18.32
1.5	0	Cube	0.60x0.60x0.52	18.16
2	0	Cube	0.60x0.60x0.52	17.45
3	0	Cube	0.60x0.60x0.52	11.10
4	0	Cube	0.60x0.60x0.52	10.31
5	0	Cube	0.60x0.60x0.52	10.31
6	0	Cube	0.60x0.60x0.52	10.31
7	0	Cube	0.60x0.60x0.52	17.46
8	0	Cube	0.60x0.60x0.52	13.48
9	0	Cube	0.60x0.60x0.52	13.48
10	0	Cube	0.60x0.60x0.52	13.48
11	0	Cube	0.60x0.60x0.52	13.49
12	0	Cube	0.60x0.60x0.52	13.48
13	0	Cube	0.60x0.60x0.52	13.48
14	0	Cube	0.60x0.60x0.52	17.46
15	0	Cube	0.60x0.60x0.52	17.49
16	0	Cube	0.60x0.60x0.52	17.46
17	0	Cube	0.60x0.60x0.52	17.46
18	0	Cube	0.60x0.60x0.52	18.07
19	0	Cube	0.60x0.60x0.52	17.46
20	0	Cube	0.60x0.60x0.52	17.46
21	0	Cube	0.60x0.60x0.52	17.39
22	0	Cube	0.60x0.60x0.52	17.46
23	0	Cube	0.60x0.60x0.52	17.46
24	0	Cube	0.60x0.60x0.52	17.46
25	0	Cube	0.60x0.60x0.52	17.46
26	0	Cube	0.60x0.60x0.52	17.46
27	0	Cube	0.60x0.60x0.52	22.21
28	0	Cube	0.60x0.60x0.52	34.12
29	0	Cube	0.60x0.60x0.52	23.49
30	0	Cube	0.60x0.60x0.52	10.31

Build Number	Cycle	Geometry/Shape	Dimensions (WxDxH) (in)	Build Time (hr.min.sec)
30	0	Cube	0.60x0.60x0.52	34.12
31	0	Cube	0.60x0.60x0.52	34.13
32	0	Cube	0.60x0.60x0.52	34.12
33	1	Cube	0.60x0.60x0.52	34.12
34	1	Cube	0.60x0.60x0.52	34.12
35	1	Cube	0.60x0.60x0.52	34.12
36	1	Cylinder stack	1.00x0.75x1.00	28.55
37	1	Cylinder stack	1.00x0.75x1.00	1.32.0
38	2	Cube	0.60x0.60x0.52	34.12
39	2	Cube	0.60x0.60x0.52	34.13
40	2	Cube	0.60x0.60x0.52	34.12
41	2	Rose	--	--
42	2	Cylinder stack	1.00x0.75x1.00	1.31.52
43	2	Chimney	1.00x0.25x3.00	56.27
44	2	Cube	0.60x0.60x0.52	34.12
45	2	Block	1.50x1.50x0.40	33.17
46	2	Chimney	1.00x0.25x3.00	41.14
47	2	Chimney	0.50x0.20x1.75	10.32
48	2	Chimney	1.00x0.25x3.00	55.45
49	2	Block	1.50x1.50x0.40	2:26.10
50	2	Block	1.50x1.50x0.40	2.20.14
51	2	Block	1.60x0.40x1.60	3.00.50
52	2	Cube	0.60x0.60x0.52	32.44
53	2	Cube	0.60x0.60x0.52	34.12
54	2	Cylinder stack	1.00x1.75x1.00	1.32.00
55	3	Cube	0.60x0.60x0.52	34.12
56	3	Cylinder stack	1.00x1.75x1.00	1.28.10
57	3	Hatch Cube	0.62x0.62x0.52	38.20
58	3	Cube	0.60x0.60x0.52	34.56
59	3	Cube	0.60x0.60x0.52	33.24
60	3	Cube	0.60x0.60x0.52	34.12
61	3	Cube	0.60x0.60x0.52	34.12
62	3	Cube	0.60x0.60x0.52	34.12
63	3	Chimney	1.00x0.25x3.00	55.45
64	3	Block	1.50x1.50x0.40	2.20.20
65	3	Block	1.50x1.50x0.40	2.20.20
66	3	Block	1.50x0.40x1.50	2.30.20
67	3	Block	1.50x0.40x1.50	2.30.20
68	3	Block	1.50x1.50x0.40	2.20.20

Build Number	Cycle	Geometry/Shape	Dimensions (WxDxH) (in)	Build Time (hr.min.sec)
69	0	Hatch Cube	0.62x0.62x0.52	37.36
70	0	Hatch Cube	0.62x0.62x0.52	13.15
71	0	Hatch Cube	0.62x0.62x0.52	34.73
72	0	Hatch Cube	0.62x0.62x0.52	37.37
73	0	Hatch Cube	0.62x0.62x0.52	36.03
74	0	Hatch Cube	0.62x0.62x0.52	36.03
75	0	Hatch Cube	0.62x0.62x0.52	37.37
76	0	Hatch Cube	0.62x0.62x0.52	36.07
77	4	Block	1.50x1.50x0.40	2.20.20
78	4	Block	1.50x1.50x0.40	2.20.15
79	4	Block	1.50x0.40x1.50	2.33.00
80	4	Block	1.50x0.40x1.50	2.33.41
81	4	Block	1.50x0.40x1.50	2.33.41
82	4	Block	1.50x1.50x0.40	2.33.00
83	0	Hatch Cube	0.62x0.62x0.52	32.26
84	0	Hatch Cube	0.62x0.62x0.52	32.36
85	0	Hatch Cube	0.62x0.62x0.52	3.28
86	0	Hatch Cube	0.62x0.62x0.52	2.02
87	0	Hatch Cube	0.62x0.62x0.52	36.02
88	0	Hatch Cube	0.62x0.62x0.52	36.02
89	0	Hatch Cube	0.62x0.62x0.52	36.02
90	0	Hatch Cube	0.62x0.62x0.52	36.02
91	0	Hatch Cube	0.62x0.62x0.52	32.27
92	0	Hatch Cube	0.62x0.62x0.52	32.27
93	0	Hatch Cube	0.62x0.62x0.52	32.27
94	0	Hatch Cube	0.62x0.62x0.52	32.27
95	0	Hatch Cube	0.62x0.62x0.52	37.37
96	0	Hatch Cube	0.62x0.62x0.52	37.37
97	0	Hatch Cube	0.62x0.62x0.52	37.37
98	0	Hatch Cube	0.62x0.62x0.52	37.37
99	0	Hatch Cube	0.62x0.62x0.52	37.37
100	0	Hatch Cube	0.62x0.62x0.52	5.53
101	0	Hatch Cube	0.62x0.62x0.52	32.25
102	1	Block	2.25x2.25x0.56	8.00.36
103	2	Block	2.25x2.25x0.56	8.06.39
104	1	Cube	1.20x1.20x1.04	4.11.41
105	1	Cube	1.20x1.20x1.04	4.11.41
106	1	Cube	1.20x1.20x1.04	4.11.37
107	1	Hatch Cube	0.62x0.62x0.52	33.56

Build Number	Cycle	Geometry/Shape	Dimensions (WxDxH) (in)	Build Time (hr.min.sec)
108	1	Hatch Cube	0.62x0.62x0.52	35.58
109	1	Cube	1.20x1.20x1.04	4.11.33
110	1	Cube	1.20x1.20x1.04	26.02
111	2	Cube	1.20x1.20x1.04	4.11.37
112	2	Cube	1.20x1.20x1.04	1.41.70
113	2	Cube	1.20x1.20x1.04	4.11.37
114	2	Cube	1.20x1.20x1.04	4.11.37
115	2	Block	1.60x0.40x1.60	2.52.52
116	3	Cube	0.60x0.60x0.52	35.44
117	3	Cube	1.20x1.20x1.04	4.11.36
118	3	Cube	1.20x1.20x1.04	4.11.36
119	3	Chimney	1.00x0.25x3.00	55.45
120	3	Cube	1.20x1.20x1.04	4.11.37
121	3	Cube	1.20x1.20x1.04	3.39.36
122	4	Cube	1.20x1.20x1.04	4.11.36
123	4	Cube	1.20x1.20x1.04	4.11.67
124	4	Cube	1.20x1.20x1.04	4.11.37
125	5	Chimney	1.00x0.25x3.00	55.43
126	5	Cube	1.20x1.20x1.04	4.11.36
127	5	Cube	1.20x1.20x1.04	4.11.37
128	6	Cube	1.20x1.20x1.04	4.07.38
129	4	Cube	0.60x0.60x0.52	34.12
130	4	Cube	0.60x0.60x0.52	34.16
131	4	Cube	0.60x0.60x0.52	34.12
132	4	Cube	0.60x0.60x0.52	34.12
133	4	Chimney	1.00x0.25x3.00	55.46
134	5	Cube	0.60x0.60x0.52	34.12
135	5	Cube	0.60x0.60x0.52	34.12
136	5	Cube	0.60x0.60x0.52	34.12
137	6	Cube	0.60x0.60x0.52	34.12
138	6	Cube	0.60x0.60x0.52	34.12
139	6	Cube	0.60x0.60x0.52	34.12
140	7	Cube	0.60x0.60x0.52	34.12
141	7	Cube	0.60x0.60x0.52	34.12
142	7	Cube	0.60x0.60x0.52	34.12
143	7	Chimney	1.00x0.25x3.00	55.46
144	7	Cube	1.20x1.20x1.04	3.23.21
145	8	Cube	0.60x0.60x0.52	34.12
146	8	Cube	0.60x0.60x0.52	34.12

Build Number	Cycle	Geometry/Shape	Dimensions (WxDxH) (in)	Build Time (hr.min.sec)
147	8	Cube	0.60x0.60x0.52	34.12
148	8	Chimney	1.00x0.25x3.00	55.46
149	8	Chimney	1.00x0.25x3.00	55.46
150	9	Cube	0.60x0.60x0.52	34.12
151	9	Cube	0.60x0.60x0.52	34.12
152	9	Cube	0.60x0.60x0.52	34.12
153	9	Chimney	1.00x0.25x3.00	55.46
154	4	Chimney	1.00x0.25x3.00	55.46
155	5	Cube	1.20x1.20x1.04	4.11.37
156	5	Cube	1.20x1.20x1.04	3.28.1
157	6	Chimney	1.00x0.25x3.00	55.46
158	6	Cube	1.20x1.20x1.04	4.11.37
159	6	Cube	1.20x1.20x1.04	4.11.37
160	6	Cube	1.20x1.20x1.04	3.59.33
161	6	Cube	1.20x1.20x1.04	4.09.12
162	7	Cube	1.20x1.20x1.04	4.11.38
163	7	Cube	1.20x1.20x1.04	4.11.37
164	7	Cube	1.20x1.20x1.04	4.11.37
165	7	Cylinder stack	1.00x0.75x1.00	3.01.26
166	8	Cube	1.20x1.20x1.04	4.11.36
167	8	Cube	1.20x1.20x1.04	4.11.37
168	8	Cube	1.20x1.20x1.04	4.09.57
169	8	Cube	1.20x1.20x1.04	2.03.24